The Astrophysical Journal Supplement Series, 248:8 (41pp), 2020 May https://doi.org/10.3847/1538-4365/ab80c3
© 2020. The American Astronomical Society. All rights reserved.

Gamma-Ray Flares in the Long-term Light Curve of 3C 454.3

Avik Kumar Das, Raj Prince, and Nayantara Gupta
Raman Research Institute, C.V. Raman Avenue, Sadashivanagar, Bangalore 560080, India; avikdas@rri.res.in
Received 2019 September 30; revised 2020 March 15; accepted 2020 March 16; published 2020 April 27

Abstract

3C 454.3 is frequently observed in the flaring state. The long-term light curve of this source has been analyzed with 9 yr (2008 August–2017 July) of data from the Fermi-LAT detector. We have identified five flares and one quiescent state. The flares have substructures with many peaks during the flaring phase. We have estimated the rise and decay time of the flares and compared with flares of other similar sources. The modeling of gamma-ray spectral energy distributions shows in most cases that a log-parabola function gives the best fit to the data. We have done time-dependent leptonic modeling of two of the flares, for which simultaneous multiwavelength data are available. These two long-lasting flares, Flare-2A and Flare-2D, continued for 95 and 133 days, respectively. We have used the average values of Doppler factor, injected luminosity in electrons, size of the emission region, and the magnetic field in the emission region in modeling these flares. The emission region is assumed to be in the broad-line region in our single-zone model. The energy losses (synchrotron, synchrotron self-Compton, external Compton) and escape of electrons from the emission region have been included while doing the modeling. Although the total jet powers required to model these flares with the leptonic model are higher compared to other sources, they are always found to be lower than the Eddington luminosity of 3C 454.3. We also select some flaring peaks and show that the time variation of the Doppler factor or the injected luminosity in electrons over short timescales can explain their light curves.

Unified Astronomy Thesaurus concepts: Galactic and extragalactic astronomy (563); Extragalactic astronomy (506); Quasars (1319); Active galactic nuclei (16); Blazars (164); Jets (870)

Supporting material: machine-readable table

1. Introduction

The flat-spectrum radio quasar (FSRQ) 3C 454.3, located at redshift 0.859, is frequently monitored owing to its high flux variability. During an intense flare in 1992, it was observed by EGRET (Hartman et al. 1992, 1993), when its flux varied in the range of (0.4–1.4) $\times$ 10^{-6} photons cm^{-2} s^{-1}. Subsequently, 3C 454.3 remained a source of interest for multiwavelength observations owing to its variable nature. This source was active in 2000 and even more in 2005. The 2005 outburst was recorded in optical and X-ray frequencies (Giommi et al. 2006). The high activity of 3C 454.3 in fall 2007 was observed by the Whole Earth Blazar Telescope (WEBT) in radio to optical frequencies. The gamma-ray satellite Astro-rivelatore Gamma a Immagini LEggero (AGILE) detected this source in late 2007 July and November–December (Raiteri et al. 2008).

The AGILE 2007 November campaign was reported by Vercellone et al. (2009). AGILE, the International Gamma-ray Astrophysics Laboratory, Swift, the WEBT consortium, and the optical–near-IR telescope Rapid Eye Mount (REM) observed 3C 454.3 during the campaign. During 3 weeks of the observation period, the average gamma-ray flux above 100 MeV was 1.7 $\times$ 10^{-6} photons cm^{-2} s^{-1}. The source was extremely variable in the optical band. The gamma-ray emission was found to be correlated with optical emission. The AGILE 2007 December campaign (Donnarumma et al. 2009) observed this source with average flux 2.5 $\times$ 10^{-6} photons cm^{-2} s^{-1} above 100 MeV, and the delay between gamma-ray and optical emissions was found to be 12 hr.

Fermi-LAT has been regularly monitoring this source since 2008 July. An intense flare was observed during 2008 July 7–October 6, and the average flux above 100 MeV was found to be 3 $\times$ 10^{-6} photons cm^{-2} s^{-1}. Strong, distinct, and symmetric flares were observed with an increase in flux by several factors within 3 days (Abdo et al. 2009).

A multiwavelength study was carried out to find out the correlation between emissions in different wavelengths (IR, optical, UV, X-ray, and gamma-ray) during 2008 August–December (Bonninng et al. 2009). They found a correlation of less than a day between light curves in different frequencies except in X-rays. The X-ray flux is not correlated with fluxes in gamma-ray or longer wavelengths.

A similar result was also reported for the high state in 2009 November–December (Gaur et al. 2011). They found a strong correlation between optical and gamma-ray emission with a time lag of 4 days, but the X-ray emission is not correlated to any of them.

The strong flare of 3C 454.3 in 2009 during December 3–12 in gamma-rays, X-rays, and optical/near-IR bands was studied by Gupta et al. (2017). Optical polarization measurements showed dramatic changes during the flare, with a strong anticorrelation between optical flux and degree of polarization during the decay phase of the flare. They used a one-zone model with variations in magnetic field, spectral break energies, and normalization to fit the spectral energy distributions (SEDs) at different times.

Raiteri et al. (2011) studied the multiwavelength light curves in 18 bands to analyze the flux variability for the period 2008 April–2010 March. The X-ray flux variation appeared to follow the gamma-ray and optical ones by about 0.5 and 1 day, respectively. They speculated that there is a slight variable misalignment between the synchrotron and Comptonization zones, which can explain the increases in gamma-ray and X-ray flux levels in 2009–2010, as well as the change in gamma-ray-to-optical flux ratio at the peaks of the outbursts.

During high gamma-ray states of 3C 454.3 in 2009 December and 2010 April and November, the parsec-scale jet was highly active. Superluminal radio knots K09 and K10 were found to be associated with fall 2009 and 2010 outbursts (Jorstad et al. 2013). It was argued that gamma-ray outbursts of as short as 3 hr duration can occur on parsec scales if flares take place in localized regions such as turbulent cells.

Multiwavelength variations of 3C 454.3 during the 2010 November–2011 January outburst were studied previously (Wehrle et al. 2012). Their discrete correlation analysis of the millimeter, far-infrared, and gamma-ray light curves showed simultaneous variations indicating their common origin. They located the site of outburst in the parsec-scale "core." In their model the turbulent plasma crosses a conical shock in the parsec-scale region of the jet. The seed photons for inverse Compton emission are produced in nonthermal radiation by a Mach disk, thermal emission from hot dust, or synchrotron emission from moving plasma. Extremely high polarization in the 2010 outbursts was reported by Sasada et al. (2014).

Long-term and rapid radio variability of 3C 454.3 was studied on the RATAN-600 radio telescope of the Special Astrophysical Observatory at 4.6, 8.2, 11.2, and 21.7 GHz and on the 32 m Zelenchuk and Badary radio telescopes (Gorshkov et al. 2018). Two flares were observed in the long-term light curve in 2010 and in 2015–2017. The delay in the maximum of the first flare at 4.85 GHz relative to the maximum at 21.7 GHz was 6 months. Intraday variability was detected at 8.57 GHz on the 32 m telescopes in 30 of 61 successful observations, and it was found to be correlated with the maxima of the flares. The characteristic timescale for this variability was found to be 2–10 hr.

Multiwavelength temporal variability of 3C 454.3 for the gamma-ray high state during 2014 May–December was studied by Kushwaha et al. (2017). Their multi-band correlation study showed that the source was initially showing no lags between the IR and gamma-ray, optical and gamma-ray, and IR and optical emission, but later gamma-ray emission lagged behind IR/optical by 3 days.

Fermi-LAT observations of the 2014 May–July outburst were studied by Britto et al. (2016). The average flux during the highest state from 2014 June 7 to 29 was found to be 7.2×10^{-6} photons cm^{-2} s^{-1}. Several photons above 20 GeV were detected, including one above 45 GeV on MJD 56827. The emission region was speculated to be near the outer boundary of the broad-line region (BLR). Temporal correlation between the optical and gamma-ray flux variations in the blazar 3C 454.3 has been studied with 9 yr of Fermi-LAT data (Rajput et al. 2019). Out of four epochs of intense optical flares, in two epochs the gamma-ray and optical flares are found to be correlated. In the other two epochs gamma-rays are weak or absent.

The long-term optical spectroscopic variations of blazar 3C 454.3 have recently been investigated with 10 yr of data from the Steward Observatory (Nalewajko et al. 2019). The data revealed that the line flux from the BLR changed dramatically with the blazar activity from a very high state in 2010 to a significantly low state in 2012. Inverse Compton emission of relativistic electrons by the seed photons from BLR is the well-established scenario for explaining gamma-ray emission from FSRQs. Due to this reason, the radius of the BLR is a crucial input parameter in modeling of multiwavelength emission from FSRQs. They have obtained the lower bound on the radius of the BLR to be 0.28 pc.

The long-term variability for the period between 2008 February and 2016 April in radio, IR, and optical bands has been analyzed recently by Sarkar et al. (2019). This source showed significant multiwavelength variability with the timescale of variability in the range of months to years. The variations in radio band have been observed to be lagging behind the variations in optical/IR bands by 15–100 days. Strong correlation in optical/IR bands indicates their cospatial origin. They inferred from their analysis that the emission regions change their orientation with our line of sight as the time lag between radio and optical/IR emission varies over the years.

Recently, Weaver et al. (2019) analyzed the uniquely structured multifrequency outburst of 2016 June. This outburst was monitored in optical R band by several ground-based telescopes in photometric and polarimetric modes, as well as by the Fermi-LAT gamma-ray detector. Intraday variability continued throughout the outburst. They constrained the Doppler factor and the size of the emission region from the observed minimum variability timescale.

Leptonic and lepto-hadronic models have been used previously to model the multiwavelength SEDs. In MHD jet launching models a large-scale poloidal magnetic field at the jet base extends to a helical magnetic field downstream along the jet. A large-scale ordered helical magnetic field at a distance of hundreds of parsecs was used by Zamaninasab & Savolainen (2013) to explain the radio emission of 3C 454.3. Several theoretical models were proposed to explain the SEDs of 3C 454.3 (Finke & Dermer 2010; Cerruti et al. 2013; Hunger & Reimer 2016). The flare observed during 2010 November is well explained by the one-zone lepto-hadronic model by Diltz & Böttcher (2016). Another flare in 2015 August was observed with simultaneous data in optical, UV, X-ray, and gamma-ray energy (Shah et al. 2017). They suggested that X-ray and gamma-ray emission of 3C 454.3 cannot be attributed to a single emission zone and both synchrotron self-Compton (SSC) and external Compton (EC) mechanisms are required to explain the data. They further suggested that the flare region lies beyond the BLR of this source.

Motivated by the earlier studies, we have analyzed the Fermi-LAT data from 2008 August to 2017 July to identify the flares of 3C 454.3 and study their characteristics. In Section 2 we discuss the Fermi-LAT and Swift-XRT/UVOT data analysis. In Section 3 the flaring states of 3C 454.3 are identified from the 9 yr gamma-ray light curve. The flares are studied in Section 4, and their substructures and peaks are identified. The variability time in gamma-rays is calculated by scanning the light curves. The SEDs of the flares in gamma-rays are studied in Section 5. In Section 6 we discuss the multiwavelength modeling of two flares. In Section 7 we discuss how a time-dependent Doppler factor or injected luminosity in electrons can explain the flare peaks. Our results are discussed in Section 8, and conclusions are drawn in Section 9.

2. Data Analysis

2.1. Fermi-LAT Analysis

Fermi-LAT (Large Area Telescope) is an imaging pair conversion telescope, which covers a γ-ray energy range from 20 MeV to >300 GeV with energy resolution <15% at energy >100 Gev (Atwood et al. 2009). A detailed description of LAT

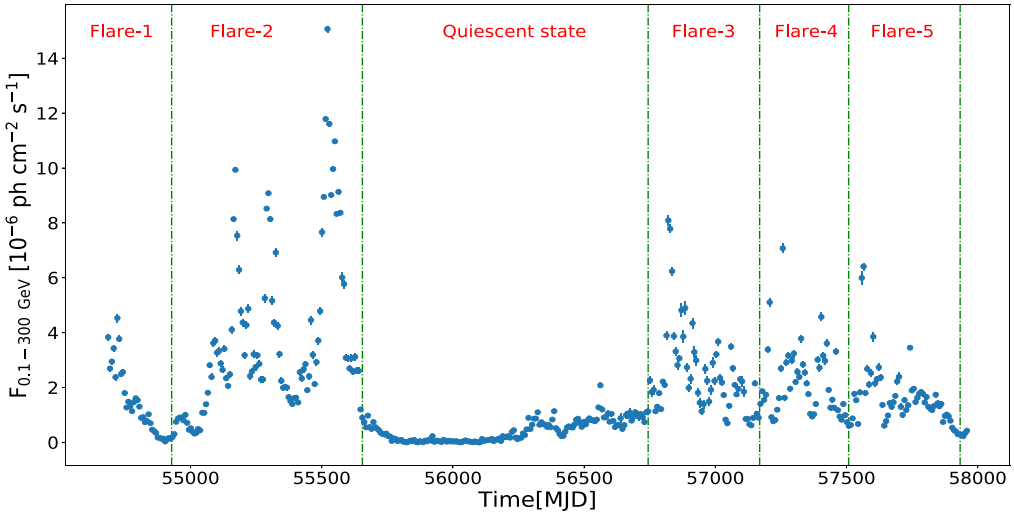

Figure 1. The 7-day binning light curve of 3C 454.3 (MJD 54686−57959). We have identified five major flares (shown by the dashed green lines).

characteristics has been provided on the Fermi website.[1] Fermi typically scans the entire sky in survey mode with a time period of ∼3.2 hr. We have extracted the data of the blazar 3C 454.3 source from FSSC's website data server[2] over a period of 9 yr (2008 August–2017 July) and analyzed them with the help of Fermi science tool software package version-1.0.10, which includes a galactic diffuse emission model (`gll_iem_v06.fits`) and extragalactic isotropic diffuse emission model (`iso_P8R2_SOURCE_V6_v06.txt`). The "unbinned likelihood analysis" (using python) method has been used to analyze the Fermi-LAT Pass8 data with appropriate selections and recommended cuts. The photon-like events are classified as "evclass = 128, evtype = 3," with energies ranging from 100 MeV to 300 GeV. We have extracted the photons from a radius (region of interest or ROI) of 10° around the source and used a maximum zenith angle value of 90°, which is the standard value provided by the LAT instrument team, in order to avoid the γ-ray detection from Earth's limb. Filter expression "(`DATA_QUAL` > 0)&(`LAT_CONFIG` == 1)" is implemented to select the good time interval data, which are recommended by the LAT team. The live time, exposure map, and diffuse response of the instrument have been computed subsequently for each event with the latest instrument response function (IRF) "`P8R2_SOURCE_V6`." To localize the source detection, a quantity called at "test statistic" (TS) is computed, which is defined as

$$\mathrm{TS} = -2\log\left(\frac{L_0}{L_1}\right), \quad (1)$$

where L_0 and L_1 are the maximum likelihood values for a given model without (null hypothesis) and with the point-like source at the position of the source. We have always maintained the criterion to choose the sources with TS ⩾ 25 (corresponds to $\sim(\mathrm{TS})^{1/2}\sigma$ or 5σ detection level) for each data set. To generate the light curve, we have fixed the model parameters of all the sources within the ROI, excluding our source of interest from the third Fermi catalog (3FGL; Acero et al. 2015). In our work, we have studied the light curve of three different time bins: 7 days, 1 day, and 6 hr. Apart from this, we have also generated the spectral data points for different periods of activity in the energy range 0.1 GeV ⩽ E ⩽ 300 GeV.

2.2. *Swift-XRT/UVOT*

We have analyzed the archival data from the Swift-XRT/UVOT for the source 3C 454.3 during the time period of 2009–2011 April (∼2 yr), which have been retrieved from the HEASARC website.[3] A total of 203 observations were made in this time span. A task "*xrtpipeline*" (version 0.13.2) has been used to process the XRT data (Burrows et al. 2005; 0.2–10 keV) files for each observation set. The latest calibration files (CALDB version of 20160609) and standard screening criteria have been implemented in this process. We have chosen a circular radius of 20″ around the source to analyze the XRT data. A background region is also chosen of the same radius (20″) but far away from the source region. A tool "*xselect*" has been used to extract the X-ray light curve and spectra. The tools called "*xrtmkarf*" and "*grppha*" have been used to create the ancillary response file and group the spectra of 30 counts bin^{-1}, respectively. Subsequently, the grouped spectra have been modeled in XSPEC (version 12.10.0) with the "*tbabs∗log parabola*" model and with the fixed neutral hydrogen column density of $n_{\mathrm{H}} = 1.34 \times 10^{21}$ cm^{-2} (Villata et al. 2006).

The source 3C 454.3 was also observed by the Swift Ultraviolet/Optical Telescope (UVOT; Roming et al. 2005) in all six filters: U, V, B, $W1$, $M2$, and $W2$. The source region has been extracted from the 10″ circular region around the source, and the background region has also been chosen with a radius of 25″ away from the source. The source magnitudes have been extracted by the task "*uvotsource*" and corrected for galactic extinction (Schlafly & Finkbeiner 2011). Subsequently, these magnitudes have been converted into flux by using the zero-points (Breeveld et al. 2011) and conversion factors (Larionov et al. 2016).

3. Flaring State of 3C 454.3

The 7-day binning gamma-ray light curve of 3C 454.3 has been shown in Figure 1, which is observed by Fermi-LAT from

[1] https://fermi.gsfc.nasa.gov/ssc/data/analysis/software/
[2] https://fermi.gsfc.nasa.gov/cgi-bin/ssc/LAT/LATDataQuery.cgi
[3] https://heasarc.gsfc.nasa.gov/cgi-bin/W3Browse/swift.pl

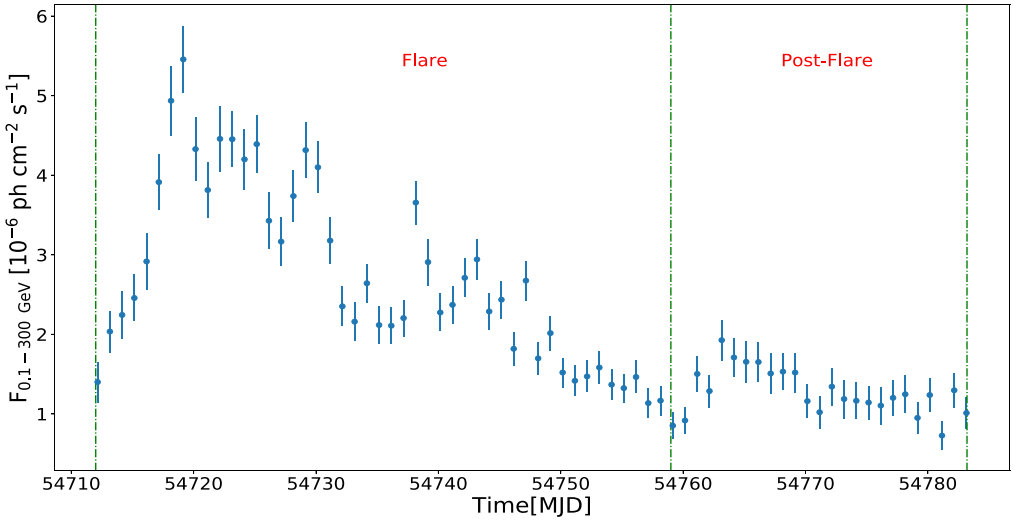

Figure 2. The 1-day binning light curve for Flare-1A. Time durations of all the different periods of activities (shown by the dashed green lines) are MJD 54712 −54759 (flare) and MJD 54759−54783 (post-flare).

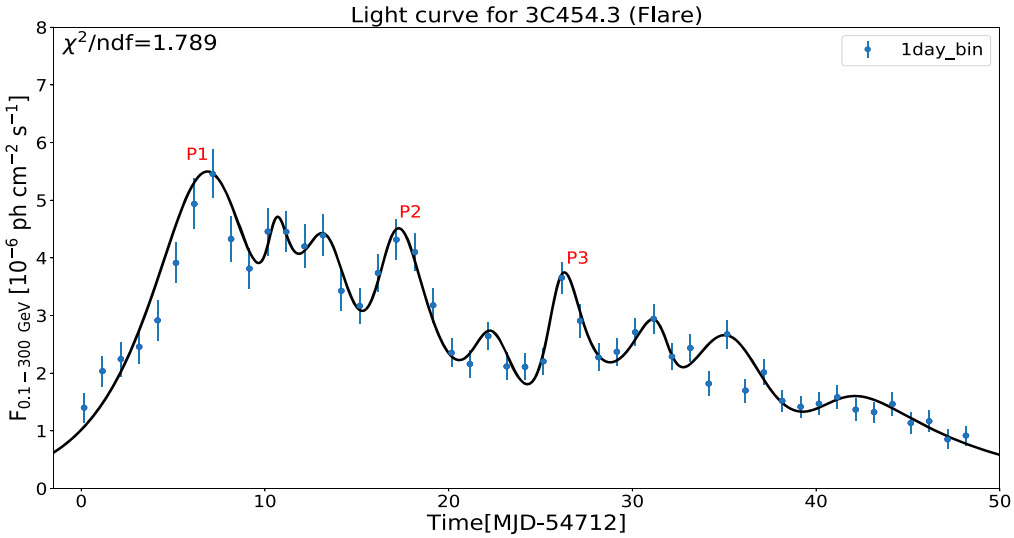

Figure 3. Fitted light curve (fitted by the sum of the exponential function) of Flare-1A of the flare (MJD 54712−54759) epoch.

Table 1
Rising and Decay Time (T_r and T_d) for Given Peak Time (t_0) and Peak Flux (F_0), which Is Calculated by Temporal Fitting of the Light Curve (Flare-1A) with the Sum of the Exponential Function

Flare-1A				
Peak	t_0 (MJD)	F_0 (10^{-6} photons cm^{-2} s^{-1})	T_r (hr)	T_d (hr)
P1	54719.1	5.45 ± 0.42	73.35 ± 4.21	54.79 ± 14.38
P2	54729.1	4.31 ± 0.35	19.95 ± 5.78	57.03 ± 9.96
P3	54738.1	3.66 ± 0.28	15.55 ± 4.91	30.52 ± 9.86

Note. Column (1) represents the peak number. Here results are shown for 1-day binning. All of the flare data are provided in the machine-readable table.
(This table is available in its entirety in machine-readable form.)

MJD 54686 (2008 August) to MJD 57959 (2017 July). From this 9 yr light-curve history we have clearly identified (shown by the dashed green lines) five major flaring states and one quiescent state. As alluded to previously (Prince et al. 2017), we have defined these states as Flare-1, Flare-2, Flare-3, Flare-4, and Flare-5, with time spans of MJD 54683−54928, MJD 54928−55650, MJD 56744−57169, MJD 57169−57508, and MJD 57508−57933, respectively. The quiescent state has a time duration of almost 3 yr (MJD 55650−56744). In our work, we are more interested in flaring states, and hence further analysis has been carried out on these states only. We have studied these flares in detail for 1-day binning (where the substructures are not clearly visible) and then 6 hr binning to identify the various substructures properly.

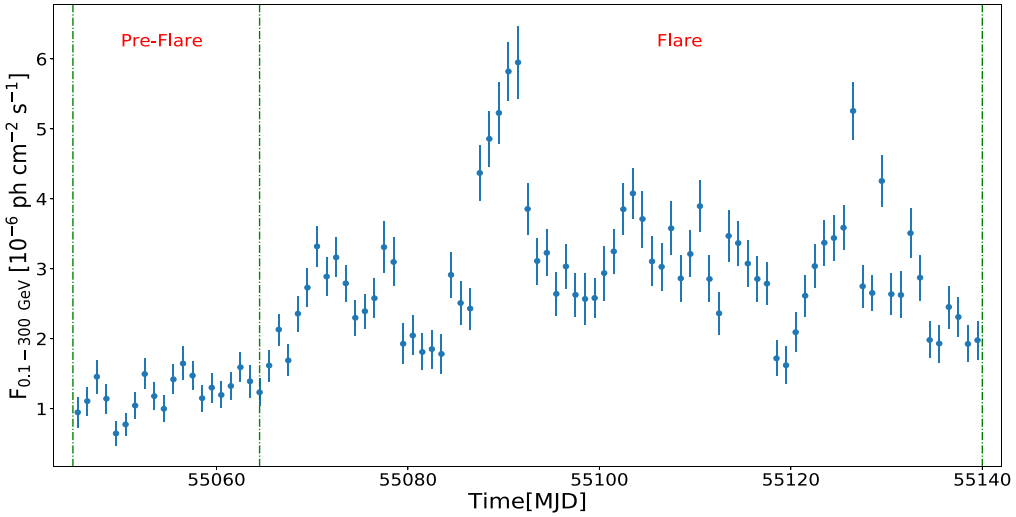

Figure 4. The 1-day binning light curve for Flare-2A. Time durations of all the different periods of activities (shown by the dashed green lines) are MJD 55045 −55064 (pre-flare) and MJD 55064−55140 (flare).

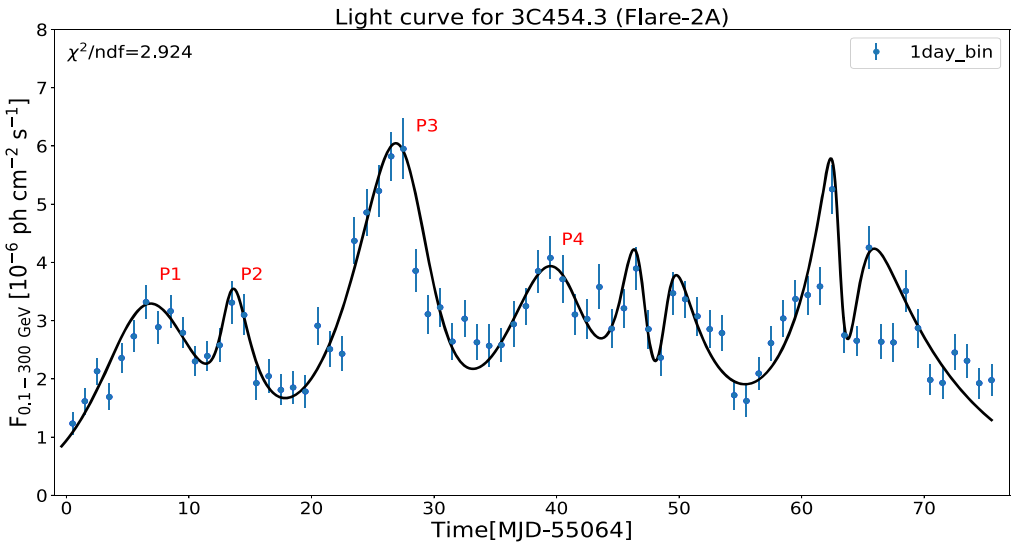

Figure 5. Fitted light curve (fitted by the sum of the exponential function) of Flare-2A of the flare (MJD 55064−55140) epoch.

Table 2
Constant Flux Value for Four Substructures

Substructures	Constant Flux (10^{-6} $F_{0.1-300\ \mathrm{GeV}}$ photons cm^{-2} s^{-1})
Flare-4A	1.54 ± 0.13
Flare-4B	1.79 ± 0.23
Flare-4D	1.24 ± 0.13
Flare-5A	0.52 ± 0.07

In the 6 hr binning study we have found several substructures for each flaring state. Flare-1 has only one substructure; we labeled that as Flare-1A. Four substructures were noticed in Flare-2, defined as Flare-2A, Flare-2B, Flare-2C, and Flare-2D. Flare-3A and Flare-3B are two substructures of Flare-3. Similarly, Flare-4 and Flare-5 have four (Flare-4A, Flare-4B, Flare-4C, and Flare-4D) and two (Flare-5A and Flare-5B) substructures, respectively. There are two substructures (Flare-1A and Flare-2A) that are well observed in 1-day binning, but we are unable to study them in 6 hr binning owing to large error in the photon flux.

4. Gamma-Ray Light-curve History of Flares and Variability

We have studied each substructure separately and observed different states of activity (e.g., pre-flare, flare, post-flare) as shown in 6 hr binning light curve. There are various ways in which one can define the different states of the source. One of these methods is to estimate the average flux for each time period (pre-flare, flare, etc.) and compare their values. The flare period can be defined as the period when the average flux is more than 3–4 times its average flux during the pre-flare period. The other way is to estimate the fractional variability in each period. The flux is high and more variable during the flaring period, while during pre-flare or post-flare the fractional variability is less and also the flux will be constant for a long period of time (e.g., Prince et al. 2018). In our case we have used both these methods to identify the various states of the source, and our result is consistent with both these methods.

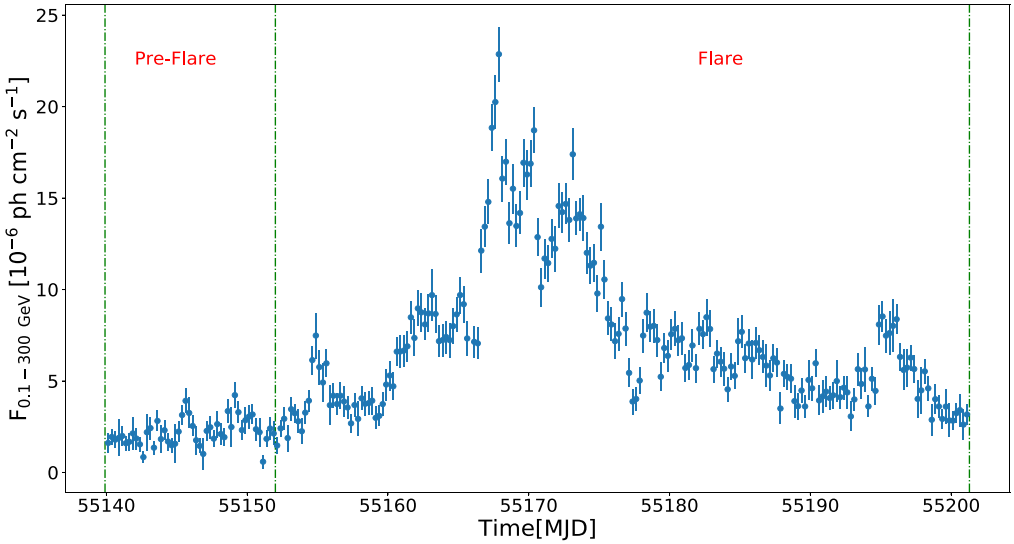

Figure 6. The 6 hr binning light curve for Flare-2B. Time durations of all the different periods of activities (shown by the dashed green lines) are MJD 55140−55152 (pre-flare) and MJD 55152−55201 (flare).

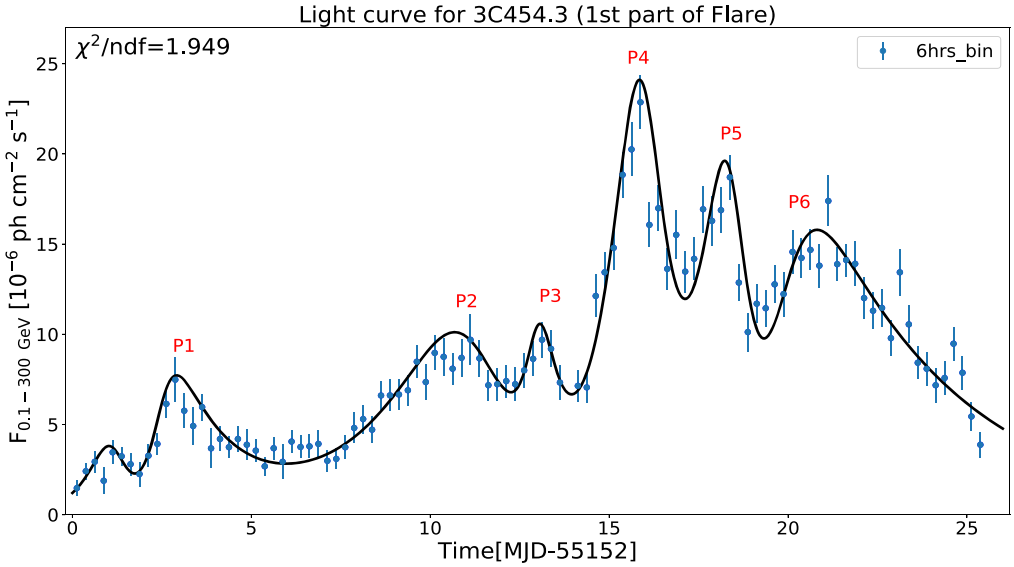

Figure 7. Fitted light curve (fitted by the sum of the exponential function) of Flare-2B for the first part of the flare (MJD 55152−55177) epoch.

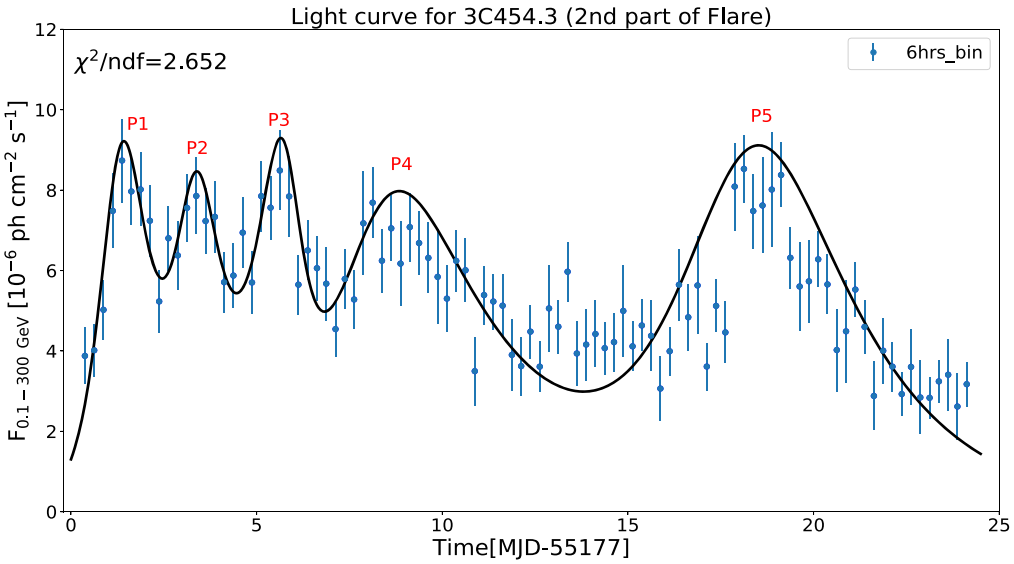

Figure 8. Fitted light curve (fitted by the sum of the exponential function) of Flare-2B for the second part of the flare (MJD 55177−55201) epoch.

Table 3
Results of Variability Time (t_{var}), which Is Calculated by Scanning the 6 hr Binning γ-Ray Light Curve for Each Flare

$T_{start}(t_1)$ (MJD)	$T_{stop}(t_2)$ (MJD)	Flux Start$[F(t_1)]$ (10^{-6} photons cm^{-2} s^{-1})	Flux Stop$[F(t_2)]$ (10^{-6} photons cm^{-2} s^{-1})	$\tau_{d/h}$ (hr)	$\Delta t_{d/h}$ (hr)	Rise/Decay
			Flare-1A			
54728.125	54728.375	2.37 ± 0.60	5.22 ± 0.77	2.63 ± 0.98	1.41 ± 0.53	R
54744.625	54744.875	1.55 ± 0.34	3.10 ± 0.50	3.00 ± 1.18	1.61 ± 0.63	R
54749.125	54749.375	2.77 ± 0.52	1.27 ± 0.32	−2.67 ± 1.07	−1.44 ± 0.57	D
54756.625	54756.875	1.78 ± 0.40	0.87 ± 0.34	−2.90 ± 1.83	−1.56 ± 0.98	D
			Flare-2A			
55055.375	55055.625	1.12 ± 0.34	2.38 ± 0.56	2.77 ± 1.43	1.49 ± 0.77	R
55061.875	55062.125	0.70 ± 0.28	1.76 ± 0.44	2.24 ± 1.14	1.20 ± 0.61	R
55063.625	55063.875	1.99 ± 0.49	0.99 ± 0.32	−2.97 ± 1.75	−1.60 ± 0.94	D
55064.875	55065.125	1.36 ± 0.38	0.65 ± 0.30	−2.79 ± 2.04	−1.50 ± 1.10	D
55068.125	55068.375	1.11 ± 0.34	3.25 ± 0.57	1.93 ± 0.64	1.04 ± 0.34	R
55110.875	55111.125	5.16 ± 0.90	2.46 ± 0.68	−2.80 ± 1.24	1.51 ± 0.67	R
55111.375	55111.625	4.73 ± 0.76	2.32 ± 0.52	−2.90 ± 1.11	1.56 ± 0.60	R
55118.625	55118.875	1.00 ± 0.36	2.03 ± 0.58	2.94 ± 1.93	1.58 ± 1.04	R
55129.625	55129.875	3.66 ± 0.65	7.62 ± 0.88	2.84 ± 0.82	1.53 ± 0.44	R
55129.875	55130.125	7.62 ± 0.88	2.60 ± 0.62	−1.94 ± 0.48	1.04 ± 0.26	R
55138.375	55138.625	1.18 ± 0.37	2.75 ± 0.53	2.46 ± 1.07	1.34 ± 0.57	R
			Flare-2B			
55138.125	55138.375	1.19 ± 0.37	2.75 ± 0.54	2.48 ± 1.09	1.33 ± 0.59	R
55143.375	55143.625	1.36 ± 0.37	2.82 ± 0.57	2.85 ± 1.32	1.53 ± 0.71	R
			Flare-2C			
55256.375	55256.625	3.59 ± 0.64	1.47 ± 0.59	−2.33 ± 1.14	−1.25 ± 0.61	D
55256.625	55256.875	1.47 ± 0.59	3.23 ± 0.66	2.64 ± 1.51	1.42 ± 0.81	R
55260.125	55256.375	2.64 ± 0.52	1.16 ± 0.39	−2.53 ± 1.20	−1.36 ± 0.64	D
55277.375	55277.625	1.94 ± 0.54	3.98 ± 0.10	2.89 ± 1.12	1.55 ± 0.60	R
55277.625	55277.875	3.98 ± 0.10	1.92 ± 0.51	−2.85 ± 1.04	−1.53 ± 0.56	D
55278.125	55278.375	1.73 ± 0.46	3.78 ± 0.72	2.66 ± 1.11	1.43 ± 0.60	R
55279.875	55280.125	3.83 ± 0.83	1.83 ± 0.46	−2.81 ± 1.26	−1.51 ± 0.68	D
55306.125	55306.375	8.56 ± 0.92	4.14 ± 0.12	−2.86 ± 0.43	−1.54 ± 0.23	D
55332.375	55332.625	5.23 ± 0.72	2.52 ± 0.51	−2.85 ± 0.95	−1.53 ± 0.51	D
			Flare-2D			
55452.375	55452.625	1.35 ± 0.47	2.70 ± 0.57	3.00 ± 1.76	1.61 ± 1.95	R
55455.125	55455.375	2.65 ± 0.92	5.30 ± 0.73	3.00 ± 1.62	1.61 ± 0.87	R
55459.375	55459.625	6.04 ± 0.78	2.80 ± 0.51	−2.70 ± 0.78	−1.45 ± 0.42	D
55468.625	55468.875	1.57 ± 0.48	3.59 ± 0.87	2.51 ± 1.18	1.35 ± 0.63	R
55475.875	55476.125	1.51 ± 0.50	3.01 ± 0.77	3.01 ± 1.83	1.62 ± 0.98	R
55478.625	55478.875	2.87 ± 0.57	1.09 ± 0.42	−2.14 ± 0.96	−1.15 ± 0.52	D
55478.875	55479.125	1.09 ± 0.42	2.38 ± 0.62	2.66 ± 1.58	1.43 ± 0.85	R
			Flare-3A			
56807.625	56807.875	1.03 ± 0.34	3.32 ± 0.59	1.78 ± 0.57	0.96 ± 0.31	R
56808.125	56808.375	2.12 ± 0.51	4.46 ± 1.08	2.79 ± 1.28	1.50 ± 0.69	R
56808.375	56808.625	4.46 ± 1.08	1.78 ± 0.52	−2.26 ± 0.93	−1.21 ± 0.50	D
56812.375	56812.625	1.44 ± 0.57	3.95 ± 0.87	2.06 ± 0.92	1.11 ± 0.50	R
56815.625	56815.875	2.63 ± 0.71	8.95 ± 0.48	1.70 ± 0.38	0.91 ± 0.20	R
56826.875	56827.125	3.58 ± 0.60	9.28 ± 1.03	2.18 ± 0.46	1.17 ± 0.25	R
56839.125	56839.375	6.28 ± 0.79	2.94 ± 0.78	−2.74 ± 1.06	−1.47 ± 0.57	D
56841.375	56841.625	2.21 ± 0.65	5.77 ± 0.74	2.17 ± 0.72	1.17 ± 0.41	R
56844.375	56844.625	1.10 ± 0.41	2.32 ± 0.52	2.79 ± 1.62	1.87 ± 0.87	R
56844.875	56845.125	2.31 ± 0.63	4.78 ± 1.01	2.86 ± 1.36	1.54 ± 0.73	R
56847.125	56847.375	2.11 ± 0.95	4.99 ± 1.30	2.41 ± 1.46	1.30 ± 0.73	R

Note. $\Delta t_{d/h}$ (Column (6)) is the redshift-corrected doubling/halving time. Rise/Decay (Column (7)) represents the behavior of the flux in a given time interval between T_{start} (Column (1)) and T_{stop} (Column (2)). Results are shown here from MJD 54728 to 57207.

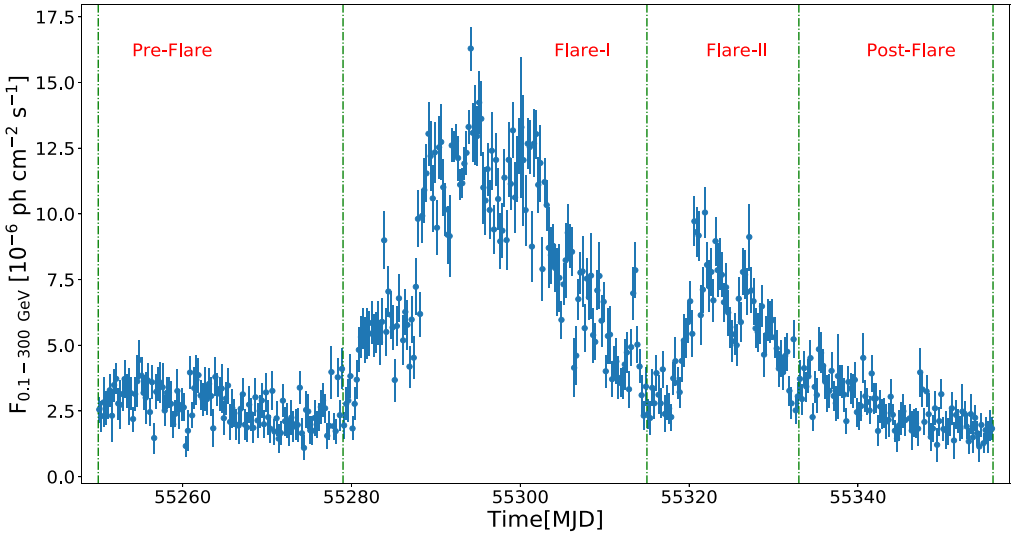

Figure 9. The 6 hr binning light curve for Flare-2C. Time durations of all the different periods of activities (shown by the dashed green lines) are MJD 55250−55279 (pre-flare), MJD 55279−55315 (Flare-I), MJD 55315−55333 (Flare-II), and MJD 55333−55356 (post-flare).

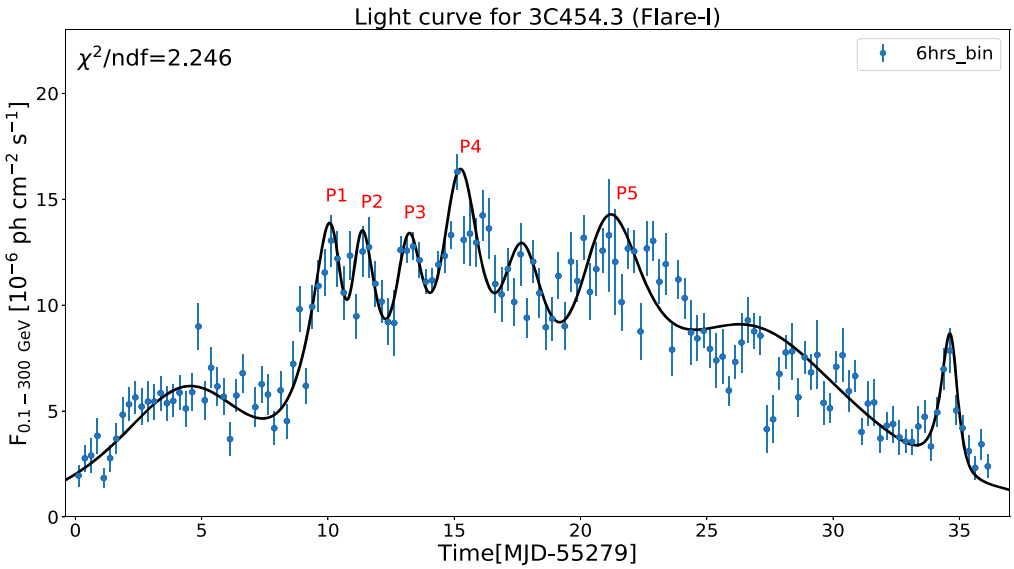

Figure 10. Fitted light curve (fitted by the sum of the exponential function) of Flare-2C for the Flare-I (MJD 55279−55315) epoch.

We have fitted only the flaring state of each substructure with the sum of the exponential function to show the temporal evolution. These fitted flares have characteristic rising and decay times for different peaks (P1, P2, etc.). The functional form of the sum of the exponential function is given by (Abdo et al. 2010a)

$$F(t) = 2F_0\left[\exp\left(\frac{t_0 - t}{T_r}\right) + \exp\left(\frac{t - t_0}{T_d}\right)\right]^{-1}, \quad (2)$$

where t_0 is the peak time and F_0 is the flux observed at time t_0. T_r and T_d represent the rising and decay times, respectively. For a few flares we are able to show the constant state (shown by the horizontal gray line). All reported gamma-ray fluxes throughout the paper are mentioned in units of 10^{-6} photons cm^{-2} s^{-1}.

4.1. Flare-1

A 6 hr binning has been carried out for Flare-1 during MJD 54683−54928. We have found only one substructure (defined as Flare-1A) in this period, but we are unable to identify the peaks in this binning owing to rapid fluctuation and large error in photon counts. For this reason we have shown the substructure in 1-day binning in Figure 2.

Flare-1A (MJD 54712−54783) has two distinct states of activity; these are defined as flare and post-flare. There are several peaks in the flare epoch (shown in Figure 3), but we have considered only three prominent major peaks, which are labeled as P1, P2, and P3, with the fluxes of 5.45 ± 0.42, 4.31 ± 0.35, and 3.66 ± 0.28 at times MJD 54719.1, 54729.1, and 54738.1, respectively. The details of the modeling parameters (T_r and T_d) of Flare-1A and all the subsequent substructures have been elucidated in Table 1 in machine-readable format. The post-flare

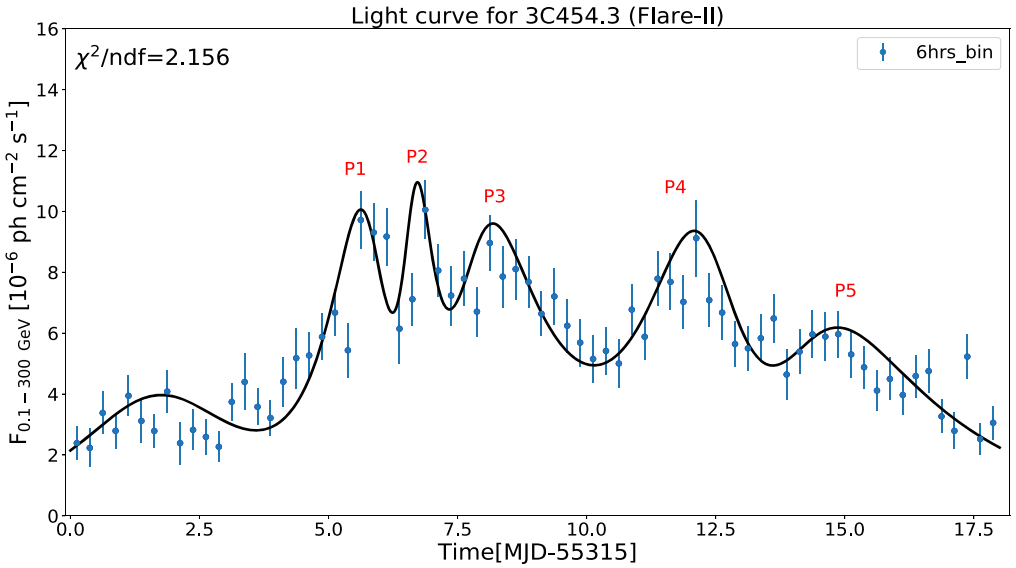

Figure 11. Fitted light curve (fitted by the sum of the exponential function) of Flare-2C for the Flare-II (MJD 55315−55333) epoch.

epoch (MJD 54759−54783) follows immediately after the flare epoch, with a time span of 24 days, which has small variations in flux, and the average flux is found to be 1.27 ± 0.04.

4.2. Flare-2

We have performed 6 hr binning of the light curve of Flare-2 during MJD 54928−55650 and identified four substructures (Flare-2A, Flare-2B, Flare-2C, and Flare-2D). As with Flare-1A, we are unable to study the temporal evolution of Flare-2A in 6 hr binning owing to a large error in flux. Here 1-day binning light curves of Flare-2A are considered for further study, which are shown in Figure 4 and the fitted light curves are shown in Figure 5. The 6 hr binning light curves of Flare-2B, Flare-2C, and Flare-2D are presented in Figures 6, 9, and 12, respectively.

Flare-2A shows two different phases during MJD 55045 −55140, which are labeled as pre-flare and flare. The pre-flare epoch has a time span of 19 days (MJD 55045−55064), with an average flux of 1.22 ± 0.04. After that, the source enters into a flaring state with a time duration of MJD 55064−55140. Figure 5 shows the fitted light curve of the flaring state in 1-day binning, which has four prominent peaks (P1, P2, P3, and P4) with fluxes of 3.32 ± 0.29, 3.31 ± 0.36, 5.95 ± 0.52, and 4.08 ± 0.36 at MJD 55070.5, 55077.5, 55091.5, and 55103.5, respectively.

Flare-2B (MJD 55140−55201) also shows two different states of activity regions: pre-flare and flare. Pre-flare has been considered from MJD 55140−55152, during which flux does not vary much. The rest of the region of the light curve is considered as flare (MJD 55152−55201). Figures 7 and 8 represent the fitted light curve of the flaring state in two different parts, as we are unable to fit the entire flare in a single plot. In the first part of the flare (Figure 7, MJD 55152 −55177), six major peaks (P1, P2, P3, P4, P5, and P6) are observed at MJD 55154.9, 55163.1, 55165.1 55167.9, 55170.4, 55172.1 with fluxes (F_0) of 7.48 ± 1.24, 9.69 ± 1.41, 9.69 ± 0.99, 22.86 ± 1.48, 18.70 ± 1.24, and 14.56 ± 1.21, respectively. A small hump kind of structure has been observed in the beginning of the light curve during MJD 55152.0 −55153.9 (Figure 7), but we have not considered it as a distinct peak owing to a low flux value. Similarly, five different peaks (P1, P2, P3, P4, and P5) have been noticed in the second part of the flare (Figure 8, MJD 55177−55201). The flux values (F_0) of these peaks are 8.73 ± 1.04, 7.85 ± 0.95, 8.48 ± 0.98, 7.68 ± 0.87, and 8.52 ± 0.83 at MJD 55178.4, 55180.4, 55182.6, 55185.1, and 55195.1, respectively.

There are four different phases of activity (pre-flare, Flare-I, Flare-II, and post-flare) in Flare-2C during MJD 55250 −55356, which are shown in Figure 9. The pre-flare phase has small variation in counts, with an average flux of 2.68 ± 0.06, and then the source goes to the Flare-I and Flare-II states, with a time span of 36 and 18 days, respectively. The fitted light curve of the Flare-I phase (shown in Figure 10) shows five distinguishable major peaks, which are labeled as P1, P2, P3, P4, and P5 respectively. After peak P5 flux counts gradually decrease with a small variation, and at the end of the Flare-I epoch (during MJD 55312.2−55314.7) a sudden increase in flux has been observed, although we have not considered it as a distinct peak since it is far away from the main peaks. The Flare-II (shown in Figure 11) phase also shows five distinctive major peaks (defined as P1, P2, P3, P4, and P5) with fluxes of 9.71 ± 0.94, 10.05 ± 0.95, 7.79 ± 0.90, 9.12 ± 1.26, and 5.96 ± 0.78 at MJD 55320.6, 55321.6, 55322.6, 55327.1, and 55329.4, respectively. After Flare-II photon flux starts to decay slowly and the source comes back to its quiescent state, which we have identified as the post-flare phase in Figure 9.

Flare-2D (MJD 55467−55600) is observed to be the most violent substructure in the whole 9 yr of light-curve history with six different phases (shown in Figure 12) of activity: pre-flare, Plateau-I, Flare-I, Flare-II, Plateau-II, and post-flare. There is no rapid fluctuation in flux during MJD 55467 −55480; this phase is considered as the pre-flare phase. After that (MJD 55467), the flux starts to rise slowly up to MJD 55511, which is labeled as the Plateau-I phase, with the average flux of 6.26 ± 0.07. We have identified three major peaks (P1, P2, P3) from the fitted light curve (see Figure 13) of the Flare-I phase with a time duration of 25 days, which has peak fluxes (F_0) of 53.51 ± 2.08, 65.66 ± 2.34, and 80.41 ± 5.92 at MJD 55517.6, 55518.6, and 55519.9, respectively. Peak P3

Table 4
All the Parameters Represented here Are Similar to the Parameters of Table 3, but Results Are Shown here from MJD 57263 to 57762

$T_{start}(t_1)$ (MJD)	$T_{stop}(t_2)$ (MJD)	Flux Start ($F(t_1)$) (10^{-6} photons cm^{-2} s^{-1})	Flux Stop ($F(t_2)$) (10^{-6} photons cm^{-2} s^{-1})	$\tau_{d/h}$ (hr)	$\Delta t_{d/h}$ (hr)	Rise/Decay
			Flare-3B			
57013.625	57013.875	1.91 ± 0.59	4.00 ± 0.97	2.81 ± 1.49	1.51 ± 0.80	R
57013.875	57014.125	4.00 ± 0.97	1.52 ± 1.11	−2.15 ± 1.70	−1.16 ± 0.91	D
57014.125	57014.375	1.52 ± 1.11	3.48 ± 0.56	2.51 ± 2.27	1.35 ± 1.22	R
57019.375	57019.625	2.38 ± 0.45	1.10 ± 0.41	−2.69 ± 1.46	−1.45 ± 0.78	D
			Flare-4A			
57163.875	57164.125	0.65 ± 0.24	1.68 ± 0.43	2.19 ± 1.04	1.18 ± 0.56	R
57165.625	57165.875	1.19 ± 0.43	0.57 ± 0.26	−2.82 ± 2.23	−1.52 ± 1.20	D
57171.375	57171.625	2.59 ± 0.67	1.28 ± 0.40	−2.95 ± 1.70	−1.59 ± 0.91	D
57174.375	57174.625	1.73 ± 0.60	4.33 ± 0.69	2.27 ± 0.94	1.22 ± 0.50	R
57178.125	57178.375	0.62 ± 0.27	1.61 ± 0.51	2.18 ± 1.23	1.17 ± 0.66	R
57182.625	57182.875	1.35 ± 0.45	0.60 ± 0.28	−2.56 ± 1.81	−1.38 ± 0.97	D
57182.875	57183.125	0.60 ± 0.28	1.59 ± 0.43	2.13 ± 1.18	1.14 ± 0.63	R
57185.875	57186.125	3.03 ± 0.59	1.26 ± 0.43	−2.37 ± 1.06	−1.27 ± 0.57	D
57192.875	57193.125	1.47 ± 0.48	3.38 ± 0.74	2.50 ± 1.18	1.34 ± 0.63	R
57194.125	57194.375	2.12 ± 0.56	0.94 ± 0.41	−2.56 ± 1.60	−1.38 ± 0.86	D
57196.375	57196.625	1.25 ± 0.55	2.93 ± 0.69	2.44 ± 1.43	1.31 ± 0.77	R
57198.625	57196.875	7.59 ± 0.79	3.34 ± 0.59	−2.53 ± 0.63	−1.36 ± 0.34	D
57199.875	57200.125	5.64 ± 0.74	2.02 ± 0.61	−2.02 ± 0.65	−1.09 ± 0.35	D
57205.125	57205.375	6.80 ± 0.71	2.52 ± 0.65	−2.09 ± 0.59	−1.12 ± 0.32	D
57205.875	57206.125	2.19 ± 0.61	4.64 ± 0.81	2.77 ± 1.21	1.49 ± 0.65	R
57207.125	57207.375	6.96 ± 0.46	2.74 ± 0.80	−2.23 ± 0.72	−1.20 ± 0.39	D
			Flare-4B			
57263.875	57264.125	1.42 ± 0.45	3.24 ± 0.87	2.52 ± 1.27	1.35 ± 0.68	R
57264.375	57264.625	3.52 ± 0.66	1.65 ± 0.49	−2.74 ± 1.27	−1.47 ± 0.68	D
			Flare-4C			
57396.875	57397.125	3.16 ± 0.82	1.13 ± 0.53	−2.02 ± 1.05	−1.09 ± 0.56	D
57397.125	57397.375	1.13 ± 0.53	3.07 ± 0.72	2.08 ± 1.09	1.12 ± 0.59	R
57397.375	57397.625	3.07 ± 0.72	1.23 ± 0.55	−2.27 ± 1.25	−1.22 ± 0.67	D
57397.625	57397.875	1.23 ± 0.55	3.56 ± 0.78	1.96 ± 0.92	1.05 ± 0.49	R
57397.875	57398.125	3.56 ± 0.78	1.76 ± 0.70	−2.95 ± 1.90	−1.59 ± 1.02	D
57410.625	57410.875	1.39 ± 0.48	3.02 ± 0.64	2.68 ± 1.40	1.44 ± 0.75	R
57419.125	57419.375	2.94 ± 0.58	1.42 ± 0.42	−2.86 ± 1.39	−1.54 ± 0.74	D
57419.375	57419.625	1.42 ± 0.42	2.95 ± 0.77	2.84 ± 1.53	1.53 ± 0.82	R
57430.125	57430.375	1.42 ± 0.40	3.19 ± 0.58	2.57 ± 1.06	1.38 ± 0.57	R
			Flare-4D			
57460.625	57460.375	6.40 ± 0.95	3.25 ± 0.65	−3.07 ± 1.13	−1.65 ± 0.61	D
57463.125	57463.375	1.19 ± 0.44	2.38 ± 0.56	3.00 ± 1.90	1.61 ± 1.02	R
57464.625	57464.875	1.44 ± 0.47	0.65 ± 0.34	−2.61 ± 2.03	−1.40 ± 1.09	D
			Flare-5A			
57552.125	57552.375	2.32 ± 0.62	5.42 ± 1.05	2.45 ± 0.95	1.32 ± 0.51	R
57552.625	57552.875	5.77 ± 0.70	2.93 ± 0.51	−3.07 ± 0.96	−1.65 ± 0.52	D
57553.875	57554.125	3.80 ± 0.56	1.90 ± 0.51	−3.00 ± 1.32	−1.61 ± 0.71	D
57554.875	57555.125	3.27 ± 0.53	1.49 ± 0.77	−2.64 ± 1.82	−1.42 ± 0.98	D
57557.625	57557.875	4.32 ± 1.15	13.55 ± 2.00	1.82 ± 0.48	0.98 ± 0.26	R
57565.125	57565.375	3.75 ± 0.38	1.49 ± 0.25	−2.25 ± 0.48	−1.21 ± 0.26	D
57567.625	57567.875	2.20 ± 0.50	0.88 ± 0.34	−2.27 ± 1.11	−1.22 ± 0.60	D
57567.875	57568.125	0.88 ± 0.34	1.90 ± 0.49	2.70 ± 1.63	1.45 ± 0.88	R
57570.625	57570.875	1.14 ± 0.35	3.68 ± 0.62	1.77 ± 0.53	0.95 ± 0.28	R
57574.125	57574.375	3.12 ± 0.65	1.55 ± 0.49	−2.97 ± 1.60	−1.60 ± 0.86	D
57575.625	57575.875	1.25 ± 0.44	2.68 ± 0.52	2.73 ± 1.44	1.47 ± 0.77	R

corresponds to the highest observed flux in our analysis. A small variation compared to peaks P1, P2, and P3 has been noticed in flux after peak P3 in the Flare-I phase, but no major peak has been identified. The Flare-II state is observed immediately after Flare-I during MJD 55536−55572. A large variation in flux is seen during this period, and six major peaks are observed (see Figure 14). After Flare-II (see Figure 12), the source went into a state of steady diminution of flux defined as

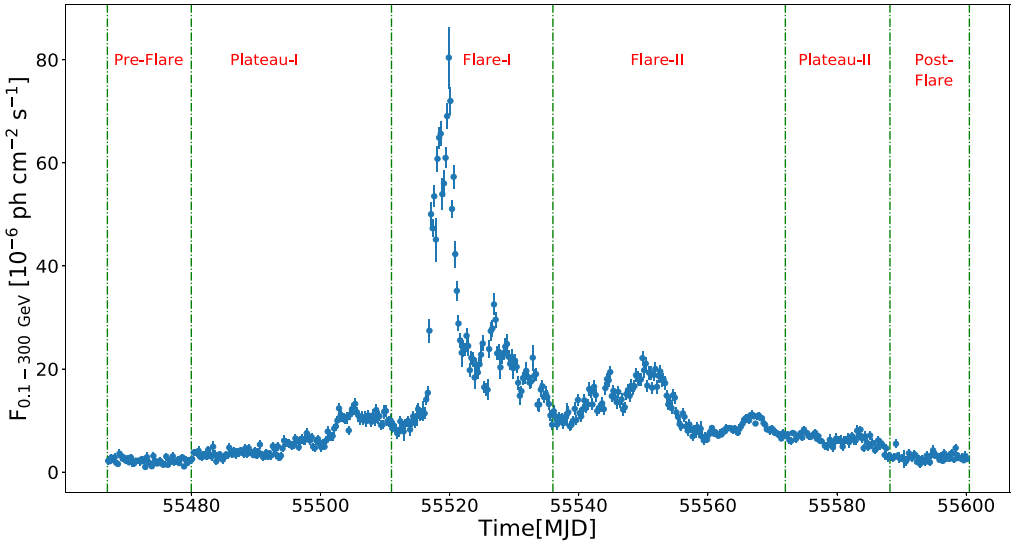

Figure 12. The 6 hr binning light curve for Flare-2D. Time durations of all the different periods of activities (shown by the dashed green lines) are MJD 55467−55480 (pre-flare), MJD 55480−55511 (Plateau-I), MJD 55511−55536 (Flare-I), MJD 55536−55572 (Flare-II), MJD 55572−55588 (Plateau-II), and MJD 55590−55600 (post-flare).

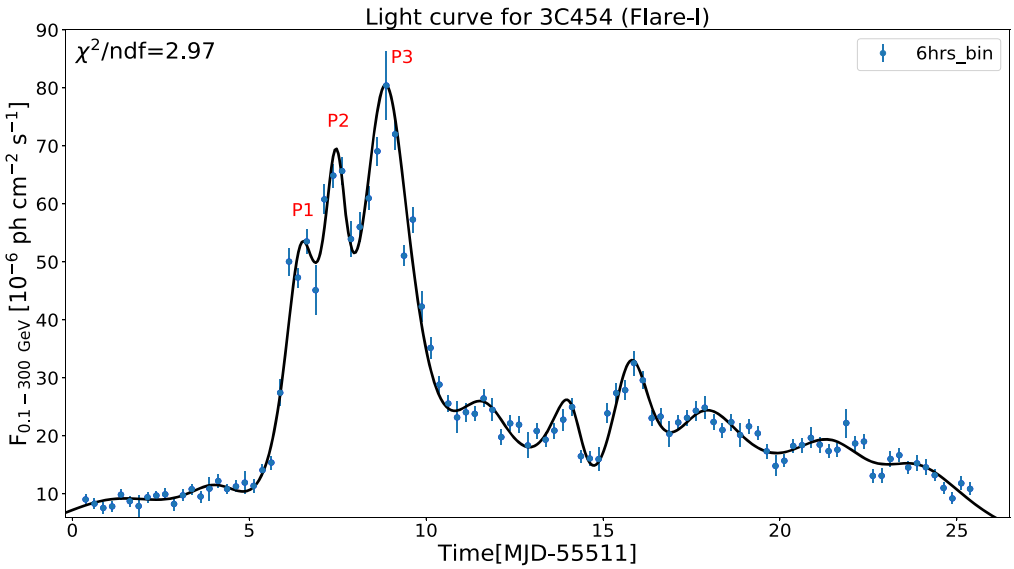

Figure 13. Fitted light curve (fitted by the sum of the exponential function) of Flare-2D for the Flare-I (MJD 55511−55536) epoch.

Plateau-II, which eventually ends up in a post-flare state having almost constant temporal flux distribution.

4.3. Flare-3

Following the similar procedure executed for Flare-2, a 6 hr binning light-curve analysis has also been carried out for Flare-3, and two substructures (Flare-3A and Flare-3B) of moderate time duration (51 and 30 days, respectively) have been found in our study.

Four different epochs of flaring phases are identified in Flare-3A (shown in Figure 15). The time span of pre-flare is about 14 days. After the pre-flare, two flaring states (Flare-I and Flare-II) of similar time durations have been identified, both of which have five prominent peaks, shown in Figures 16 and 17, respectively. Small fluctuations in photon flux are noticed during MJD 56838−56850 with an average flux of 3.56 ± 0.12, which is defined as the post-flare phase (Figure 15).

Flare-3B has the least complicated substructure, with three clear states shown in Figure 18. A pre-flare phase has been identified from MJD 56799 to 57002. In the flare region, the source shows only two major peaks at MJD 57006.1 and 57008.4 with fluxes of 4.95 ± 0.69 and 7.90 ± 0.90, respectively (Figure 19). After spending around 10 days in the flaring state, it comes back again to the constant flux state, which is labeled as post-flare.

4.4. Flare-4

The 6 hr binning of the light curve of Flare-4 shows four distinct substructures, defined as Flare-4A, Flare-4B, Flare-4C, and Flare-4D (Figures 20, 22, 24, and 26). In this period, we are able to fit the light curve by showing the constant flux state (shown by the horizontal gray line) for Flare-4A, Flare-4B, and

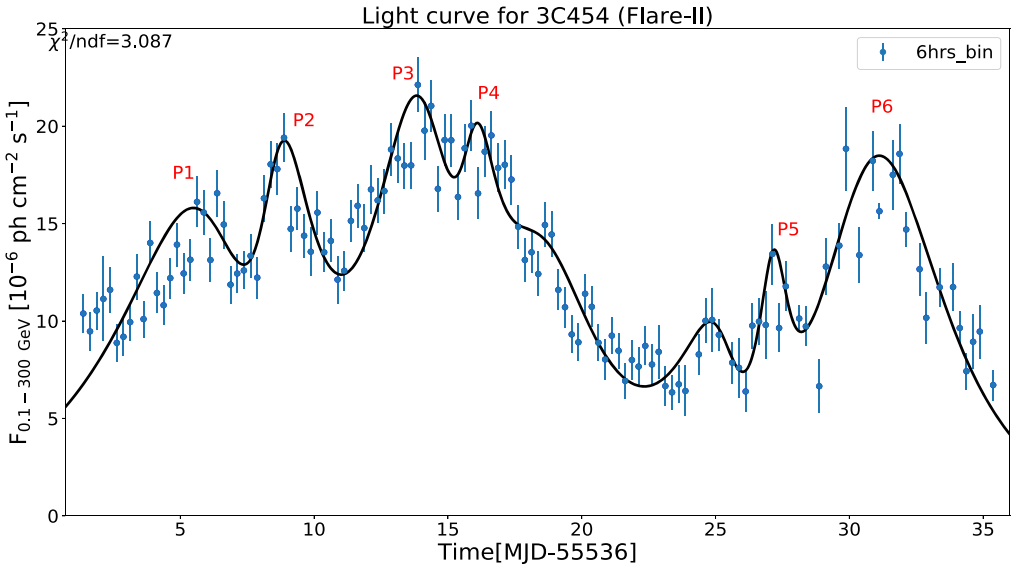

Figure 14. Fitted light curve (fitted by the sum of the exponential function) of Flare-2D for the Flare-II (MJD 55536−55572) epoch.

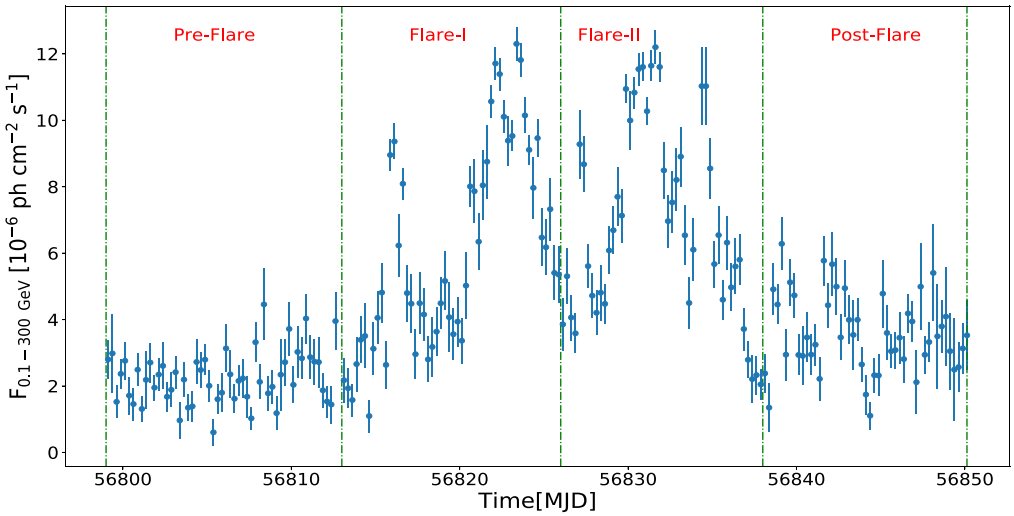

Figure 15. The 6 hr binning light curve for Flare-3A. Time durations of all the different periods of activities (shown by the dashed green lines) are MJD 56799−56813 (pre-flare), MJD 56813−56826 (Flare-I), MJD 56826−56838 (Flare-II), and MJD 56838−56850 (post-flare).

Table 5
All the Parameters Represented here Are Similar to the Parameters of Table 3, but Results Are Shown Here from MJD 57749 to 57762

$T_{start}(t_1)$ (MJD)	$T_{stop}(t_2)$ (MJD)	Flux Start ($F(t_1)$) (10^{-6} photons cm^{-2} s^{-1})	Flux Stop ($F(t_2)$) (10^{-6} photons cm^{-2} s^{-1})	$\tau_{d/h}$ (hr)	$\Delta t_{d/h}$ (hr)	Rise/Decay
		Flare-5B				
57749.375	57749.625	2.72 ± 0.50	1.38 ± 0.52	−3.06 ± 1.89	−1.65 ± 1.02	D
57749.625	57749.875	1.38 ± 0.52	2.97 ± 0.93	2.71 ± 1.73	1.46 ± 0.93	R
57749.875	57750.125	2.97 ± 0.93	1.45 ± 0.46	−2.90 ± 1.80	−1.56 ± 0.97	D
57761.875	57762.125	2.62 ± 0.72	1.18 ± 0.42	−2.61 ± 1.47	−1.40 ± 0.79	D

Flare-4D, which are shown in Figures 21, 23, and 27, respectively.

A pre-flare phase has been noticed in Flare-4A during MJD 57178−57194 with small-scale variation in photon flux, and the average flux is observed to be 1.57 ± 0.08. After that, the source enters into the flaring state (shown in Figure 21) with a time span of 19 days (MJD 57164−57213), which has five well-defined peaks (labeled as P1, P2, P3, P4, and P5). The post-flare region promptly follows after this with a time duration of 19 days and having an almost constant flux throughout this period.

Similarly, Flare-4B also shows three phases (see Figure 22): pre-flare, flare, and post-flare. Pre-flare and post-flare epochs have almost constant flux with average fluxes of 2.50 ± 0.12

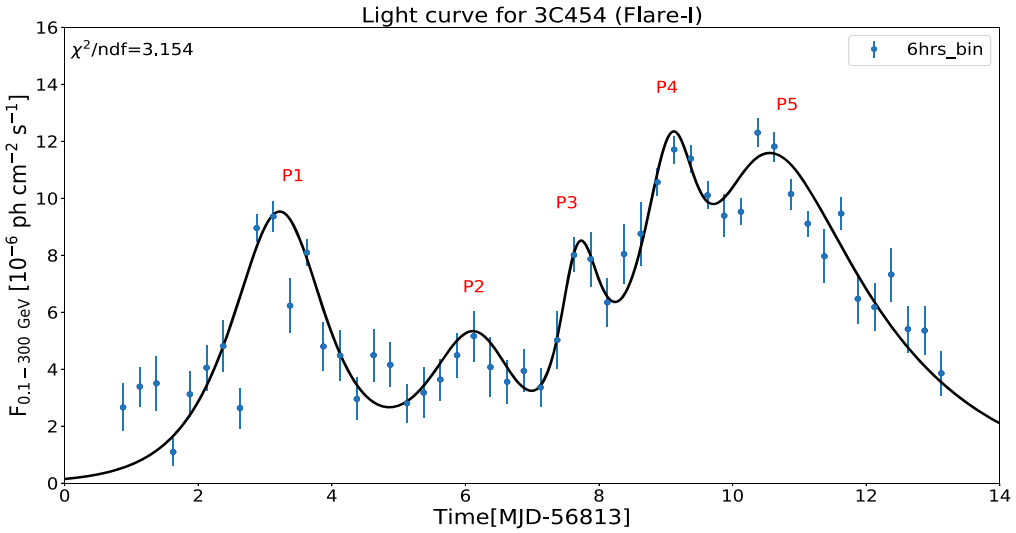

Figure 16. Fitted light curve (fitted by the sum of the exponential function) of Flare-3A for the Flare-I (MJD 56813−56826) epoch.

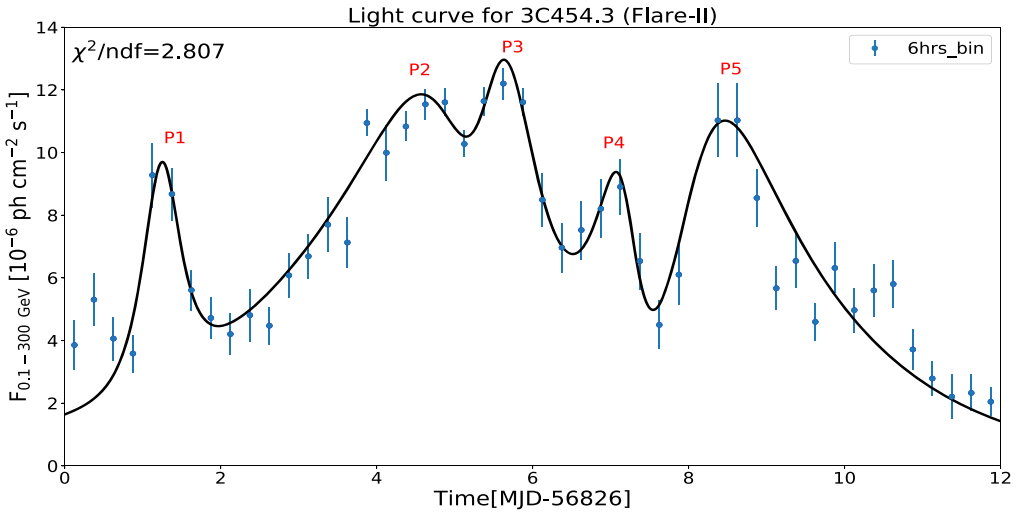

Figure 17. Fitted light curve (fitted by the sum of the exponential function) of Flare-3A for the Flare-II (MJD 56826−56838) epoch.

and 1.91 ± 0.10, respectively. Two distinct major peaks (P1 and P2) are observed during the flare phase (see Figure 23), which have peak fluxes of 11.43 ± 0.48 and 12.00 ± 0.49 at MJD 57254.1 and 57256.1, respectively.

Flare-4C (Figure 24) has much more error in flux compared to other substructures, and three different phases (pre-flare, flare, and post-flare) are observed. Pre-flare and post-flare states have a time span of 8 and 11 days before and after the flare phase, respectively. During the flare phase, four major peaks have been clearly identified with fluxes of 5.15 ± 0.83, 5.49 ± 0.80, 7.44 ± 0.94, and 5.44 ± 0.83 at MJD 57401.4, 57402.9, 57407.1, and 57408.9, respectively, which are shown in Figure 25.

Flare-4D (shown in Figure 26) has three phases similar to Flare-4A and Flare-4B. The pre-flare phase shows small variation in the flux, and the average flux is observed to be 1.31 ± 0.11, which lasts from MJD 57450 to 57456. The flare phase has two sharp peaks labeled as P1 and P2 with fluxes of 3.49 ± 0.69 and 9.99 ± 0.45 at MJD 57457.4 and 57460.1, respectively, which are shown in Figure 27. We have identified the post-flare region during MJD 57461−57468.

4.5. *Flare-5*

Similarly, a 6 hr binning of Flare-5 has also been carried out, and two substructures have been found: one during 2016 June–July (MJD 57542−57576) and another in 2016 December (MJD 57727−57752), with time spans of 34 and 25 days, respectively. Both the substructures (defined as Flare-5A and Flare-5B) have the simplest time profile, where the three phases pre-flare, flare, and post-flare can be clearly identified.

The pre-flare phase of Flare-5A has almost constant flux during MJD 57542−57549 (see Figure 28). Figure 29 shows the fitted light curve of the flare phase with a time duration (MJD 57549−57568) of 19 days, and five major peaks have been identified. A small fluctuation is noticed in flux during the post-flare phase (MJD 57568−57576), and the average flux is estimated to be 1.84 ± 0.09.

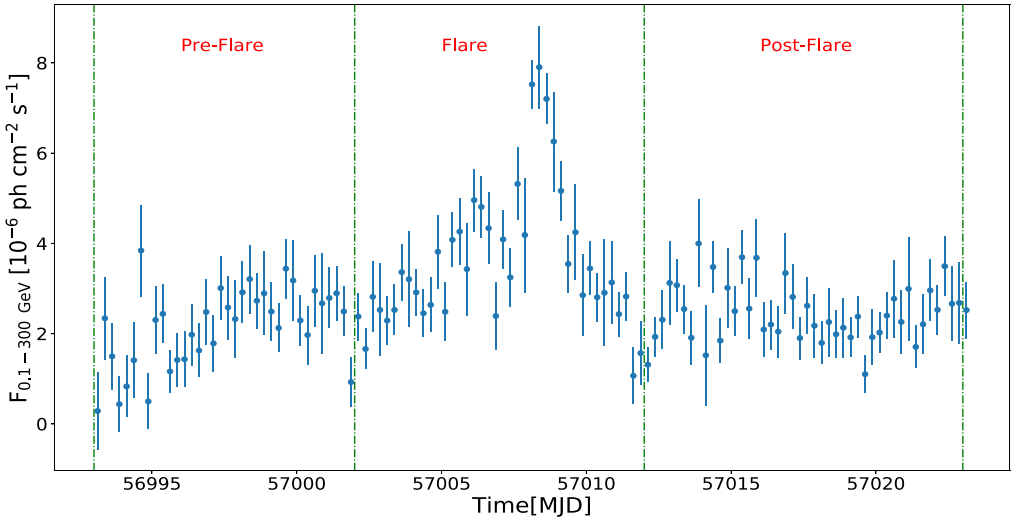

Figure 18. The 6 hr binning light curve for Flare-3B. Time durations of all the different periods of activities (shown by the dashed green lines) are MJD 56993−57002 (pre-flare), MJD 57002−57012 (flare), and MJD 57012−57023 (post-flare).

Table 6
Result of SED for Flare-1A Fitted with Different Models

Power Law						
Activity	F_0 (10^{-6} photons cm^{-2} s^{-1})	Γ			log(Likelihood)	
Flare	2.60 ± 0.03	2.39 ± 0.01	⋯	⋯	162999.70	⋯
Post-flare	1.30 ± 0.04	2.40 ± 0.03	⋯	⋯	57805.94	⋯
Log-parabola						
Activity	F_0 (10^{-6} photons cm^{-2} s^{-1})	α	β	⋯	log(Likelihood)	Δlog(Likelihood)
Flare	2.50 ± 0.04	2.31 ± 0.02	0.07 ± 0.01	⋯	162979.78	−19.92
Post-flare	1.30 ± 0.05	2.29 ± 0.05	0.09 ± 0.03	⋯	57799.58	−6.36
Broken Power Law						
Activity	F_0 (10^{-6} photons cm^{-2} s^{-1})	Γ_1	Γ_2	E_{break} (GeV)	log(Likelihood)	Δlog(Likelihood)
Flare	2.60 ± 0.04	2.29 ± 0.02	2.73 ± 0.06	1.02 ± 0.03	162960.52	−39.18
Post-flare	1.30 ± 0.06	2.27 ± 0.09	2.87 ± 0.20	1.03 ± 0.18	57797.77	−8.17

Note. Column (1): different periods of activity. Columns (2)−(4): flux value (F_0) and spectral indices for different models, respectively. Column (5): break energy (E_{break}) for broken-power-law model. Column (6): goodness of fit (log of likelihood). Column (7): difference in the goodness of fit with respect to the power-law model.

Figure 30 shows the three different states of Flare-5B. The pre-flare phase has been considered during MJD 57727 −57737. After that, a flare having two distinct major peaks has been identified, which is shown in Figure 31. Small variation in flux has been noticed in the flare phase during MJD 57737.1−57741.9, which is also fitted with the sum of the exponential function (Equation (2)). However, we have not considered any peak in this time interval owing to a low count of photons. The post-flare region has a time duration of around 6 days, with an average flux of 1.96 ± 0.14.

Constant flux values in the steady state (shown by the solid gray line) for Flare-4A, Flare-4B, Flare-4D, and Flare-5A have been shown in Table 2.

4.6. Variability

Variability time (t_{var}) is the timescale of variation in flux during flare. This can be computed by scanning the 6 hr binned γ-ray light curve with the following equation:

$$F(t_2) = F(t_1) 2^{\frac{(t_2-t_1)}{\tau_{d/h}}}, \quad (3)$$

where $F(t_1)$ and $F(t_2)$ are the fluxes at consecutive time instants t_1 and t_2, respectively. Doubling/halving (indicated by "+" and "−" sign, respectively) timescale is indicated by $\tau_{d/h}$. We have used the following two criteria while scanning the light curve (Prince et al. 2017):

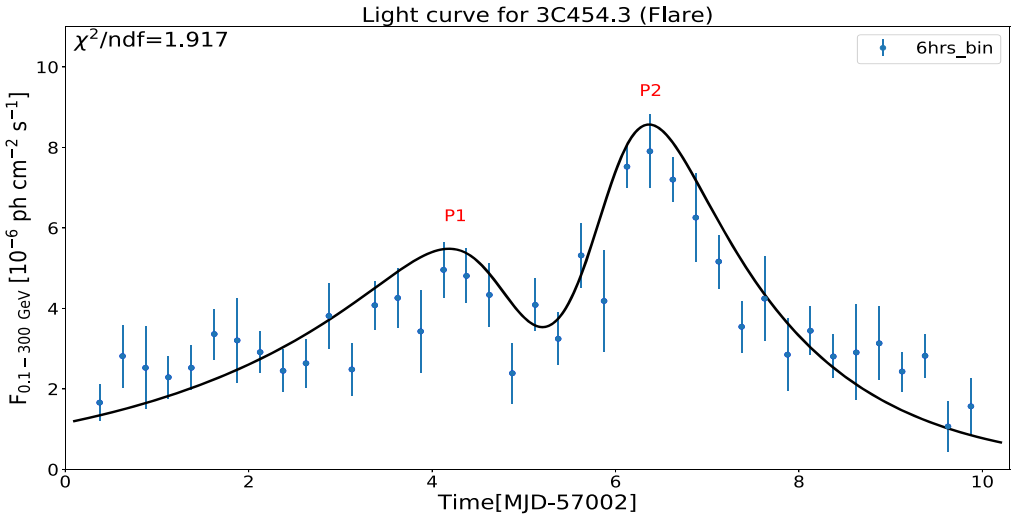

Figure 19. Fitted light curve (fitted by the sum of the exponential function) of Flare-3B for the flare (MJD 57002−57012) epoch.

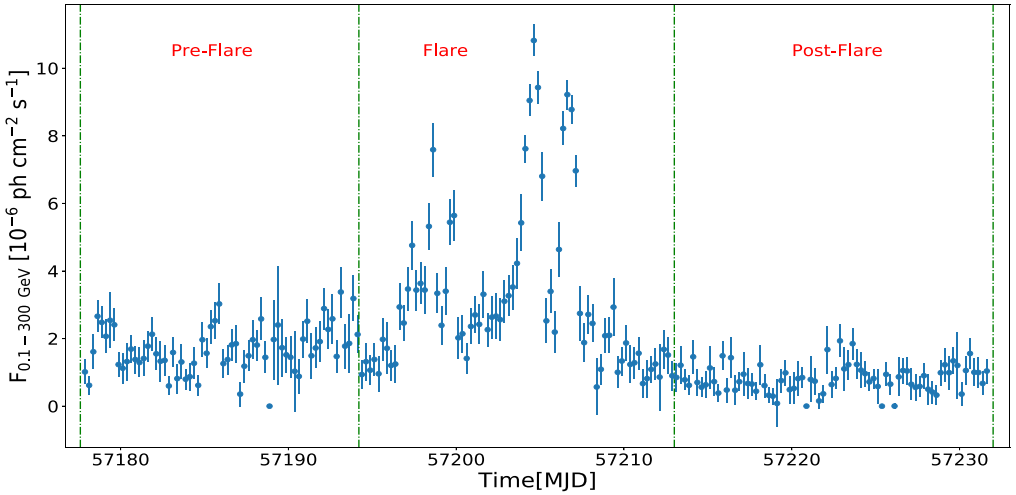

Figure 20. The 6 hr binning light curve for Flare-4A. Time durations of all the different periods of activities (shown by the dashed green lines) are MJD 57160−57190 (pre-flare), MJD 57194−57213 (flare), and MJD 57213−57232 (post-flare).

Table 7
All the Parameters Represented here Are Similar to the Parameters of Table 6

Power Law						
Activity	F_0 (10^{-6} photons cm^{-2} s^{-1})	Γ			log(Likelihood)	
Pre-flare	1.30 ± 0.05	2.42 ± 0.04	⋯	⋯	50345.11	⋯
Flare	2.90 ± 0.006	2.41 ± 0.001	⋯	⋯	231037.12	⋯
Log-parabola						
Activity	F_0 (10^{-6} photons cm^{-2} s^{-1})	α	β	⋯	log(Likelihood)	Δlog(Likelihood)
Pre-flare	1.20 ± 0.05	2.25 ± 0.05	0.18 ± 0.04	⋯	50368.45	23.34
Flare	2.70 ± 0.05	2.26 ± 0.02	0.12 ± 0.01	⋯	230979.32	−57.80
Broken Power Law						
Activity	F_0 (10^{-6} photons cm^{-2} s^{-1})	Γ_1	Γ_2	E_{break} (GeV)	log(Likelihood)	Δlog(Likelihood)
Pre-flare	1.20 ± 0.07	2.23 ± 0.09	3.11 ± 0.24	0.91 ± 0.16	50368.09	22.98
Flare	2.90 ± 0.04	2.31 ± 0.02	2.86 ± 0.05	1.03 ± 0.02	231038.29	1.17

Note. Results are shown for Flare-2A.

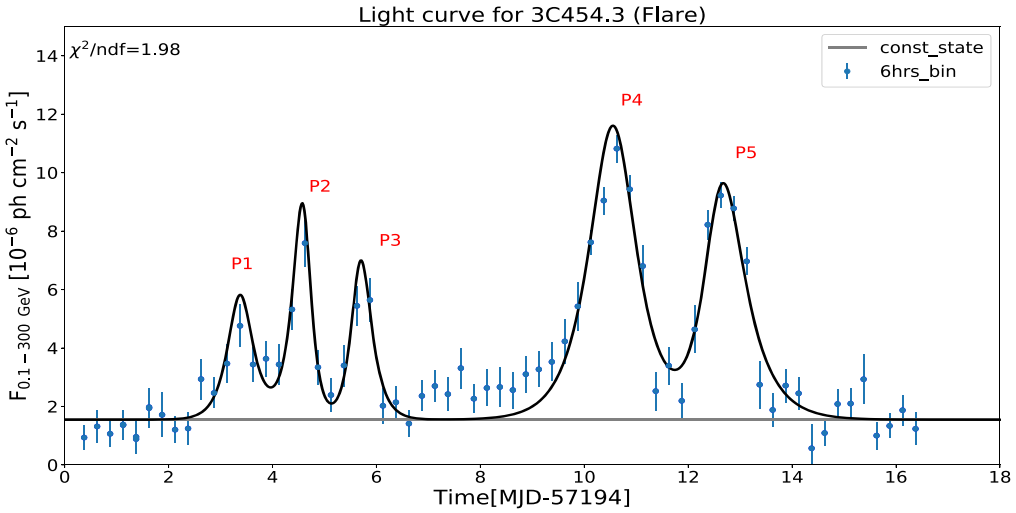

Figure 21. Fitted light curve (fitted by the sum of the exponential function) of Flare-4A for the flare (MJD 57194−57213) epoch.

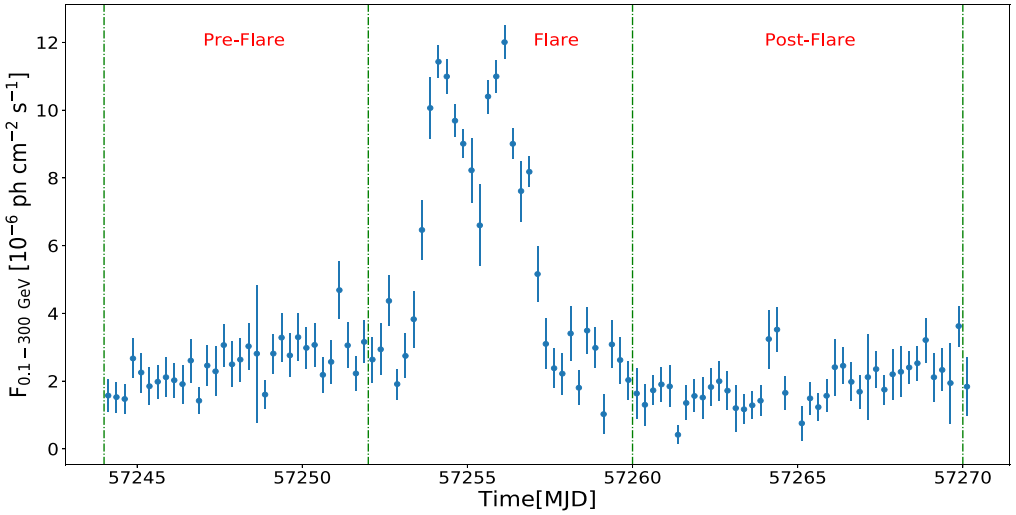

Figure 22. The 6 hr binning light curve for Flare-4B. Time durations of all the different periods of activities (shown by the dashed green lines) are MJD 57244−57252 (pre-flare), MJD 57251−57260 (flare), and MJD 57260−57270 (post-flare).

Table 8
All the Parameters Represented here Are Similar to the Parameters of Table 6

Power Law						
Activity	F_0 (10^{-6} photons cm^{-2} s^{-1})	Γ			log(Likelihood)	
Pre-flare	2.36 ± 0.067	2.42 ± 0.03	⋯	⋯	43514.22	⋯
Flare	7.4 ± 0.065	2.30 ± 0.008	⋯	⋯	238878.89	⋯
Log-parabola						
Activity	F_0 (10^{-6} photons cm^{-2} s^{-1})	α	β	⋯	log(Likelihood)	Δlog(Likelihood)
Pre-flare	2.20 ± 0.06	2.34 ± 0.04	0.08 ± 0.02	⋯	43507.63	−6.59
Flare	7.00 ± 0.08	2.16 ± 0.01	0.10 ± 0.007	⋯	238755.82	−123.07
Broken Power Law						
Activity	F_0 (10^{-6} photons cm^{-2} s^{-1})	Γ_1	Γ_2	E_{break} (GeV)	log(Likelihood)	Δlog(Likelihood)
Pre-flare	2.10 ± 0.09	2.23 ± 0.04	2.87 ± 0.11	0.91 ± 0.04	43493.02	−21.2
Flare	7.10 ± 0.07	2.16 ± 0.01	2.70 ± 0.03	1.00 ± 0.02	238745.81	−133.08

Note. Results are shown for Flare-2B.

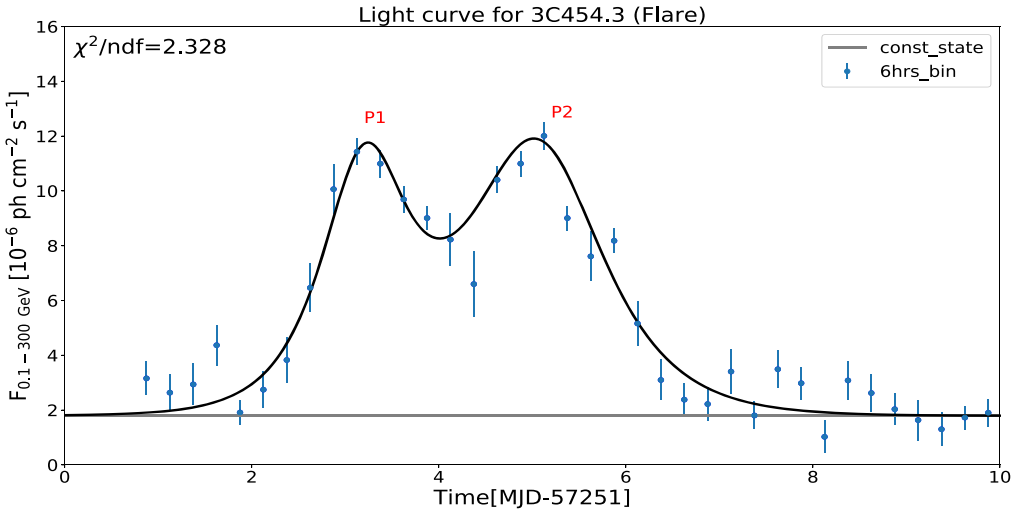

Figure 23. Fitted light curve (fitted by the sum of the exponential function) of Flare-4B for the flare (MJD 57251−57260) epoch.

Table 9
All the Parameters Represented here Are Similar to the Parameters of Table 6

Power Law						
Activity	F_0 (10^{-6} photons cm^{-2} s^{-1})	Γ			log(Likelihood)	
Pre-flare	2.70 ± 0.05	2.47 ± 0.02	⋯	⋯	79966.93	⋯
Flare-I	8.61 ± 1.8e−4	2.37 ± 1.38e−5	⋯	⋯	198341.69	⋯
Flare-II	5.66 ± 0.09	2.35 ± 0.01	⋯	⋯	74663.22	⋯
Post-flare	2.70 ± 0.06	2.40 ± 0.02	⋯	⋯	69581.59	⋯
Log-parabola						
Activity	F_0 (10^{-6} photons cm^{-2} s^{-1})	α	β	⋯	log(Likelihood)	Δlog(Likelihood)
Pre-flare	2.6 ± 0.05	2.36 ± 0.02	1.12 ± 0.02	⋯	79949.72	−17.21
Flare-I	7.94 ± 0.01	2.22 ± 0.001	0.102 ± 0.0009	⋯	198270.76	−70.93
Flare-II	5.35 ± 0.004	2.24 ± 0.0008	0.07 ± 0.0004	⋯	74650.18	−13.04
Post-flare	2.5 ± 0.08	2.23 ± 0.04	0.12 ± 0.02	⋯	69564.56	−17.03
Broken Power Law						
Activity	F_0 (10^{-6} photons cm^{-2} s^{-1})	Γ_1	Γ_2	E_{break} (GeV)	log(Likelihood)	Δlog(Likelihood)
Pre-flare	2.6 ± 0.05	2.33 ± 0.03	2.95 ± 0.12	0.89 ± 0.16	79952.88	−14.05
Flare-I	8.20 ± 0.008	2.24 ± 0.0004	2.71 ± 0.002	0.99 ± 0.0002	198278.75	−62.94
Flare-II	5.43 ± 0.002	2.24 ± 0.0001	2.63 ± 0.008	1.02 ± 0.0001	74651.10	−12.12
Post-flare	2.60 ± 0.06	2.27 ± 0.03	2.92 ± 0.13	1.10 ± 0.20	69563.80	−17.79

Note. Results are shown for Flare-2C.

1. Flux should be half or double between two successive instants of time.
2. The condition TS > 25 (corresponds to ∼5σ detection) on flux must always be fulfilled for these two consecutive time instants.

The value of $\tau_{d/h}$ for each substructure has been shown in Tables 3–5. The minimum value of $|\tau_{d/h}|$ is defined as the variability time (t_{var}) in our work.

In our 9 yr light-curve study we have found the shortest time as $\tau_{d/h}$ (or t_{var}) = 1.70 ± 0.38 hr during MJD 56815.625 −56815.875 (Flare-3A), which is consistent with previously calculated hour-scale variability time for other FSRQs, e.g., PKS 1510−089 and CTA 102 (Prince et al. 2017, 2018).

5. Gamma-Ray Spectral Energy Distribution of Flaring States

We have fitted the SEDs of different epochs with three different spectral models (Abdo et al. 2010b). These are

(i) A power-law model (PL), whose functional form is

$$\frac{dN}{dE} = N_0\left(\frac{E}{E_0}\right)^{-\Gamma}, \quad (4)$$

where N_0 and Γ are the prefactor and spectral index, respectively. We have kept fixed the value of E_0 (scaling factor) to 100 MeV for all the SEDs.

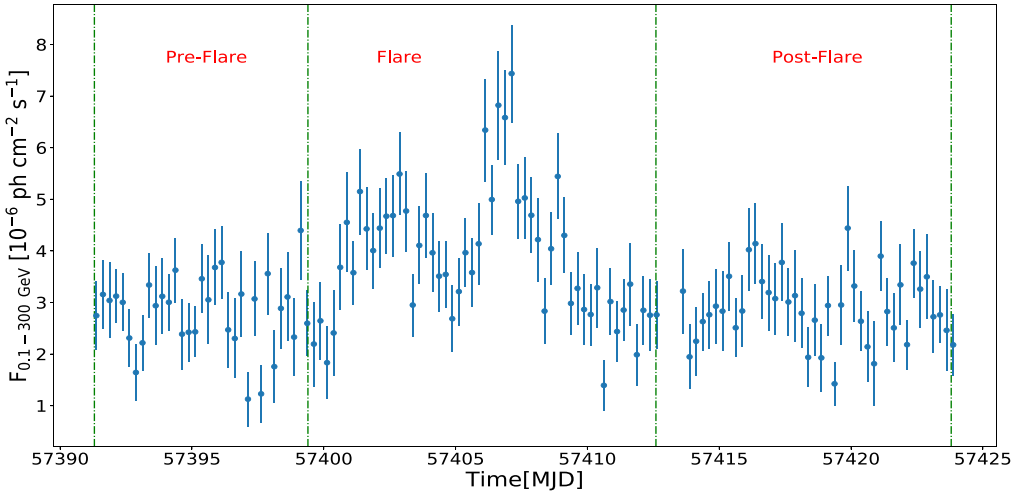

Figure 24. The 6 hr binning light curve for Flare-4C. Time durations of all the different periods of activities (shown by the dashed green lines) are MJD 57391−57399 (pre-flare), MJD 57399−57413 (flare), and MJD 57413−57424 (post-flare).

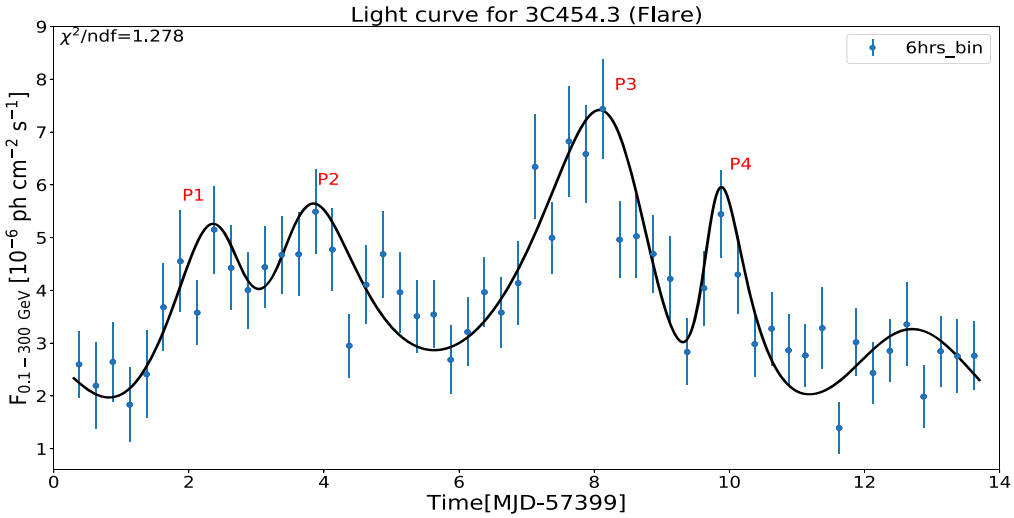

Figure 25. Fitted light curve (fitted by the sum of the exponential function) of Flare-4C for the flare (MJD 57399−57413) epoch.

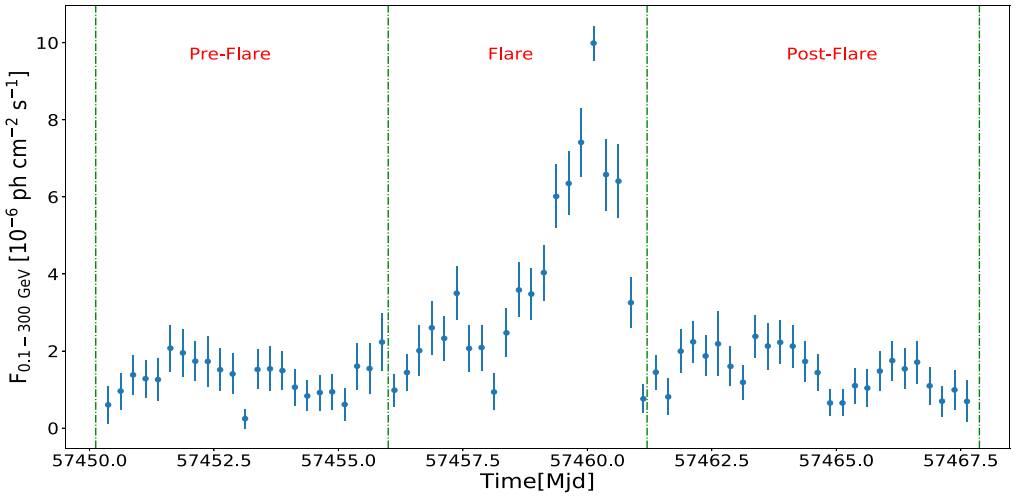

Figure 26. The 6 hr binning light curve for Flare-4D. Time durations of all the different periods of activities (shown by the dashed green lines) are MJD 57450−57456 (pre-flare), MJD 57454−57461 (flare), and MJD 57461−57468 (post-flare).

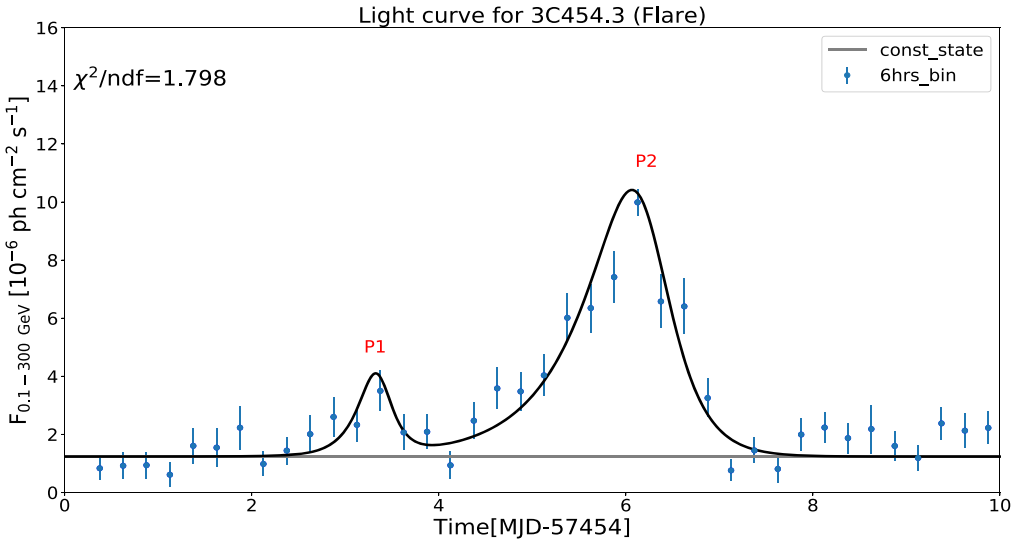

Figure 27. Fitted light curve (fitted by the sum of the exponential function) of Flare-4D for the flare (MJD 57454−57461) epoch.

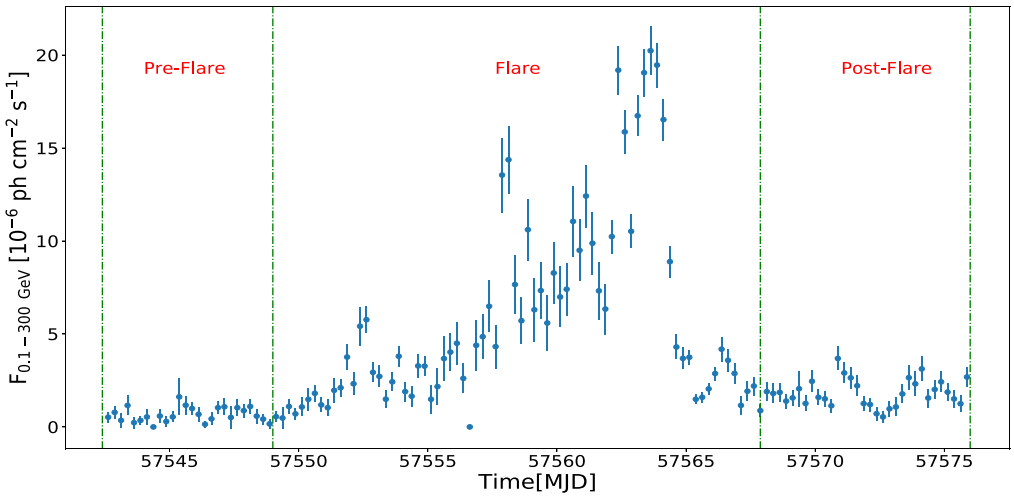

Figure 28. The 6 hr binning light curve for Flare−5A. Time durations of all the different periods of activities (shown by the dashed green lines) are MJD 57542 −57549 (pre-flare), MJD 57549−57568 (flare), and MJD 57568−57576 (post-flare).

(ii) A log-parabola model(LP), whose functional form is

$$\frac{dN}{dE} = N_0\left(\frac{E}{E_0}\right)^{-(\alpha+\beta\log(E/E_0))}, \quad (5)$$

where α and β are the photon index and curvature index, respectively. Scaling factor (E_0) is kept fixed to 300 MeV, near the low-energy part of the spectrum ("ln" is the natural logarithm).

(iii) A broken-power-law model (BPL), whose functional form is

$$\frac{dN}{dE} = N_0\begin{cases}\left(\frac{E}{E_b}\right)^{-\Gamma_1}, & \text{for } E < E_b\\ \left(\frac{E}{E_b}\right)^{-\Gamma_2}, & \text{otherwise}\end{cases}, \quad (6)$$

where E_b is the break energy.

The values of the fitted parameters for these spectral models (PL, LP, and BPL) have been elucidated in Tables 6–18. We have also mentioned the log(Likelihood) value for all the epochs and calculated the Δlog(Likelihood) value from that, which is defined by the difference between the log(Likelihood) value for the log-parabola/broken-power-law model and the simple power-law model.

Figure 32 shows the SEDs of the substructure of Flare-1A for two different phases: flare and post-flare. Here cyan, black, and magenta colors indicate the fitting of spectral points with the PL, LP, and BPL, respectively. The values of the fitted parameters for the different periods of activity for these models (PL, LP, BPL) have been given in Table 6.

The SEDs of the flaring epochs for all four substructures (Flare-2A, Flare-2B, Flare-2C, and Flare-2D) of Flare-2 have been illustrated in Figures 33–36, respectively. All of these substructures except Flare-2A show a spectral hardening with increasing flux. Spectral index (Γ) is nearly constant (for PL

Table 10
All the Parameters Represented here Are Similar to the Parameters of Table 6

Power Law						
Activity	F_0 (10^{-6} photons cm^{-2} s^{-1})	Γ			log(Likelihood)	
Pre-flare	2.98 ± 0.04	2.41 ± 0.01	⋯	⋯	85950.62	⋯
Platue-I	6.40 ± 0.07	2.33 ± 0.01	⋯	⋯	145909.56	⋯
Flare-I	24.0 ± 0.16	2.27 ± 0.006	⋯	⋯	250597.83	⋯
Flare-II	13.0 ± 0.09	2.29 ± 0.007	⋯	⋯	241670.99	⋯
Platue-II	5.90 ± 0.09	2.31 ± 0.01	⋯	⋯	70434.36	⋯
Post-flare	2.52 ± 0.0003	2.39 ± 0.00008	⋯	⋯	195003.71	⋯
Log-parabola						
Activity	F_0 (10^{-6} photons cm^{-2} s^{-1})	α	β	⋯	log(Likelihood)	Δlog(Likelihood)
Pre-flare	2.78 ± 0.07	2.25 ± 0.02	0.13 ± 0.01	⋯	85899.15	−51.47
Platue-I	6.20 ± 0.07	2.22 ± 0.01	0.08 ± 0.009	⋯	145858.64	−50.92
Flare-I	22.0 ± 0.24	2.12 ± 0.01	0.105 ± 0.006	⋯	250390.52	−207.31
Flare-II	13.0 ± 0.10	2.19 ± 0.01	0.08 ± 0.006	⋯	241554.87	−116.12
Platue-II	5.70 ± 0.10	2.23 ± 0.02	0.06 ± 0.01	⋯	70420.27	−14.09
Post-flare	2.36 ± 0.05	2.24 ± 0.02	0.11 ± 0.01	⋯	194890.83	−112.88
Broken Power Law						
Activity	F_0 (10^{-6} photons cm^{-2} s^{-1})	Γ_1	Γ_2	$E_{\rm break}$ (GeV)	log(Likelihood)	Δlog(Likelihood)
Pre-flare	2.84 ± 0.03	2.25 ± 0.005	2.95 ± 0.03	0.97 ± 0.003	85899.23	−51.39
Platue-I	6.30 ± 0.07	2.21 ± 0.01	2.69 ± 0.05	0.98 ± 0.11	145859.93	−49.63
Flare-I	23.0 ± 0.20	2.15 ± 0.01	2.62 ± 0.02	0.99 ± 0.02	250424.69	−173.14
Flare-II	13.0 ± 0.10	2.18 ± 0.007	2.62 ± 0.02	0.99 ± 0.006	241557.40	−113.59
Platue-II	5.80 ± 0.10	2.23 ± 0.02	2.55 ± 0.07	−1.01 ± 0.27	70422.59	−11.77
Post-flare	2.41 ± 0.003	2.25 ± 0.0006	2.89 ± 0.003	1.01 ± 0.0003	194888.67	−115.04

Note. Results are shown for Flare-2D.

Table 11
All the Parameters Represented here Are Similar to the Parameters of Table 6

Power Law						
Activity	F_0 (10^{-6} photons cm^{-2} s^{-1})	Γ			log(Likelihood)	
Pre-flare	2.25 ± 0.02	2.27 ± 0.005	⋯	⋯	36569.38	⋯
Flare-I	6.80 ± 0.13	2.12 ± 0.01	⋯	⋯	54645.77	⋯
Flare-II	7.20 ± 0.12	1.99 ± 0.01	⋯	⋯	63621.22	⋯
Post-flare	3.65 ± 0.004	2.21 ± 0.0006	⋯	⋯	36381.77	⋯
Log-parabola						
Activity	F_0 (10^{-6} photons cm^{-2} s^{-1})	α	β	⋯	log(Likelihood)	Δlog(Likelihood)
Pre-flare	2.06 ± 0.02	2.10 ± 0.01	0.09 ± 0.006	⋯	36565.30	−4.08
Flare-I	6.10 ± 0.02	1.92 ± 0.003	0.09 ± 0.001	⋯	54599.47	−55.30
Flare-II	6.80 ± 0.12	1.81 ± 0.02	0.08 ± 0.009	⋯	63569.28	−51.94
Post-flare	3.44 ± 0.001	2.04 ± 0.0003	0.10 ± 0.0001	⋯	36367.85	−13.92
Broken Power Law						
Activity	F_0 (10^{-6} photons cm^{-2} s^{-1})	Γ_1	Γ_2	$E_{\rm break}$ (GeV)	log(Likelihood)	Δlog(Likelihood)
Pre-flare	2.10 ± 0.03	2.11 ± 0.008	2.58 ± 0.03	0.98 ± 0.005	36565.02	−4.36
Flare-I	6.50 ± 0.13	1.99 ± 0.02	2.42 ± 0.04	1.08 ± 0.03	54619.72	−26.05
Flare-II	6.90 ± 0.13	1.82 ± 0.02	2.25 ± 0.04	1.02 ± 0.10	63578.84	−42.38
Post-flare	3.49 ± 0.01	2.05 ± 0.002	2.58 ± 0.009	1.02 ± 0.001	36367.92	−13.85

Note. Results are shown for Flare-3A.

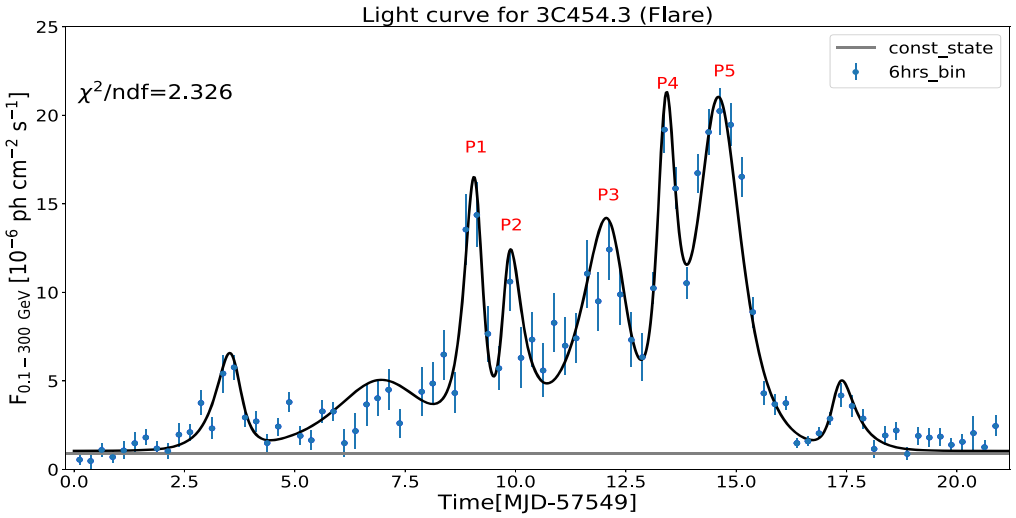

Figure 29. Fitted light curve (fitted by the sum of the exponential function) of Flare-5A for the flare (MJD 57549−57568) epoch.

Table 12
All the Parameters Represented here Are Similar to the Parameters of Table 6

Power Law						
Activity	F_0 (10^{-6} photons cm^{-2} s^{-1})	Γ			log(Likelihood)	
Pre-flare	2.30 ± 0.0006	2.31 ± 0.0001	⋯	⋯	20940.21	⋯
Flare	3.81 ± 0.08	2.32 ± 0.01	⋯	⋯	34862.33	⋯
Post-flare	2.32 ± 0.01	2.33 ± 0.005	⋯	⋯	32768.08	⋯
Log-parabola						
Activity	F_0 (10^{-6} photons cm^{-2} s^{-1})	α	β	⋯	log(Likelihood)	Δlog(Likelihood)
Pre-flare	1.95 ± 0.004	1.99 ± 0.002	0.20 ± 0.001	⋯	20930.24	−9.97
Flare	3.67 ± 0.009	2.18 ± 0.002	0.11 ± 0.001	⋯	34849.17	−13.16
Post-flare	2.08 ± 0.02	2.15 ± 0.01	0.10 ± 0.007	⋯	32761.89	−6.19
Broken Power Law						
Activity	F_0 (10^{-6} photons cm^{-2} s^{-1})	Γ_1	Γ_2	E_{break} (GeV)	log(Likelihood)	Δlog(Likelihood)
Pre-flare	2.06 ± 0.02	2.06 ± 0.004	2.96 ± 0.02	0.98 ± 0.002	20931.05	−9.16
Flare	3.71 ± 0.01	2.18 ± 0.001	2.76 ± 0.006	0.99 ± 0.0007	34850.98	−11.35
Post-flare	2.13 ± 0.02	2.16 ± 0.004	2.70 ± 0.02	1.01 ± 0.002	32761.75	−6.33

Note. Results are shown for Flare-3B.

model) with changing flux in Flare-2A (shown in Table 7). The values of the fitted parameters for Flare-2B and Flare-2C have been displayed in Tables 8 and 9, respectively. For Flare-2D, in pre-flare phase index $\Gamma = 2.41 \pm 0.01$, and then it changes to 2.33 ± 0.01 for the Plateau-I phase and to 2.27 ± 0.00 and 2.29 ± 0.00 for the Flare-I and Flare-II phases, respectively, which have been described in Table 10.

A significant spectral hardening is observed during Flare-3A, when the source transits from the pre-flare to Flare-I and Flare-II phases, whereas during Flare-3B the spectral hardening is not very significant. The SEDs of these substructures have been shown in Figures 37 and 38, and the corresponding values of the parameters have been given in Tables 11 and 12, respectively.

Flare-4A shows the spectral softening when the source travels from the pre-flare to flare epoch and spectral index changes from $\Gamma = 2.27 \pm 0.01$ to 2.32 ± 0.00, which is described in Table 13. Two (Flare-4B and Flare-4D) out of four substructures show significant spectral hardening when the source transits from low flux state to high flux state. The SEDs of different epochs of Flare-4A, Flare-4B, Flare-4C, and Flare-4D have been illustrated in Figures 39–42, respectively. Tables 14–16 describe the modeling parameter values of SEDs of different periods for Flare-4B, Flare-4C, and Flare-4D, respectively.

A clear indication of spectral hardening is also seen in both substructures (Flare-5A and Flare-5B) of Flare-5. In Flare-5A, a significant change in Γ (2.60 ± 0.01 to 2.11 ± 0.00) has been

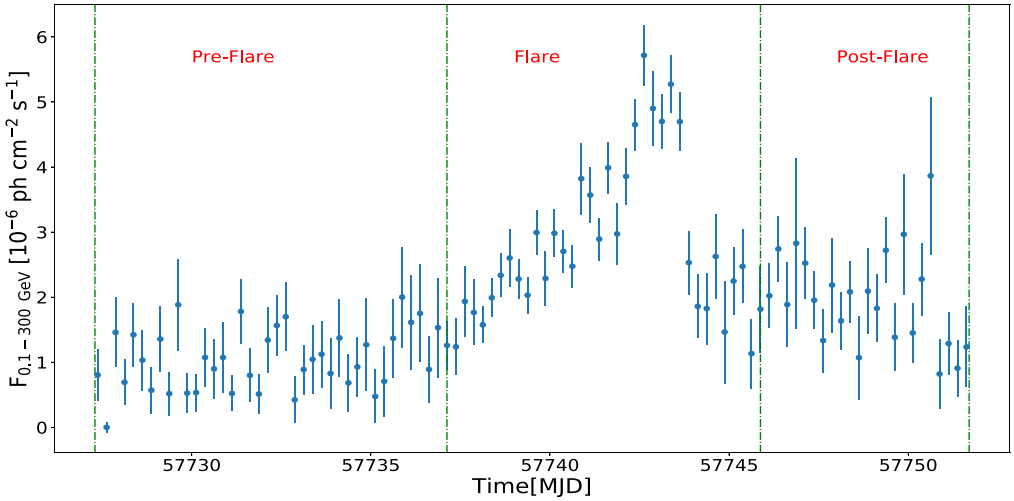

Figure 30. The 6 hr binning light curve for Flare-5B. Time durations of all the different periods of activities (shown by the dashed green lines) are MJD 57727−57737 (pre-flare), MJD 57737−57746 (flare), and MJD 57746−57752 (post-flare).

noticed during the pre-flare to flare epoch. The SEDs of different periods of activity of these substructures have been given in Figures 43 and 44, respectively. The values of the fitted parameters have been elucidated in Tables 17 and 18.

From the above γ-ray SED analysis of the 3C 454.3 source, we find that spectral hardening is an important feature of this source. This has been noticed before by Britto et al. (2016) during MJD 56570−56863. Only one substructure (Flare-4A) shows spectral softening during a change of state from pre-flare to flare. The values of the reduced χ^2 for the different spectral models (PL, LP, BPL) have been provided in Table 19, which shows that LP is the best-fitted model for most of the flaring states.

6. Multiwavelength Study of 3C 454.3

This section is dedicated to the multiwavelength study of blazar 3C 454.3. We have chosen the brightest flaring state (Flare-2) of 3C 454.3 from the whole 9 yr γ-ray light curve (shown in Figure 1). We have also collected the simultaneous multiwavelength data from other instruments and analyzed it. The simultaneous data from other wave bands are X-ray, ultraviolet (UV), and optical from Swift-XRT and UVOT telescopes. We have divided this Flare-2 state into four regions labeled as Flare-2A, Flare-2B, Flare-2C, and Flare-2D with time duration of MJD 55045−55140, MJD 55140−55201, MJD 55250−55356, and MJD 55467−55600, respectively, which are shown in Figure 45 based on gamma-ray flux as mentioned in Section 4.2. Flare-2A and Flare-2D have the simultaneous observation in gamma-ray, X-ray, optical, and UV wave bands, and hence for further study we have concentrated on Flare-2A and Flare-2D. The multiwavelength light curve of Flare-2 has been shown in Figure 45.

6.1. Multiwavelength Light Curve

Figure 46 shows the multiwavelength light curve of Flare-2A with a time span of 95 days (MJD 55045−55140). In the uppermost panel 6 hr binning of γ-ray data has been shown, and corresponding X-ray, optical, and UV data have been shown in the second, third, and fourth rows, respectively. In the γ-ray light-curve flux started rising slowly with small fluctuation. The maximum flux was recorded as 6.69 ± 0.79 at MJD 55091.375, and then the flux decayed slowly with small variation. The average flux of the decay period during MJD 55095.6−55140.125 is 2.94 ± 0.05. It is also observed that when the flux was still increasing in gamma-ray, the source started flaring in X-ray, optical, and UV bands. In the Swift-XRT data set the maximum peak was observed at MJD 55070.37 with flux of $(8.66 \pm 0.96) \times 10^{-11}$ erg cm^{-2} s^{-1}. During MJD 55094−55140, data are not available in XRT photon counting (PC) mode. Similarly, optical and UV data have also been plotted, and the brightest peak was found at MJD 55069.91 with fluxes of 3.47 ± 0.13, 3.07 ± 0.08, 2.71 ± 0.11, 2.03 ± 0.09, 2.04 ± 0.08, and 1.74 ± 0.06 in V, B, U, $W1$, $M2$, and $W2$ band, respectively, which are in units of 10^{-11} erg cm^{-2} s^{-1}. In V, U, $W1$, and $M2$ the second-brightest peak was observed at MJD 55091.18, which coincided with the first γ-ray brightest peak with a time lag of ∼5 hr, while in B band maximum peak was noticed at MJD 55090.92 with a time lag of ∼11 hr.

The multiwavelength light curve of Flare-2D has been shown in Figure 47, which has a time duration of 133 days (MJD 55467.125−55600.125). The highest flux was recorded at MJD 55519.875 with flux of 80.41 ± 5.93 in the 6 hr bin γ-ray wave band. After this, the flux started decreasing slowly with small variation during MJD 55536.6−55590.1, and the average flux was 9.80 ± 0.06. We are unable to observe any peak in XRT PC mode owing to the unavailability of the simultaneous data during MJD 55504−55554. All the peaks in optical and UV band nearly coincide with the peaks observed in γ-ray band. Interestingly, the peaks in optical and UV band during MJD 55510.1−55511.4 have no γ-ray counterpart, which has been reported earlier in several cases (Vercellone & Striani 2011; Rajput et al. 2019).

6.2. Multiwavelength SED Modeling

We have modeled the multiwavelength SEDs with the time-dependent "GAMERA" (Hahn 2015) code, which is publicly available on the github webpage.[4] This code solves the time-dependent continuity equation, calculates the evolved electron spectrum $N(E, t)$, and then computes the synchrotron and inverse Compton emission for that $N(E, t)$. The continuity

[4] https://github.com/libgamera/GAMERA

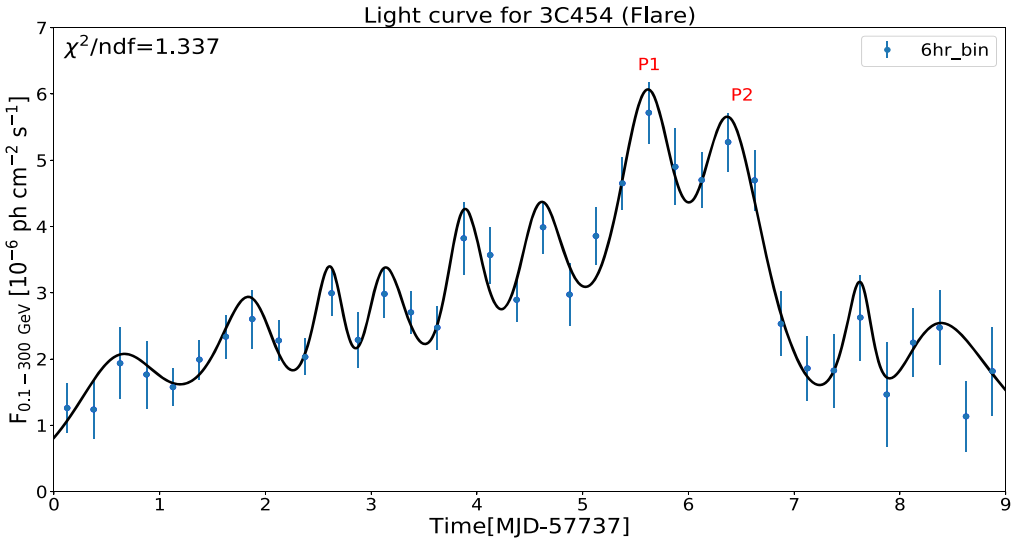

Figure 31. Fitted light curve (fitted by the sum of the exponential function) of Flare-5B for the flare (MJD 57737−57746) epoch.

Table 13
All the Parameters Represented here Are Similar to the Parameters of Table 6

Power Law						
Activity	F_0 (10^{-6} photons cm^{-2} s^{-1})	Γ			log(Likelihood)	
Pre-flare	1.38 ± 0.01	2.27 ± 0.006	⋯	⋯	75077.06	⋯
Flare	3.26 ± 0.004	2.32 ± 0.0009	⋯	⋯	81537.39	⋯
Post-flare	0.78 ± 0.01	2.41 ± 0.01	⋯	⋯	40656.04	⋯
Log-parabola						
Activity	F_0 (10^{-6} photons cm^{-2} s^{-1})	α	β	⋯	log(Likelihood)	Δlog(Likelihood)
Pre-flare	1.28 ± 0.005	2.08 ± 0.004	0.12 ± 0.002	⋯	75031.97	−45.09
Flare	3.08 ± 0.007	2.17 ± 0.002	0.10 ± 0.001	⋯	81476.70	−60.69
Post-flare	0.69 ± 0.005	2.13 ± 0.008	0.22 ± 0.005	⋯	40617.67	−38.37
Broken Power Law						
Activity	F_0 (10^{-6} photons cm^{-2} s^{-1})	Γ_1	Γ_2	E_{break} (GeV)	log(Likelihood)	Δlog(Likelihood)
Pre-flare	1.31 ± 0.04	2.10 ± 0.03	2.71 ± 0.08	1.01 ± 0.02	75033.75	−43.31
Flare	3.14 ± 0.02	2.18 ± 0.003	2.72 ± 0.01	0.99 ± 0.002	81479.48	−57.91
Post-flare	0.72 ± 0.006	2.15 ± 0.003	3.34 ± 0.02	0.99 ± 0.002	40616.82	−39.22

Note. Results are shown for Flare-4A.

equation is given by

$$\frac{\partial N(E,t)}{\partial t} = Q(E,t) - \frac{\partial}{\partial E}(b(E,t)N(E,t)) - \frac{N(E,t)}{\tau_{esc}(E,t)}, \quad (7)$$

where $Q(E, t)$ is the injected electron spectrum. The energy-loss rate is denoted by $b(E) = (\frac{dE}{dt})$, and $\tau_{esc}(E, t)$ represents the escape time. The log-parabolic model gives the best-fitted parameters for most of the substructures in the γ-ray SED, which have been described in Table 19. The radiative losses of the LP electron spectrum produce the LP photon spectrum. Massaro et al. (2004) gave a general formalism to show that if the efficiency of acceleration decreases with increasing energy, the resulting shock electron spectrum follows the LP distribution. Due to this reason, we have assumed the LP form of $Q(E, t)$. The functional form of $Q(E, t)$ is defined by

$$Q(E) = l_0\left(\frac{E}{E_{ref}}\right)^{-(\alpha+\beta\log(E/E_{ref}))}, \quad (8)$$

where l_0 is normalization constant and E_{ref} is the reference energy, which is set at 90.0 MeV. "GAMERA" uses the full Klein–Nishina cross section to compute the inverse Compton emission (Blumenthal & Gould 1970).

6.3. Physical Constraints

Here we discuss the constraints on the model parameters that we have used in our modeling:

Table 14
All the Parameters Represented here Are Similar to the Parameters of Table 6

Power Law						
Activity	F_0 (10^{-6} photons cm^{-2} s^{-1})	Γ			log(Likelihood)	
Pre-flare	2.13 ± 0.005	2.31 ± 0.001	⋯	⋯	39002.40	⋯
Flare	6.51 ± 0.01	2.15 ± 0.001	⋯	⋯	41130.59	⋯
Post-flare	1.87 ± 0.01	2.41 ± 0.004	⋯	⋯	25474.42	⋯
Log-parabola						
Activity	F_0 (10^{-6} photons cm^{-2} s^{-1})	α	β	⋯	log(Likelihood)	Δlog(Likelihood)
Pre-flare	1.95 ± 0.001	2.13 ± 0.0009	0.10 ± 0.0004	⋯	38982.23	−20.17
Flare	5.68 ± 0.01	1.87 ± 0.002	0.14 ± 0.001	⋯	41075.71	−54.88
Post-flare	1.70 ± 0.03	2.21 ± 0.02	0.14 ± 0.01	⋯	25452.96	−21.46
Broken Power Law						
Activity	F_0 (10^{-6} photons cm^{-2} s^{-1})	Γ_1	Γ_2	$E_{\rm break}$ (GeV)	log(Likelihood)	Δlog(Likelihood)
Pre-flare	2.01 ± 0.001	2.17 ± 0.0003	2.61 ± 0.001	0.99 ± 0.0002	38987.98	−14.42
Flare	5.96 ± 0.02	1.94 ± 0.001	2.58 ± 0.006	1.08 ± 0.001	41080.72	−49.87
Post-flare	1.73 ± 0.01	2.20 ± 0.003	3.10 ± 0.02	1.03 ± 0.002	25450.76	−23.66

Note. Results are shown for Flare-4B.

Table 15
All the Parameters Represented here Are Similar to the Parameters of Table 6

Power Law						
Activity	F_0 (10^{-6} photons cm^{-2} s^{-1})	Γ			log(Likelihood)	
Pre-flare	2.90 ± 0.12	2.33 ± 0.39	⋯	⋯	21642.13	⋯
Flare	3.90 ± 0.10	2.31 ± 0.02	⋯	⋯	54879.34	⋯
Post-flare	2.90 ± 0.10	2.38 ± 0.03	⋯	⋯	40934.47	⋯
Log-parabola						
Activity	F_0 (10^{-6} photons cm^{-2} s^{-1})	α	β	⋯	log(Likelihood)	Δlog(Likelihood)
Pre-flare	2.70 ± 0.12	2.17 ± 0.05	0.12 ± 0.03	⋯	21649.23	7.1
Flare	3.30 ± 0.11	2.02 ± 0.06	0.19 ± 0.03	⋯	54834.23	−45.11
Post-flare	2.80 ± 0.10	2.29 ± 0.05	0.07 ± 0.03	⋯	40930.23	−4.24
Broken Power Law						
Activity	F_0 (10^{-6} photons cm^{-2} s^{-1})	Γ_1	Γ_2	$E_{\rm break}$ (GeV)	log(Likelihood)	Δlog(Likelihood)
Pre-flare	2.80 ± 0.15	2.18 ± 0.08	3.04 ± 0.33	1.32 ± 0.28	21647.54	5.41
Flare	3.70 ± 0.12	2.10 ± 0.04	2.91 ± 0.12	0.92 ± 0.12	54846.84	−32.50
Post-flare	2.80 ± 0.13	2.27 ± 0.76	2.86 ± 0.23	1.22 ± 0.21	40927.71	−6.76

Note. Results are shown for Flare-4C.

(i) To calculate the EC emission by the relativistic electrons, the cosmic microwave background (CMB) and BLR photons are taken into account as target photons. The standard value of CMB photon density (0.25 eV cm^{-3}; Longair 1974) has been used. The energy density of BLR photons is computed (in the comoving frame) with the following equation:

$$U'_{\rm BLR} = \frac{\Gamma^2 \zeta_{\rm BLR} L_{\rm Disk}}{4\pi c R^2_{\rm BLR}}, \quad (9)$$

where Γ is the bulk Lorentz factor of the emitting blob, whose value is assumed to be 20 (Vercellone & Striani 2011). The BLR photon energy density is only a fraction of 10% ($\zeta_{\rm BLR} \sim 0.1$) of the accretion disk photon energy density. The value of the disk luminosity $L_{\rm Disk} = 6.75 \times 10^{46}$ erg s^{-1} is taken from Bonnoli et al. (2011). We have computed the radius of the BLR region by the scaling relation $R_{\rm BLR} = 10^{17} L^{1/2}_{d,45}$, where $L_{d,45}$ (Ghisellini & Tavecchio 2009) is the disk luminosity in units of 10^{45} erg s^{-1}.

Table 16
All the Parameters Represented here Are Similar to the Parameters of Table 6

Power Law						
Activity	F_0 (10^{-6} photons cm^{-2} s^{-1})	Γ			log(Likelihood)	
Pre-flare	1.20 ± 0.10	2.45 ± 0.07	⋯	⋯	17622.70	⋯
Flare	4.00 ± 0.16	2.19 ± 0.03	⋯	⋯	19422.69	⋯
Post-flare	1.40 ± 0.09	2.27 ± 0.05	⋯	⋯	23233.62	⋯
Log-parabola						
Activity	F_0 (10^{-6} photons cm^{-2} s^{-1})	α	β	⋯	log(Likelihood)	Δlog(Likelihood)
Pre-flare	1.20 ± 0.10	2.26 ± 0.11	0.19 ± 0.08	⋯	17619.23	−3.47
Flare	3.80 ± 0.16	2.04 ± 0.05	0.09 ± 0.02	⋯	19415.80	−6.89
Post-flare	1.00 ± 0.12	1.73 ± 0.15	0.30 ± 0.07	⋯	23216.66	−16.96
Broken Power Law						
Activity	F_0 (10^{-6} photons cm^{-2} s^{-1})	Γ_1	Γ_2	$E_{\rm break}$ (GeV)	log(Likelihood)	Δlog(Likelihood)
Pre-flare	1.2 ± 0.02	2.29 ± 0.008	3.17 ± 0.06	1.003 ± 0.005	17611.85	−10.85
Flare	3.80 ± 0.19	2.04 ± 0.06	2.69 ± 0.19	1.30 ± 0.27	19413.59	−9.1
Post-flare	1.30 ± 0.15	2.00 ± 0.14	3.23 ± 0.54	1.11 ± 0.36	23222.49	−11.13

Note. Results are shown for Flare-4D.

Table 17
All the Parameters Represented here Are Similar to the Parameters of Table 6

Power Law						
Activity	F_0 (10^{-6} photons cm^{-2} s^{-1})	Γ			log(Likelihood)	
Pre-flare	0.69 ± 0.01	2.60 ± 0.01	⋯	⋯	25761.05	⋯
Flare	5.49 ± 0.006	2.11 ± 0.0005	⋯	⋯	80606.46	⋯
Post-flare	1.78 ± 0.004	2.28 ± 0.001	⋯	⋯	25145.68	⋯
Log-parabola						
Activity	F_0 (10^{-6} photons cm^{-2} s^{-1})	α	β	⋯	log(Likelihood)	Δlog(Likelihood)
Pre-flare	0.64 ± 0.0009	2.49 ± 0.001	0.07 ± 0.0009	⋯	25744.39	−16.66
Flare	5.02 ± 0.008	1.87 ± 0.001	0.134 ± 0.0008	⋯	80508.03	−98.43
Post-flare	1.55 ± 0.001	2.00 ± 0.001	0.165 ± 0.0006	⋯	25138.02	−7.66
Broken Power Law						
Activity	F_0 (10^{-6} photons cm^{-2} s^{-1})	Γ_1	Γ_2	$E_{\rm break}$ (GeV)	log(Likelihood)	Δlog(Likelihood)
Pre-flare	0.65 ± 0.01	2.47 ± 0.005	3.45 ± 0.09	1.50 ± 0.006	25741.78	−19.27
Flare	5.14 ± 0.02	1.904 ± 0.002	2.518 ± 0.008	1.014 ± 0.001	80518.44	−88.02
Post-flare	1.53 ± 0.008	1.95 ± 0.002	2.79 ± 0.008	0.828 ± 0.001	25136.59	−9.09

Note. Results are shown for Flare-5A.

(ii) We have also included emission from the accretion disk component in the code to compute the EC emission. We constrain the disk energy density in the comoving jet frame by the following equation (Dermer & Menon 2009):

$$U'_{\rm Disk} = \frac{0.207 R_g L_{\rm Disk}}{\pi c Z^3 \Gamma^2}. \quad (10)$$

We chose the mass of the central engine or black hole ($M_{\rm BH}$) as $5 \times 10^8\ M_\odot$ (Bonnoli et al. 2011) in order to estimate the gravitational radius $R_g = 1.48 \times 10^{14}$ cm. The distance of the emission region from the black hole is represented by "Z." The upper limit of this quantity is estimated by the given equation (Paliya 2015)

$$Z \leqslant \frac{2\Gamma^2 c t_{\rm var}}{1+z}, \quad (11)$$

where z is the redshift of the source. The variability time estimated during Flare-2 is found to be $t_{\rm var} = 1.93$ hr during MJD 55068.125−55068.375 (corresponds to

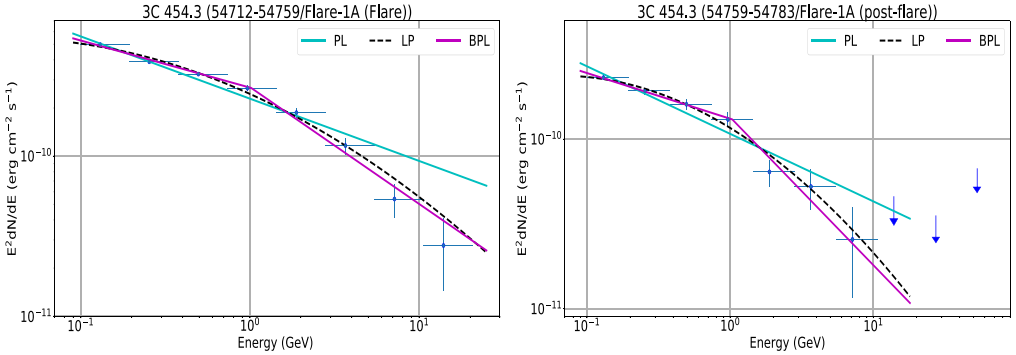

Figure 32. SED of different periods of Flare-1A as given in Figure 2. PL, LP, and BPL describe the power-law, log-parabola, and broken-power-law model, respectively, which are fitted to data points.

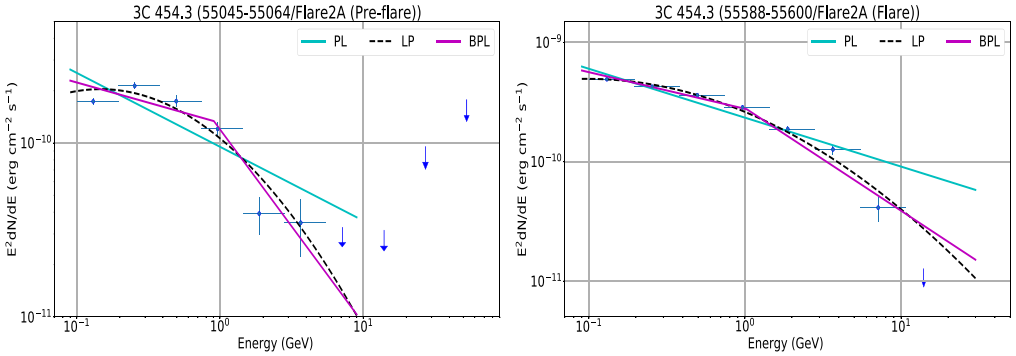

Figure 33. SED of different periods of Flare-2A as given in Figure 4. PL, LP, and BPL describe the power-law, log-parabola, and broken-power-law model, respectively, which are fitted to data points.

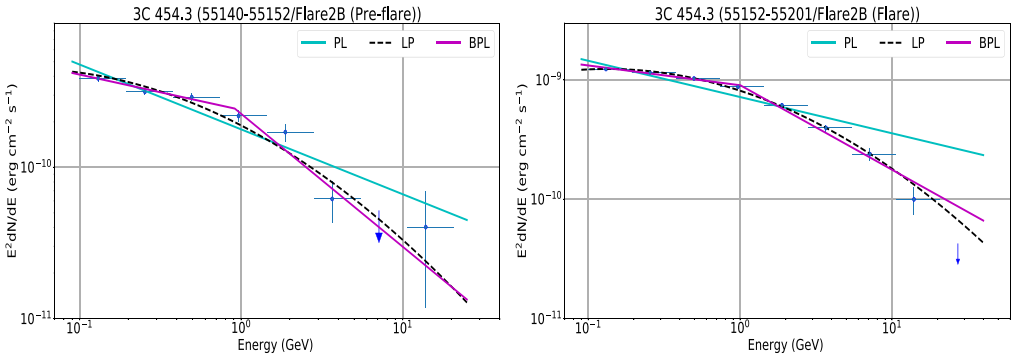

Figure 34. SED of different periods of Flare-2B as given in Figure 6. PL, LP, and BPL describe the power-law, log-parabola, and broken-power-law model, respectively, which are fitted to data points.

Flare-2A), which has been used to estimate "Z." The value of "Z" is estimated as $Z \sim 1.0 \times 10^{17}$ cm.

(iii) We can estimate the upper limit on the size of the emission region R with the following relation:

$$R \leqslant \frac{ct_{\rm var}\delta}{1+z}. \quad (12)$$

We have used $t_{\rm var} = 1.93$ hr and Doppler factor $\delta = 27.5$ (comparable to Bonnoli et al. 2011) for Flare-2, which give the value of $R = 3.08 \times 10^{15}$ cm. But it is noted that Equation (12) is just an approximation, and there are several effects that may introduce large error in determining R (Protheroe 2002). Moreover, the value of R calculated in this way for γ-ray wavelength does not give a good fit to the data in our SED modeling. In our work we have chosen $R = 3.0 \times 10^{16}$ cm, which is comparable to the value 5×10^{16} cm given by Gupta et al. (2017).

(iv) We have used typical values of BLR temperature ($T'_{\rm BLR}$) and disk temperature ($T'_{\rm Disk}$) in our model, which are 2.0×10^4 K and 1.0×10^6 K, respectively.

6.4. Modeling the SEDs

After constraining the above model parameters, we have simulated the multiwavelength SED using the code "GAMERA." We have included the escape term $\left(-\frac{N(E,t)}{\tau_{\rm esc}(E,t)}\right)$ for electrons in the continuity Equation (7) and considered two different cases:

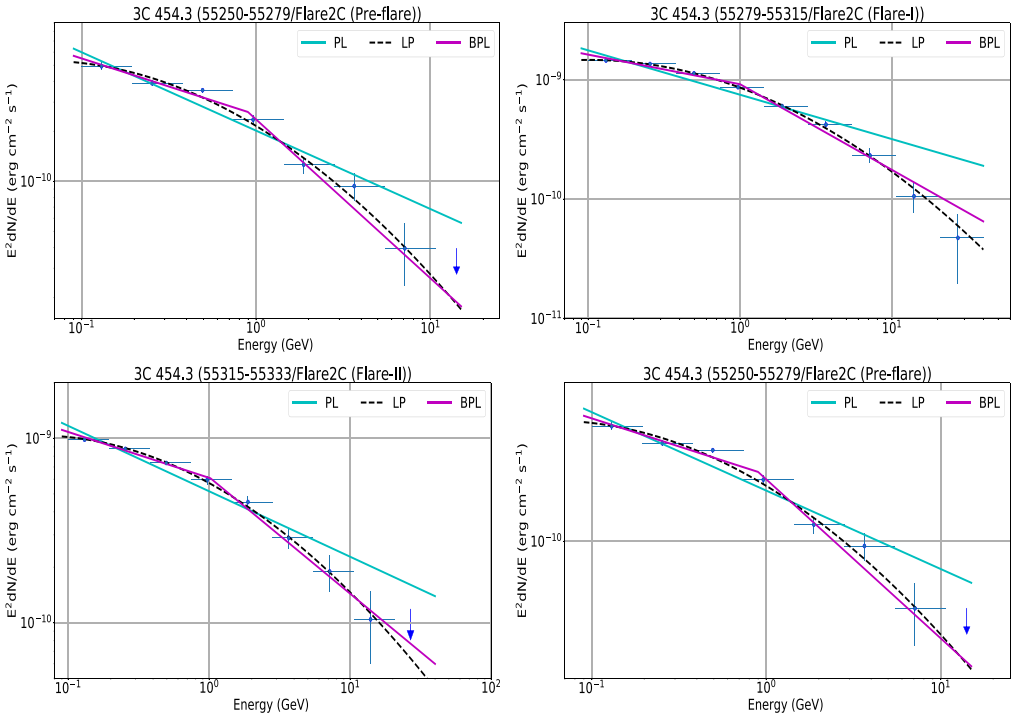

Figure 35. SED of different periods of Flare-2C as given in Figure 9. PL, LP, and BPL describe the power-law, log-parabola, and broken-power-law model, respectively, which are fitted to data points.

1. Case 1: In this case we have studied the model with constant escape time, which is $\tau_{\rm esc} \sim R/c$, where R is the size of the emission region.
2. Case 2: Next, we consider the energy-dependent escape time, which is given by $\tau_{\rm esc} = \eta E^{-0.5}$ (Sinha & Sahayanathan 2017). We have chosen the values $\eta \sim 387.0$ and 155.0 s MeV$^{1/2}$ for Flare-2A and Flare-2D, respectively, so that at low energy the escape time is comparable to the cooling time of electrons.

SED modeling has been done for the above two cases for both the flares (Flare-2A and Flare-2D), which are illustrated in Figures 48 and 49. We have shown the nonsimultaneous archival data for both the flares in cyan color represented by plus signs, which are taken from Abdo et al. (2010c). There are no simultaneous archival data available for Flare-2A. However, quasi-simultaneous data from MJD 55515 to 55524 (Vercellone & Striani 2011) and for MJD 55519 (Jorstad et al. 2013) are available for Flare-2D, and they are shown with a black triangle and green star in Figures 48 and 49. In our work the SED is averaged over the whole flaring period, i.e., 133 days from MJD 55467 to 55600. However, the SED data points shown in black and green are for the peak of the flare, which lasted for a very short period compared to our period (133 days), and hence our SED data points differ from them.

In our study we have adjusted the values of the following parameters to obtain the best-fitted model: magnetic field in the emission region (B), minimum and maximum Lorentz factor of the injected relativistic electrons ($\gamma_{\rm min}$ and $\gamma_{\rm max}$), and their spectral index (α) and curvature index (β). We have obtained the values of $B = 3.80$ and 2.30 G for Flare-2A and Flare-2D, respectively, by fitting the synchrotron emission of the relativistic electrons to the optical data. The value of spectral index (α) is 2.00 and 2.18 for Flare-2A and Flare-2D, respectively. For Flare-2A the value of minimum Lorentz factor ($\gamma_{\rm min}$) is 55 and 45 in Case 1 and Case 2, respectively. For Flare-2A and Flare-2D there is no significant difference in the values of the maximum Lorentz factor of the injected electrons ($\gamma_{\rm max}$); however, curvature index (β) varies significantly for Flare-2D ($\beta = 0.09$ for Case 1 and $\beta = 0.14$ for Case 2), whereas it remains similar for Flare-2A. The detailed results of the multiwavelength SED modeling have been described in Table 20.

We have also calculated the total required jet power by using the following equation:

$$P_{\rm tot} = \pi R^2 \Gamma^2 c (U'_e + U'_B + U'_p), \tag{13}$$

where U'_e, U'_B, and U'_p are the energy density of electrons (and positrons), magnetic field, and cold protons, respectively, in the comoving jet frame. The power carried by the injected electrons in the jet is given by

$$P_e = \frac{3\Gamma^2 c}{4R} \int_{E_{\rm min}}^{E_{\rm max}} EQ(E) dE, \tag{14}$$

where $Q(E)$ is the injected electron spectrum as defined in Equation (8). To compute U'_p, we have assumed that the ratio of electron–positron pair to proton number in the emission region is 10:1. From Equation (13) we have calculated the maximum required jet power ($P_{\rm tot}$) in our model, which is found to be 3.04×10^{46} erg s^{-1}. This value is lower than the estimated range of Eddington luminosity ($L_{\rm Edd}$): (0.6–5) $\times 10^{47}$ erg s^{-1} (Gu et al. 2001; Bonnoli et al. 2011; Khangulyan et al. 2013).

7. Modeling the Light Curve

Our SEDs represent the time-averaged flux over a very long time period. This is why the average values of the model parameters (Doppler factor, magnetic field, luminosity in injected electrons, blob size, viewing angle) are used in

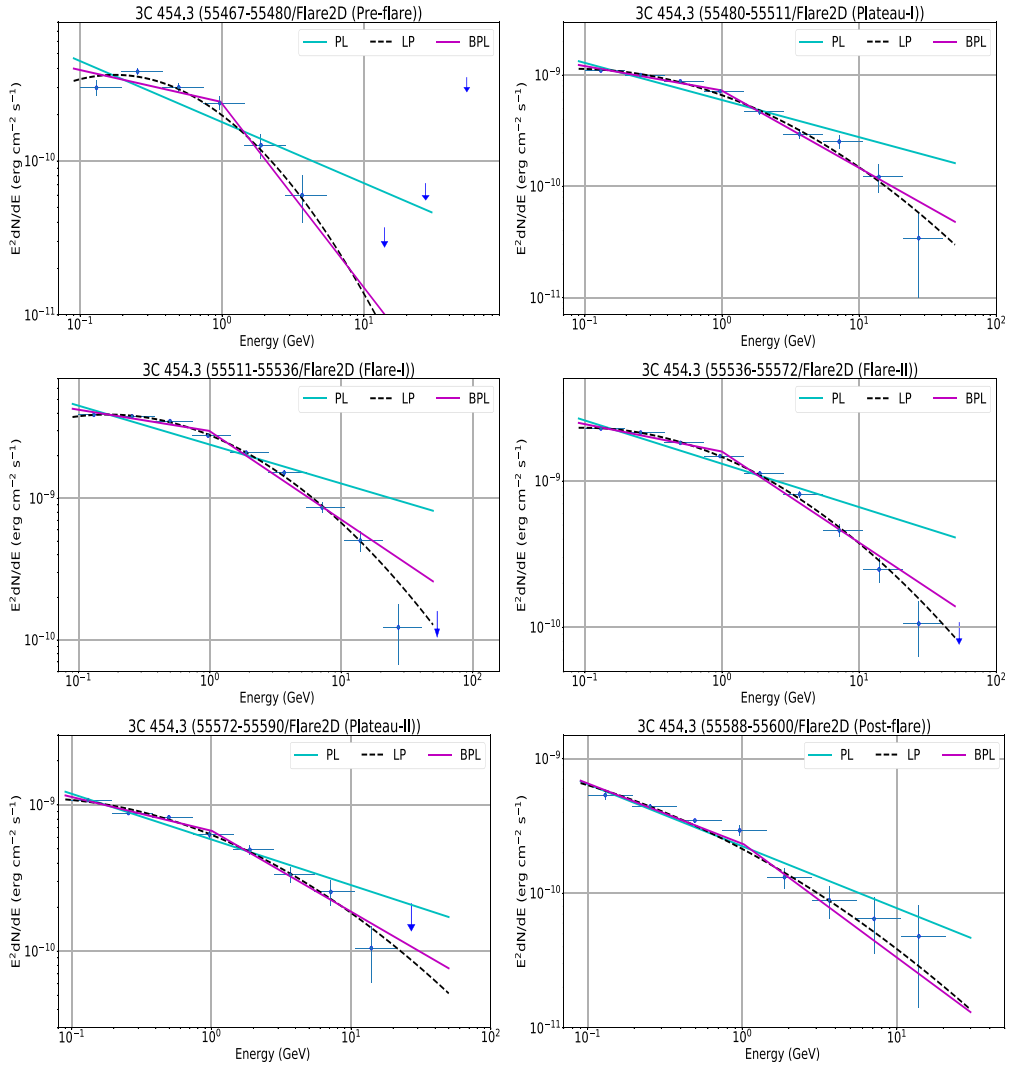

Figure 36. SED of different periods of Flare-2D as given in Figure 12. PL, LP, and BPL describe the power-law, log-parabola, and broken-power-law model, respectively, which are fitted to data points.

modeling the SEDs of Flare-2A and Flare-2D. Light curves represent the photon fluxes at different time epochs. The time variation of photon fluxes, representing complicated structures, reflects instantaneous perturbations in the emission zone. Time-dependent modeling of blazars (Saito et al. 2015; Potter 2018) has been used earlier to simulate the photon fluxes with time. Simulated profiles of flares of PKS 1510−089 were analyzed in optical, X-ray, and high-energy and very high-energy gamma-ray for a timescale of hours (Saito et al. 2015). Simultaneous multiwavelength data are not available at different frequencies to test their model predictions. The time variation of some of the parameters involved in modeling may generate time-dependent photon flux to mimic the flare peaks in the light curves over short time intervals.

Here we discuss the modeling of the γ-ray light curves using multiwavelength SED parameters. We have chosen short-duration flare peaks of three types, $T_r > T_d$, $T_r < T_d$, and $T_r \sim T_d$, since the long-duration peaks have much more complex time-dependent structures. These peaks are Peak P5 ($T_r > T_d$), P1 ($T_r < T_d$), and P3 ($T_r \sim T_d$). Since Flare-2B (Figure 7, MJD 55152−55177) has many peaks, which include all three types of peaks $T_r = T_d$, $T_r > T_d$, and $T_r < T_d$, we have chosen three different types of peaks of this flare. We have modeled the light curves by varying separately the Doppler factor (δ) and the normalization constant of the injected electron flux (l_0). While doing this, we fixed the other SED model parameters ($E_{\rm min}$, $E_{\rm max}$, B, R, etc.) to their average values as used for SED modeling of Flare-2A since multi-wavelength data of Flare-2B are not available for SED modeling.

(i) Case 1: In this case we calculate the light curve by varying the Doppler factor as a function of time, which goes as broken power law

$$\delta = \begin{cases} k t^{a_1}, & \text{for } t < t_c \\ k t_c^{(a_1 - a_2)} t^{a_2}, & \text{otherwise} \end{cases}, \quad (15)$$

where t_c is peak time, k is normalization constant, and a_1, a_2 are the indices of the broken power law.

The blob is boosted to a higher Doppler factor, which causes the rise in photon flux and then slows down during the decay phase. Due to poor photon statistics, a detailed modeling of the time variation of the Doppler factor is not possible at this stage. We have calculated the integrated γ-ray flux in the Fermi-LAT energy range ($0.1 \leqslant E \leqslant 300$ GeV) in each time step from the

Table 18
All the Parameters Represented here Are Similar to the Parameters of Table 6

Power Law						
Activity	F_0 (10^{-6} photons cm^{-2} s^{-1})	Γ			log(Likelihood)	
Pre-flare	1.10 ± 0.08	2.43 ± 0.06	⋯	⋯	42871.64	⋯
Flare	3.10 ± 0.07	2.31 ± 0.02	⋯	⋯	113517.61	⋯
Post-flare	2.00 ± 0.10	2.45 ± 0.05	⋯	⋯	41430.56	⋯
Log-parabola						
Activity	F_0 (10^{-6} photons cm^{-2} s^{-1})	α	β	⋯	log(Likelihood)	Δlog(Likelihood)
Pre-flare	1.90 ± 0.10	2.41 ± 0.07	0.04 ± 0.04	⋯	42871.02	0.62
Flare	3.00 ± 0.07	2.20 ± 0.03	0.97 ± 0.20	⋯	113502.15	−15.46
Post-flare	1.10 ± 0.08	2.36 ± 0.09	0.05 ± 0.05	⋯	41430.13	−0.43
Broken Power Law						
Activity	F_0 (10^{-6} photons cm^{-2} s^{-1})	Γ_1	Γ_2	$E_{\rm break}$ (GeV)	log(Likelihood)	Δlog(Likelihood)
Pre-flare	1.10 ± 0.10	2.35 ± 0.24	2.60 ± 0.23	0.793 ± 0.265	42871.10	−0.54
Flare	3.10 ± 0.07	2.21 ± 0.03	2.77 ± 0.14	1.271 ± 0.306	113503.80	−13.81
Post-flare	2.00 ± 0.11	2.41 ± 0.07	2.64 ± 0.25	1.309 ± 0.344	41430.21	−0.35

Note. Results are shown for Flare-5B.

Table 19
Results of Reduced-χ^2 Value for Different Spectral Models

Activity	Reduced-χ^2		
Flare-1A	Power Law	Log-parabola	Broken Power Law
Flare	12.38	3.98	1.72
Flare-2A			
Flare	49.06	4.53	12.19
Flare-2B			
Flare	41.92	1.64	2.00
Flare-2C			
Flare-I	1796.62	0.37	122.61
Flare-II	11.05	0.19	1.32
Flare-2D			
Flare-I	129.60	1.76	16.99
Flare-II	43.70	0.62	6.23
Flare-3A			
Flare-I	15.13	1.18	5.64
Flare-II	24.86	2.82	3.02
Flare-3B			
Flare	5.65	4.06	2.60
Flare-4A			
Flare	8.07	0.60	1.33
Flare-4B			
Flare	12.04	0.54	2.15
Flare-4C			
Flare	241.71	2.80	31.62
Flare-4D			
Flare	1.09	0.61	0.31
Flare-5A			
Flare	47.71	1.05	6.60
Flare-5B			
Flare	4.48	0.14	0.61

Note. Column (1): different flares' activity.

multiwavelength SED model and fitted to the light-curve data points. Our results are shown in Figures 50–52 for the three types of flare peaks. The best-fitted model parameters in Equation (15), along with the range of values of the Doppler factor (δ), have been displayed in Table 21.

(ii) Case 2: In this case we fix the Doppler factor to its average value of Flare-2A but vary the normalization constant (l_0) of the injected electron flux (Equation (8)) with a functional form similar to δ, which is defined by

$$l_0 = \begin{cases} kt^{a_3}, & \text{for } t < t_c \\ kt_c^{(a_3-a_4)}t^{a_4}, & \text{otherwise} \end{cases}, \quad (16)$$

where t_c is peak time, k is normalization constant, and a_3, a_4 are the indices of the broken power law.

The normalization constant of the injected electron flux in the emission region increases, which causes the peak in the light curve, and subsequently it decreases when the photon flux diminishes. Similar to Case 1, it is not possible to get more accurate results on time variation of the normalization constant l_0 owing to poor photon statistics. We have calculated the integrated γ-ray flux from our SED model in each time step to obtain the simulated light curve as before. Our simulated light curves of these peaks have been shown in Figures 53–55, respectively. The best-fitted values of the parameters in Equation (16), along with the ranges in the values of the normalization constant (l_0) and injected power in electrons (P_e) for each flare peak, have been given in Table 22.

Thus, we show that the light curves can be approximately generated by varying the Doppler factor (δ) or the normalization constant (l_0).

8. Discussion

3C 454.3 is one of the most violent sources in the Fermi 3FGL catalog. We have analyzed the light curve of this source

Table 20
Results of Multiwavelength SED Modeling, Which Is Shown in Figures 48 and 49

Different Cases	Parameters	Symbol	Values	Time Duration
	Flare-2A			
	Spectral index of injected electron spectrum (LP)	α	2.00	
	Magnetic field in emission region	B	3.80 G	
	Temperature of BLR region	$T'_{\rm BLR}$	2.0×10^4 K	95 days
	Photon density of BLR region	$U'_{\rm BLR}$	5.63 erg cm^{-3}	
	Temperature of disk	$T'_{\rm Disk}$	1.0×10^6 K	
	Photon density of disk	$U'_{\rm Disk}$	1.48×10^{-5} erg cm^{-3}	
	Size of the emission region	R	3.0×10^{16} cm	
	Doppler factor of emission region	δ	27.5	
	Lorentz factor of the emission region	Γ	20	
	Power in the magnetic field	P_B	1.95×10^{46} erg s^{-1}	
	Curvature index of electron spectrum	β	0.09	
Case 1	Min value of Lorentz factor of injected electrons	$\gamma_{\rm min}$	5.5×10^1	
($\tau \sim R/c$)	Max value of Lorentz factor of injected electrons	$\gamma_{\rm max}$	5.7×10^3	
	Power in the injected electrons	P_e	5.64×10^{45} erg s^{-1}	
	Curvature index of electron spectrum	β	0.08	
Case 2	Min value of Lorentz factor of injected electrons	$\gamma_{\rm min}$	4.5×10^1	
($\tau \propto E^{-0.5}$)	Max value of Lorentz factor of injected electrons	$\gamma_{\rm max}$	5.3×10^3	
	Power in the injected electrons	P_e	6.74×10^{45} erg s^{-1}	
	Flare-2D			
	Spectral index of injected electron spectrum (LP)	α	2.18	
	Magnetic field in emission region	B	2.30 G	
	Temperature of BLR region	$T'_{\rm BLR}$	2.0×10^4 K	133 days
	Photon density of BLR region	$U'_{\rm BLR}$	5.63 erg cm^{-3}	
	Temperature of disk	$T'_{\rm Disk}$	1.0×10^6 K	
	Photon density of disk	$U'_{\rm Disk}$	1.48×10^{-5} erg cm^{-3}	
	Size of the emission region	R	3.0×10^{16} cm	
	Doppler factor of emission region	δ	27.5	
	Lorentz factor of the emission region	Γ	20	
	Power in the magnetic field	P_B	7.14×10^{45} erg s^{-1}	
	Curvature index of electron spectrum	β	0.09	
Case 1	Min value of Lorentz factor of injected electrons	$\gamma_{\rm min}$	3.0×10^2	
($\tau \sim R/c$)	Max value of Lorentz factor of injected electrons	$\gamma_{\rm max}$	1.15×10^4	
	Power in the injected electrons	P_e	1.54×10^{46} erg s^{-1}	
	Curvature index of electron spectrum	β	0.14	
Case 2	Min value of Lorentz factor of injected electrons	$\gamma_{\rm min}$	2.8×10^2	
($\tau \propto E^{-0.5}$)	Max value of Lorentz factor of injected electrons	$\gamma_{\rm max}$	1.2×10^4	
	Power in the injected electrons	P_e	2.09×10^{46} erg s^{-1}	

Note. Column (1): study of different cases (see text for more details). Time duration of the flares is given in the last column.

in γ-ray for a 7-day time bin during 2008 August–2017 July, which consists of five major flares as shown in Figure 1. Each major flare comprises several substructures (or subflares), which are identified in 1-day and 6 hr binning analysis. All the substructures show different phases of activity (e.g., pre-flare, flare, plateau, post-flare). Flare regions of each substructure consist of several distinctive peaks (labeled as P1, P2, etc.) of different photon counts. Only one substructure, Flare-1A, has been identified in Flare-1. The light curve of Flare-1 is shown in Figure 2 for 1-day binning, which shows flare and post-flare phases. The peaks P1, P2, and P3 are identified in Figure 3 for the flare phase of Flare-1A. The gamma-ray SED data points are fitted with log-parabola, broken-power-law, and power-law

Table 21
Best-fitted Values of the Parameters when Doppler Factor Is Varying According to Equation (15) to Model the Light Curve of Different Types of Flare Peaks

Type of Flare Peak	Best-fitted Parameter Value				
	t_c	a_1	a_2	k	Range of δ
($T_r \sim T_d$)	1.116	0.195	−0.205	47.36	42.60–47.20
($T_r > T_d$)	1.364	0.07	−0.65	58.48	48.50–57.65
($T_r < T_d$)	1.864	0.63	−0.58	30.39	28.60-43.20

Note. Last column represents the range of values of the Doppler factor (δ) for each peak.

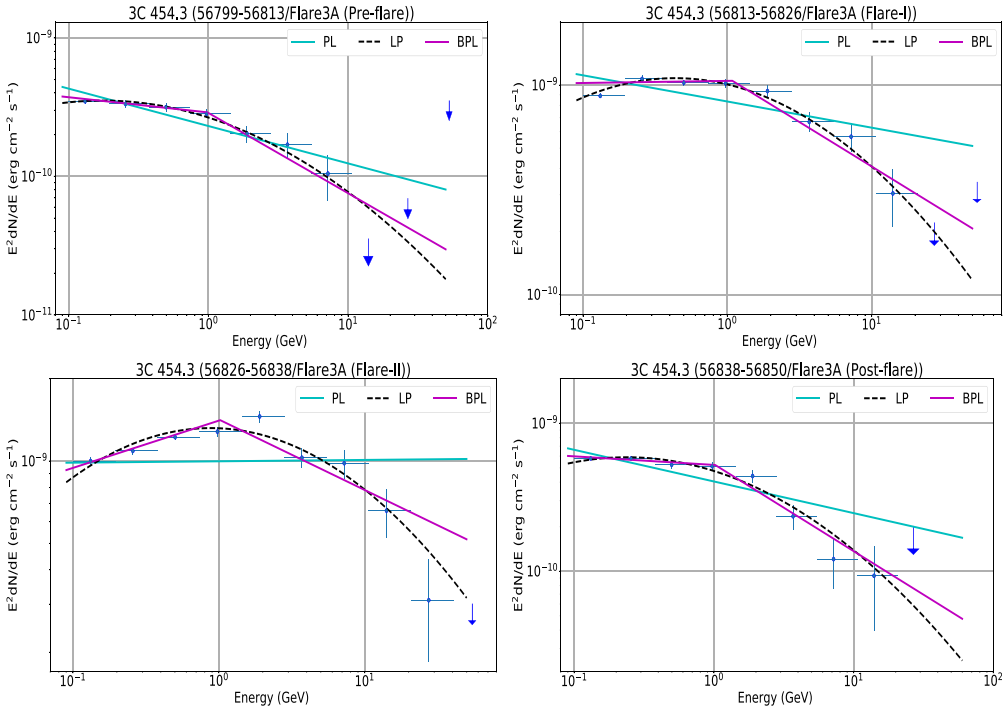

Figure 37. SED of different periods of Flare-3A as given in Figure 15. PL, LP, and BPL describe the power-law, log-parabola, and broken-power-law model, respectively, which are fitted to data points.

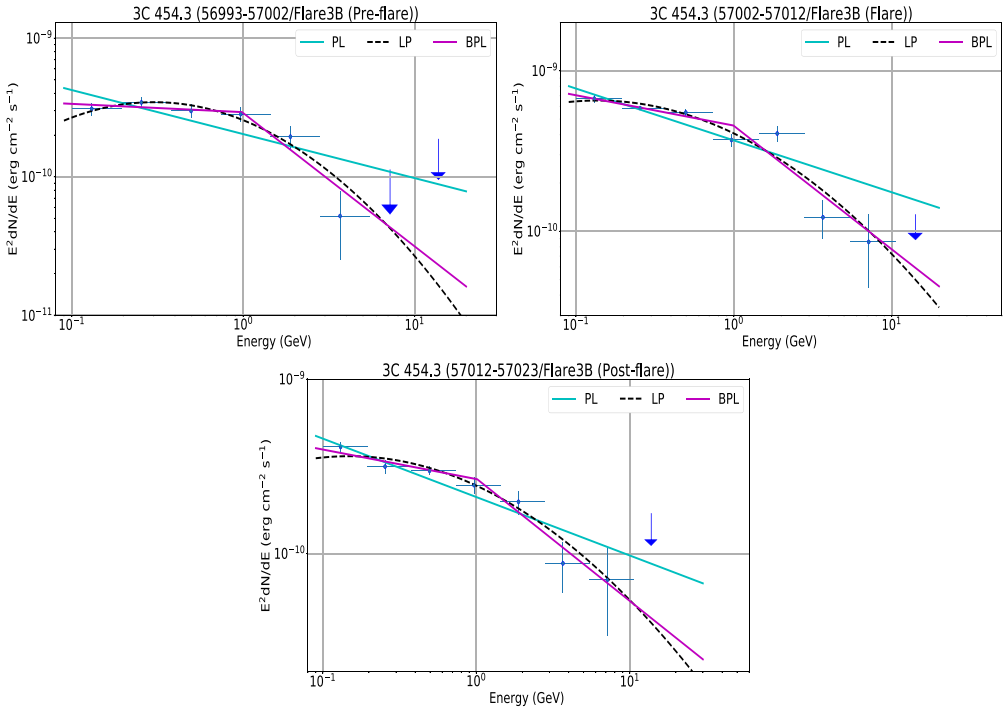

Figure 38. SED of different periods of Flare-3B as given in Figure 18. PL, LP, and BPL describe the power-law, log-parabola, and broken-power-law model, respectively, which are fitted to data points.

functions to find which function gives the best fit to the data. The same procedure has been carried out for all the flares subsequently for 6 hr binning except Flare-2A, where we have used same binning as Flare-1A. Table 19 shows that in most cases the gamma-ray SEDs of flares are well represented by the log-parabola function. The scanning of the 6 hr binning light curve is done to estimate the variability timescale in gamma-ray emission. The results are displayed in Tables 15 and 16. The shortest variability time is found to be hour scale (1.70 ± 0.38). The rise and decay timescales of flares are studied to see whether they follow any trend. Characteristic rising and decay timescales (T_r and T_d) have been computed for each peak, which are shown in Tables 1–13. We have found that the values of T_r and T_d vary between hour and day scales for

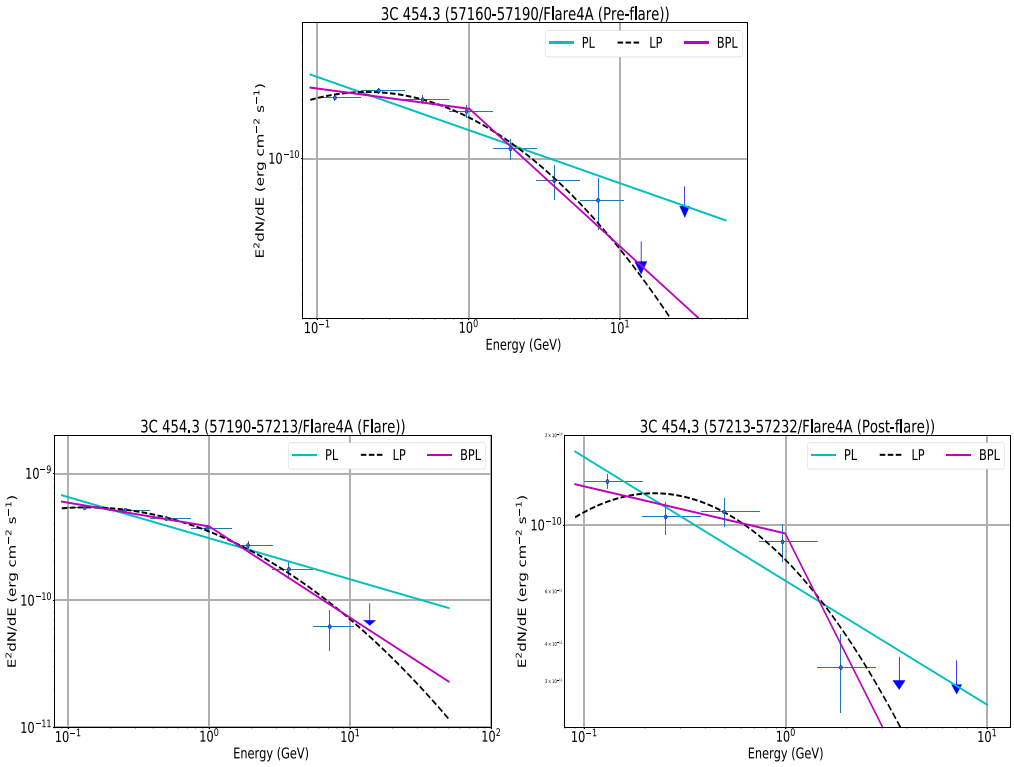

Figure 39. SED of different periods of Flare-4A as given in Figure 20. PL, LP, and BPL describe the power-law, log-parabola, and broken-power-law model, respectively, which are fitted to data points.

Table 22

Best-fitted Values of the Parameters when Normalization Constant (l_0) Is Varying According to Equation (16) to Model the Light Curve of Different Types of Flare Peaks

Type of Flare Peak	Best-fitted Parameter Value					
	t_c	a_3	a_4	k	Range of $l_0(\times 10^{50})$	Range of $P_e(\times 10^{46}$ erg s$^{-1})$
($T_r \sim T_d$)	1.116	0.586	−0.605	20.23	14.83–20.25	2.39–3.27
($T_r > T_d$)	1.364	0.22	−2.00	36.69	21.00–38.95	3.39–6.27
($T_r < T_d$)	1.861	1.43	−1.55	6.18	4.30–14.90	0.693–2.4

Note. Columns (5) and (6): range of values of the normalization constant (l_0) and injected power in electrons (P_e) for each peak, respectively.

different peaks. To compare these two timescales (T_r and T_d), we define a quantity K, which is given by (Abdo et al. 2010a)

$$K = \frac{T_d - T_r}{T_d + T_r}. \quad (17)$$

Depending on the value of K, there may be three different possibilities as discussed below:

1. Rising timescale is greater than decay timescale ($T_r > T_d$) when $K < -0.3$. This may happen when injection rate is slower than the cooling rate of electrons into the emission region. The electrons can lose energy through inverse Compton and synchrotron cooling.
2. Decay timescale is greater than rising timescale ($T_r < T_d$) when $K > 0.3$. This could be due to longer cooling timescale of electrons.
3. Nearly equal rising and decay timescale ($T_r \sim T_d$) or symmetric temporal evolution when $-0.3 \leqslant K \leqslant 0.3$. This property can be explained by perturbation in the jet or a dense plasma blob passing through a standing shock front in the jet region (Blandford & Königl 1979).

In our study we have found that out of a total of 69 prominent peaks, 16 peaks have $T_r > T_d$, 20 peaks have $T_r < T_d$, and 33 peaks have $T_r \sim T_d$. Earlier, a similar study was done for PKS 1510−089 with 8 yr of Fermi-LAT data (Prince et al. 2017). The rise and decay times were presented in Tables 1–5 and plotted in Figure 27 of Prince et al. (2017). For most of the peaks the decay time was found to be shorter than the rise time. CTA 102, another flaring FSRQ, was studied for a much shorter period, 2016 September–2017 March (Prince et al. 2018). During its flaring state, 14 peaks were identified. Out of these, 5 peaks had nearly equal decay and rise time, 5 peaks had slower rise time than decay time, and 4 peaks had slower decay time than rise time. These results suggest that the decay and rise times of peaks do not have any specific trend for flaring FSRQs.

The SED modeling has been done for the two flares Flare-2A and Flare-2D, for which multiwavelength data are available. The modeling has been done with the time-dependent code GAMERA, which solves the transport equation for electrons, including their energy losses by synchrotron and inverse Compton emission (SSC and EC), and escape. We have

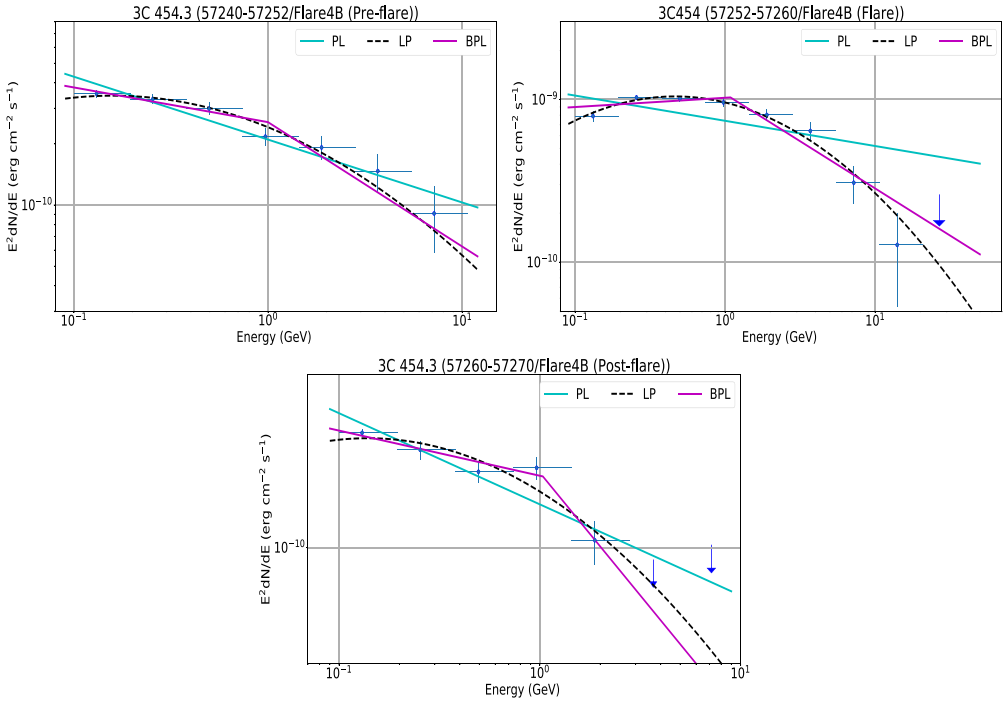

Figure 40. SED of different periods of Flare-4B as given in Figure 22. PL, LP, and BPL describe the power-law, log-parabola, and broken-power-law model, respectively, which are fitted to data points.

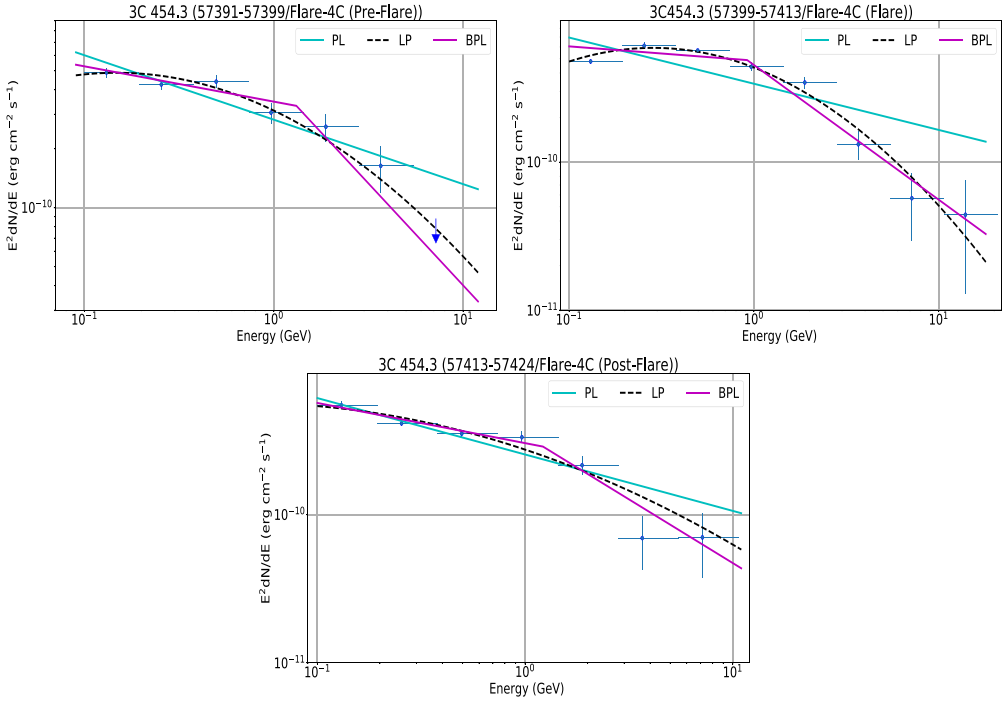

Figure 41. SED of different periods of Flare-4C as given in Figure 24. PL, LP, and BPL describe the power-law, log-parabola, and broken-power-law model, respectively, which are fitted to data points.

considered two cases for the escape timescale: (i) constant escape time $R/c = 10^6$ s and (ii) energy-dependent escape time, which goes as $E^{-0.5}$. We note that the cooling timescale of the electrons in case (i) is much shorter than R/c in our case. In case (ii) the escape time is comparable to the cooling time for low-energy electrons, but for high-energy electrons the cooling time decreases faster than the escape time as it goes as E^{-1}. Table 20 shows the results of our SED modeling. The results for the two cases are comparable for both Flare-2A and Flare-2D. Magnetic field is slightly higher for Flare-2A. The jet power in relativistic electrons and positrons is higher for Flare-2D compared to Flare-2A. Figures 48 and 49 show the results

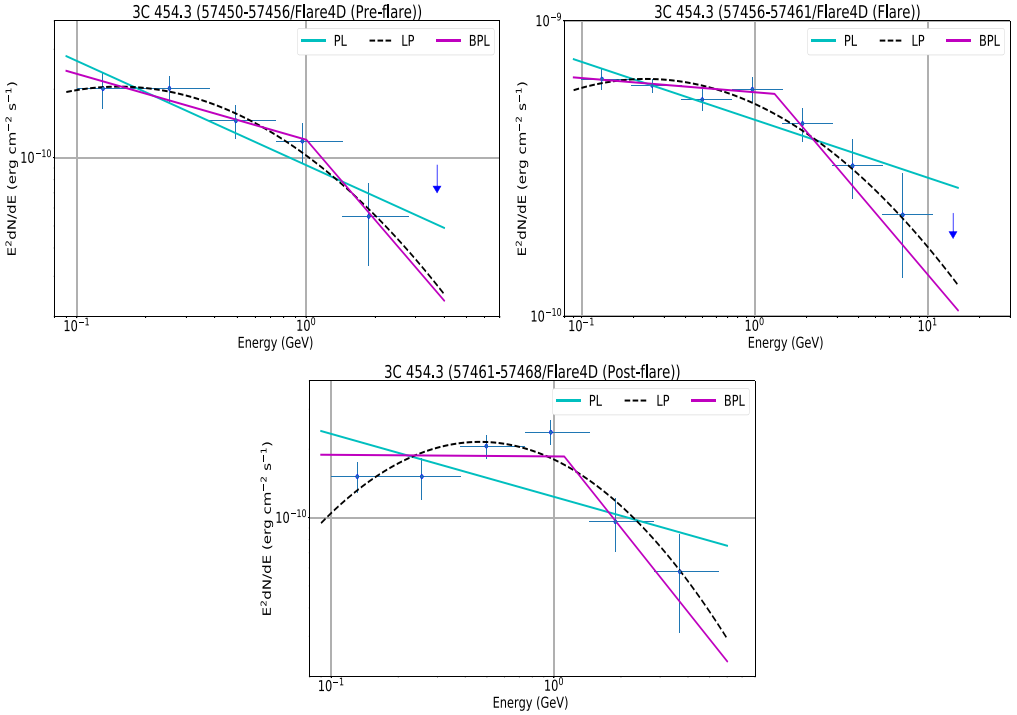

Figure 42. SED of different periods of Flare-4D as given in Figure 26. PL, LP, and BPL describe the power-law, log-parabola, and broken-power-law model, respectively, which are fitted to data points.

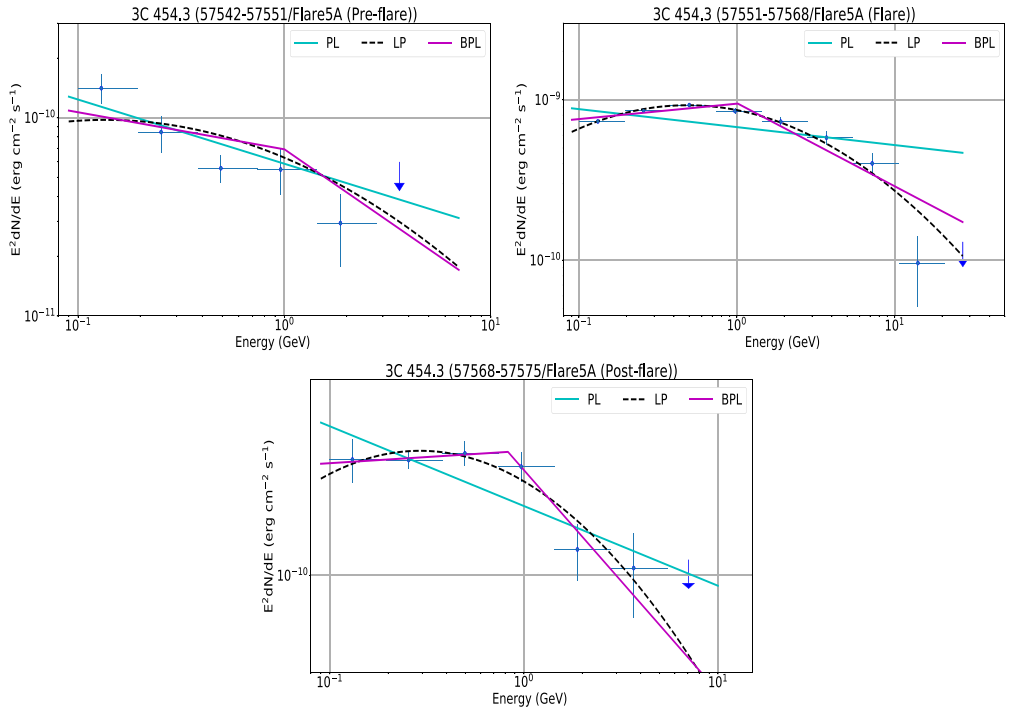

Figure 43. SED of different periods of Flare-5A as given in Figure 28. PL, LP, and BPL describe the power-law, log-parabola, and broken-power-law model, respectively, which are fitted to data points.

of our SED modeling. If we divide the duration of a flare into four equal time intervals, the SED calculated for each time interval overlaps with each other. The electron spectrum becomes steady in a short time compared to the durations of Flare-2A and Flare-2D, and as a result, their radiated photon spectrum also becomes steady. Due to this reason, it is not possible to see the time evolution in Figures 48 and 49.

3C 454.3, being highly variable in gamma-rays, is often monitored. The data from 2008 July 7 to October 6 were analyzed to study the flaring activity during this period (Abdo et al. 2009).

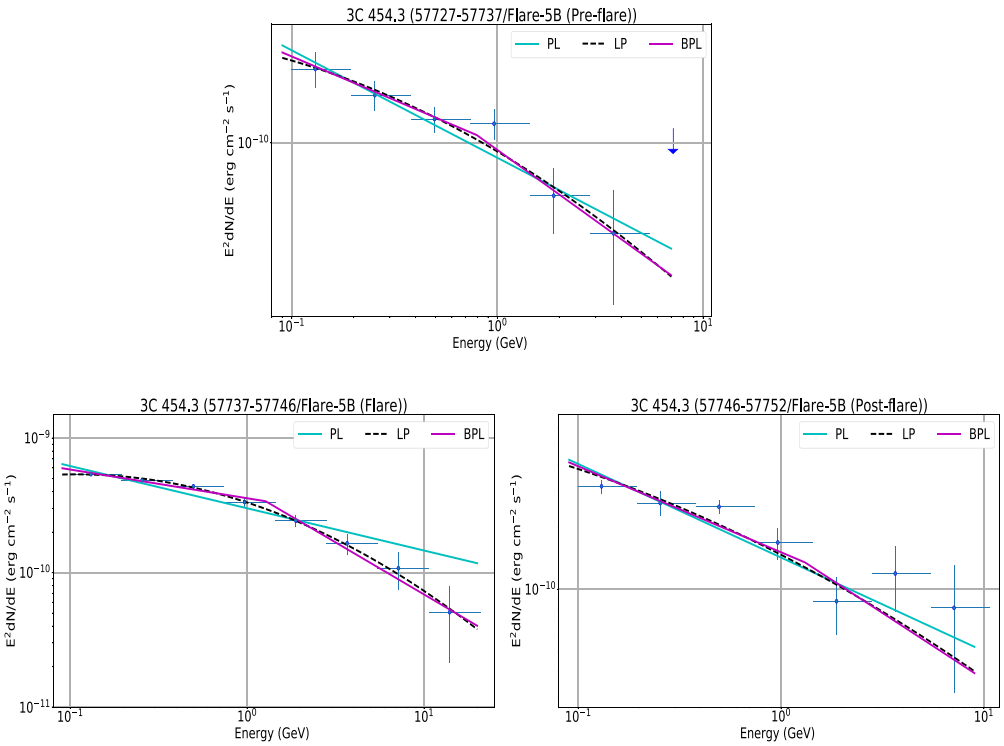

Figure 44. SED of different periods of Flare-5B as given in Figure 30. PL, LP, and BPL describe the power-law, log-parabola, and broken-power-law model, respectively, which are fitted to data points.

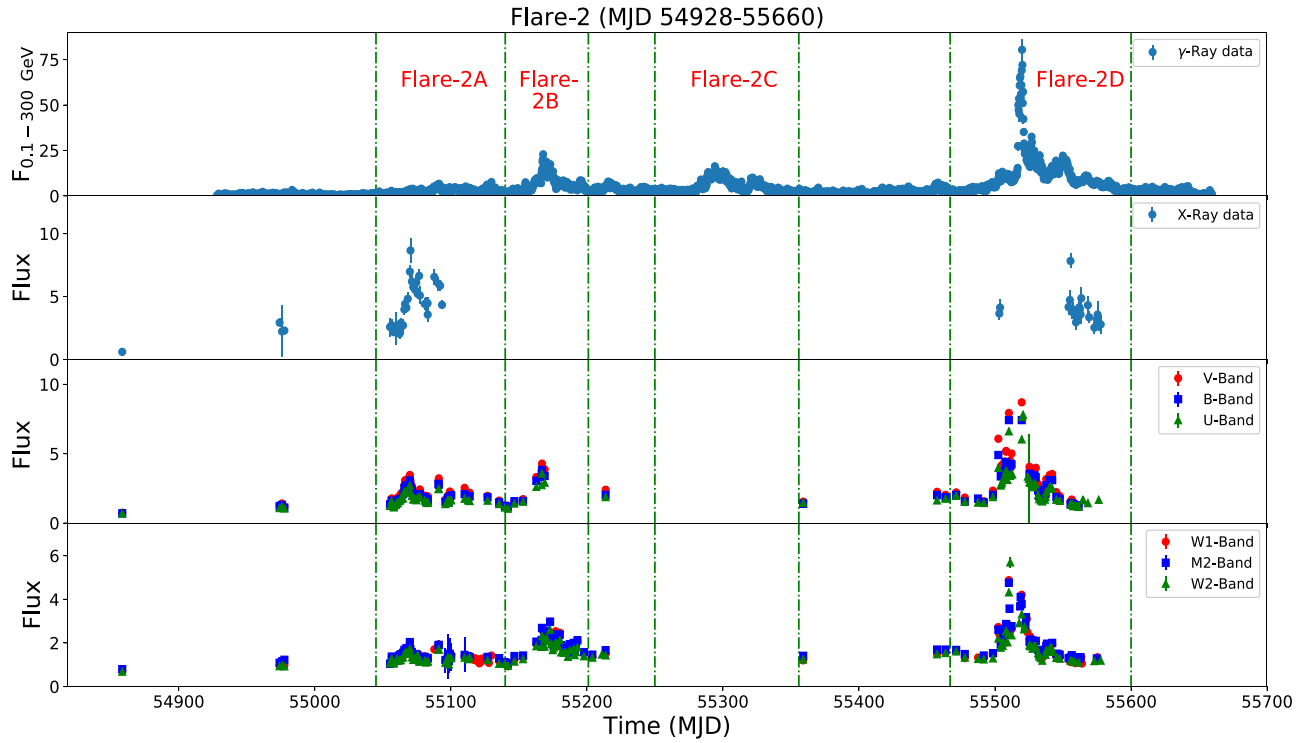

Figure 45. Multiwavelength light curve of Flare-2. Four distinctive major flares have been identified. The γ-ray flux ($F_{0.1-300GeV}$) is in units of 10^{-6} photons cm^{-2} s^{-1}. X-ray, optical (V, B, and U band), and ultraviolet ($W1$, $M2$, and $W2$ band) fluxes are in units of 10^{-11} erg cm^{-2} s^{-1}.

They observed nearly symmetric flares with rise and decay timescales of 3.5 days. They obtained a lower bound of 8 on the value of Doppler factor. Their gamma-ray SED is best represented by a broken power law with a break near 2 GeV. They suggested that this break may be due to an intrinsic break in the electron spectrum. Finke & Dermer (2010) suggested a combination of the Compton-scattered disk and BLR radiation to explain the spectral break and also fit the quasi-simultaneous radio, optical, X-ray, and gamma-ray data of the 2008 flare. Hunger & Reimer (2016) used a particle distribution with a break to model the flare emission

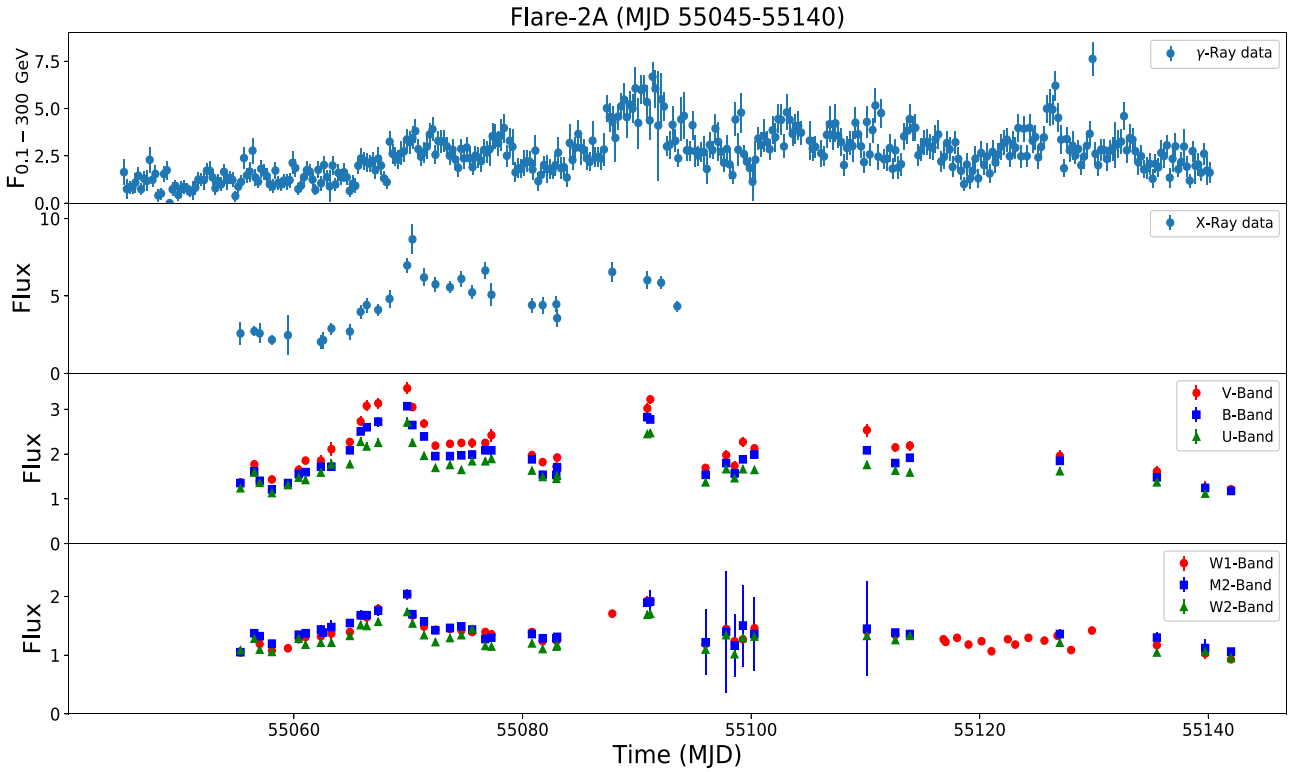

Figure 46. Multiwavelength light curve of Flare-2A. The γ-ray flux ($F_{0.1-300\,\mathrm{GeV}}$) is in units of 10^{-6} photons cm^{-2} s^{-1}. X-ray, optical (V, B, and U band), and ultraviolet ($W1$, $M2$, and $W2$ band) fluxes are in units of 10^{-11} erg cm^{-2} s^{-1}.

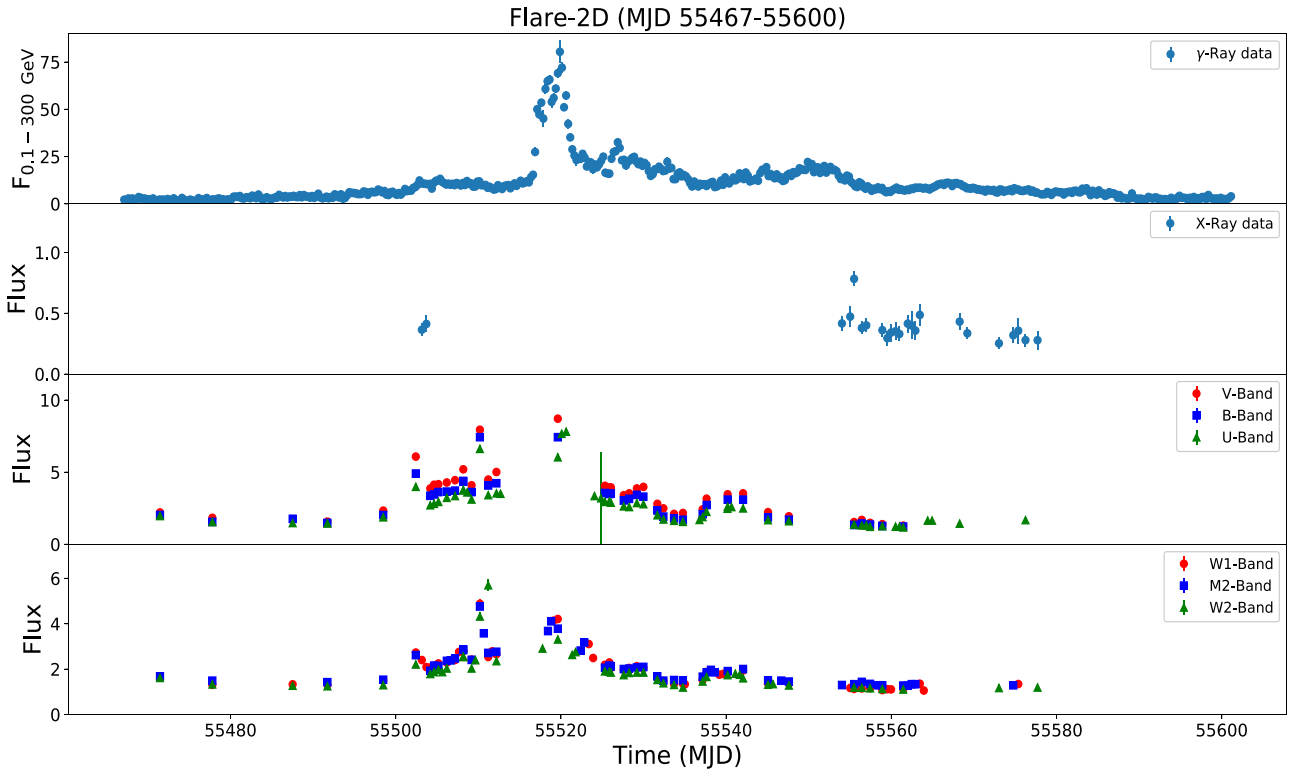

Figure 47. Multiwavelength light curve of Flare-2D. The γ-ray flux ($F_{0.1-300\,\mathrm{GeV}}$) is in units of 10^{-6} photons cm^{-2} s^{-1}. X-ray, optical (V, B, and U band), and ultraviolet ($W1$, $M2$, and $W2$ band) fluxes are in units of 10^{-11} erg cm^{-2} s^{-1}.

with Compton-scattered BLR radiation alone and also in combination with Compton-scattered disk emission. Kohler & Nalewajko (2015) studied many short bright flares of blazars, including 3C 454.3. They concluded that the average Fermi-LAT spectrum is a superposition of many short-lived components where each one has a different spectral curvature. In our work in

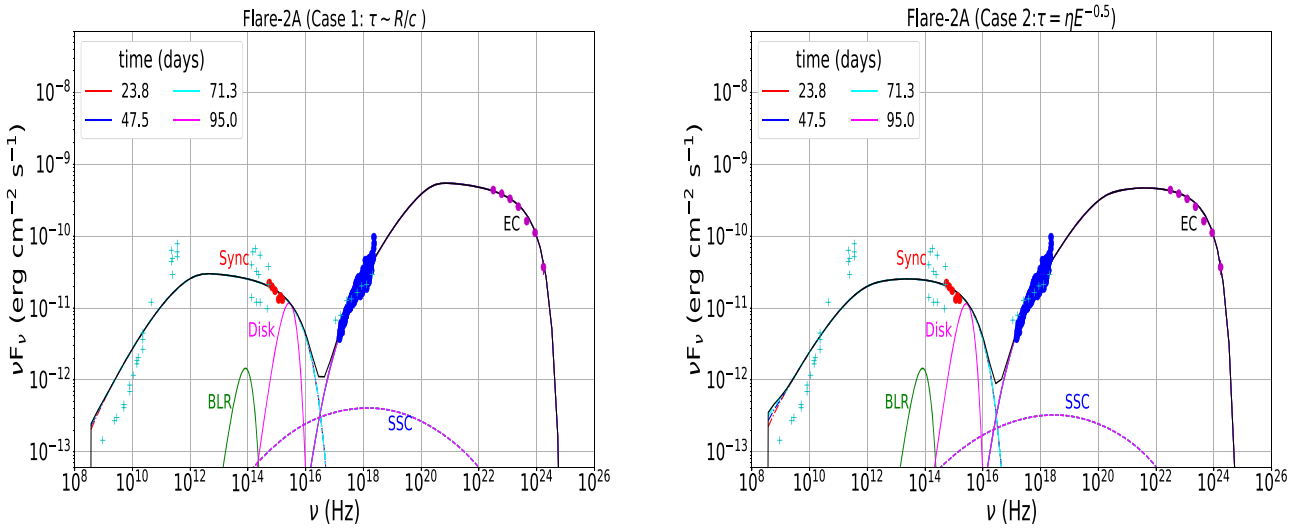

Figure 48. Multiwavelength SED of Flare-2A for two different cases of escape timescale. Our analyzed data are shown in red, blue, and purple. Nonsimultaneous data (see text for more details) are shown by a cyan plus sign, which is taken from Abdo et al. (2010c).

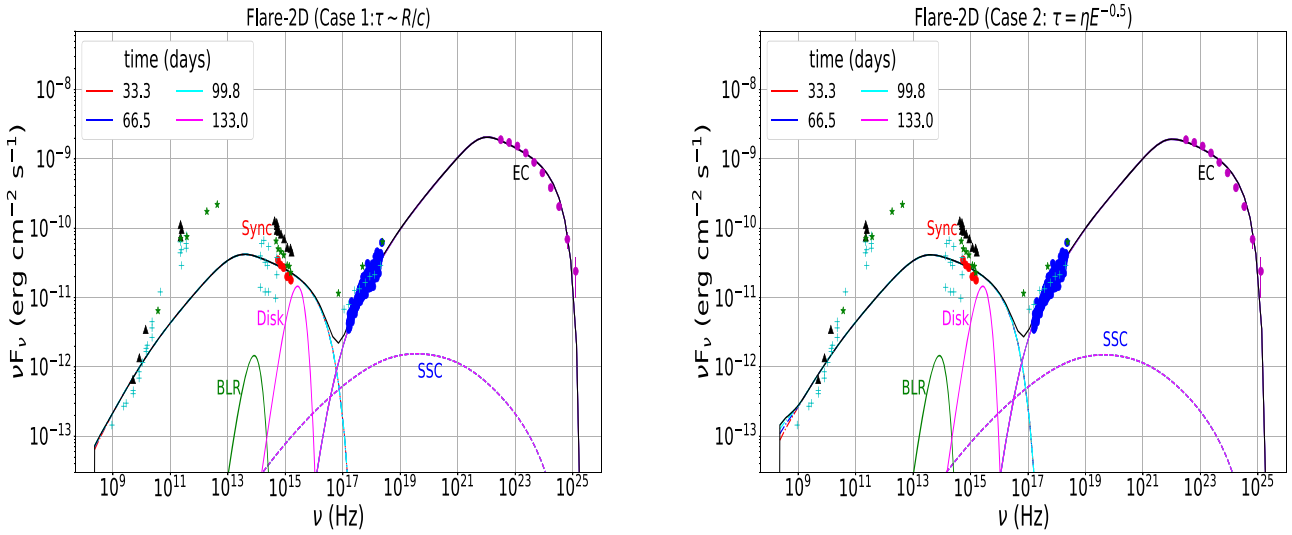

Figure 49. Multiwavelength SED of Flare-2D for two different cases of escape timescale. Our analyzed data are shown in red, blue, and purple. Nonsimultaneous data (see text for more details) are shown by a cyan plus sign, which is taken from Abdo et al. (2010c). Quasi-simultaneous data are also shown by a black triangle (Vercellone & Striani 2011) and green star (Jorstad et al. 2013).

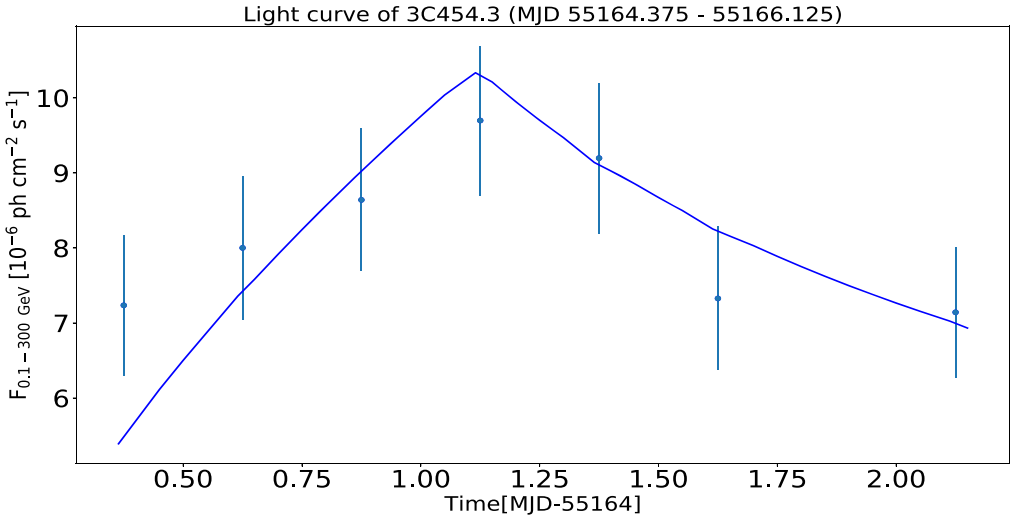

Figure 50. Modeled light curve (by varying Doppler factor) between the data of MJD 55164.375−55166.125, which corresponds to P3 peak of the first part of Flare-2B.

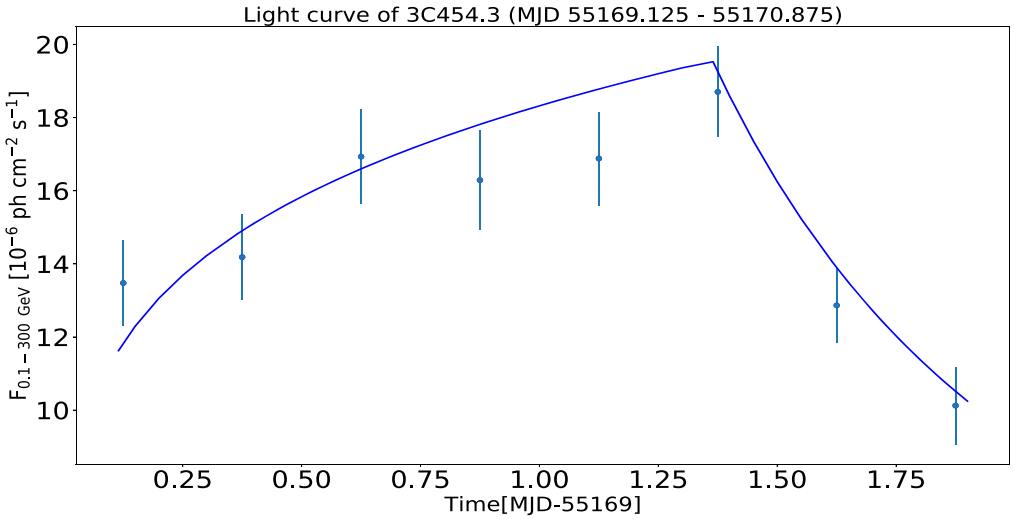

Figure 51. Modeled light curve (by varying Doppler factor) between the data of MJD 55169.125−55170.875, which corresponds to P5 peak of the first part of Flare-2B.

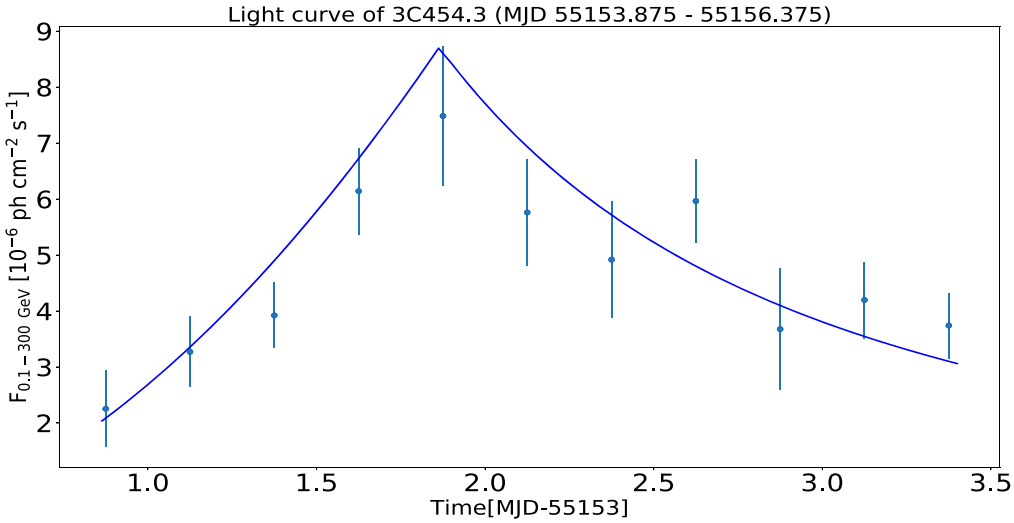

Figure 52. Modeled light curve (by varying Doppler factor) between the data of MJD 55153.875−55156.375, which corresponds to P1 peak of the first part of Flare-2B.

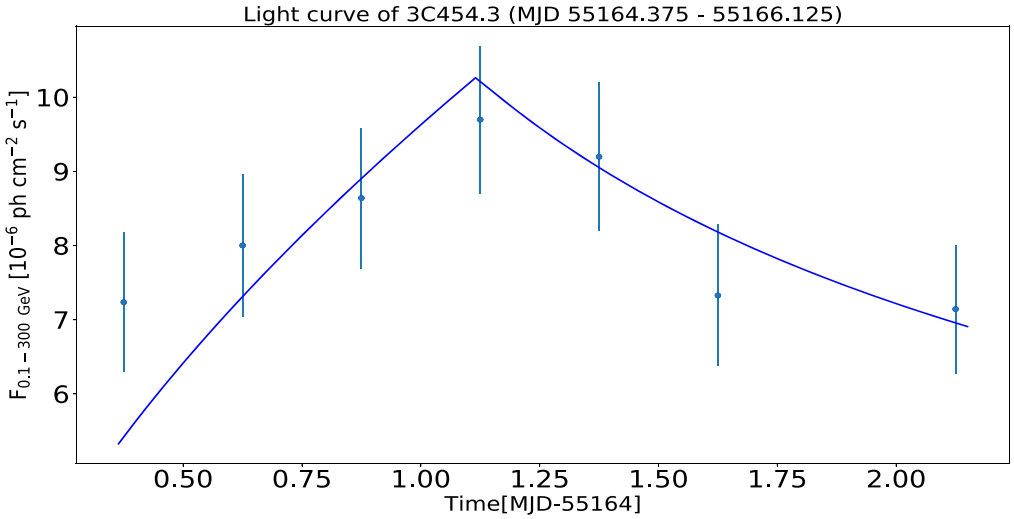

Figure 53. Modeled light curve (by varying normalization constant of the flux of injected electrons) between the data of MJD 55164.375−55166.125, which corresponds to P3 peak of the first part of Flare-2B.

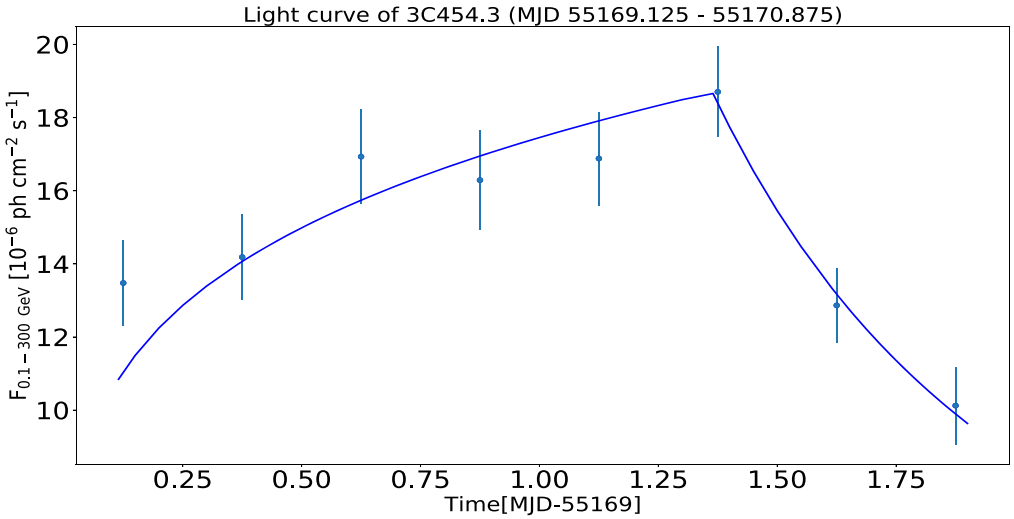

Figure 54. Modeled light curve (by varying normalization constant of the flux of injected electrons) between the data of MJD 55169.125−55170.875, which corresponds to P5 peak of the first part of Flare-2B.

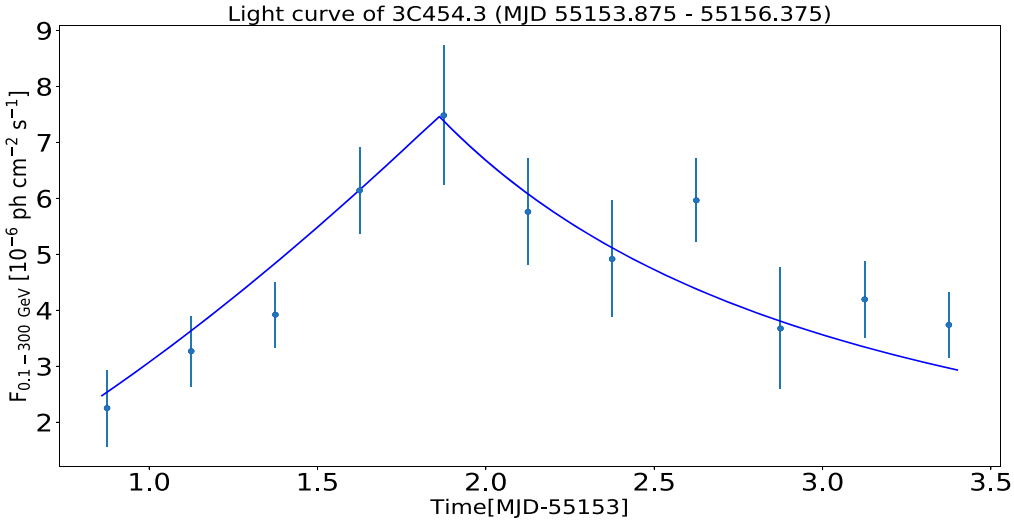

Figure 55. Modeled light curve (by varying normalization constant of the flux of injected electrons) between the data of MJD 55153.875−55156.375, which corresponds to P1 peak of the first part of Flare-2B.

many cases (see Table 19) the log-parabola function well represents the gamma-ray SEDs of flares.

While modeling the two flares Flare-2A and Flare-2D, we have assumed the emission region to be in the BLR region, which is commonly assumed in single-zone SED modeling. However, for many of the flares a more complicated and realistic scenario may be required to explain the temporal and spectral features.

Due to its variable nature, this source should be monitored for high-energy neutrino emission during its flaring states. High-energy neutrinos can escape from the jets even if they are produced in the inner regions of jets. In this case high-energy neutrinos may be detected without counterparts in high-energy gamma-rays. More simultaneous multiwavelength data and constraint on neutrino flux from IceCube detector would be useful to model the flares, constrain their hadronic jet power, and locate the emission regions of the flares.

Below we clarify some important points on our analysis.

The "sum of exponentials" (Equation (2)) is the function that the "blazar community" uses to model the peaks observed in a light curve. We have performed the fitting in python with the "curvefit" package. The number of exponentials is chosen based on the number of peaks observed in a particular light curve. The first exponential function is used to fit the rising part of the peak, and this gives the rising time. Similarly, the second exponential is used to fit the decaying part of the peak, which gives the decay time. The rise and decay times of the peak play an important role for calculating the variability time, which is used to do the SED modeling. In Equation (2), we have four parameters, but among them, two parameters, peak flux (F_0) and corresponding time t_0, are fixed from observation, and we have varied T_r and T_d to get the best-fit value. However, the fitting of light curves with the "sum of exponentials" does not always give very good results. There could be many reasons if the fit is not good. It may be due to low statistics and large error bars on the data points. There is also the possibility that the flux

is changing so fast that it is impossible to catch that flux value with any smooth function. The high value of reduced chi-square could also be because of rapid variations in flux (small peaks), which have not been included during the fitting.

A statistical "mixture model" decision process can be used to choose the number of components from the fitted light curve for more sophisticated analysis. But in our case the peaks can be clearly identified from eye inspection. Moreover, we mostly use the brighter peak (where the flux is a few times higher than its initial value in a short duration of time) to estimate the variability time, so it does not matter if we leave out some small peaks in our fitting, which will of course increase the chi-square value.

One can also use the nonparametric density estimation approach, smoothing the time series with a (Gaussian) kernel or locally fitting with polynomials (e.g., splines).

In our analysis the binning of light curve is not arbitrary, as it is based on how good the data are (TS value of each data points). If the source is very bright during a flare and the flux is very high, in this case there is a chance of having good statistics, and hence we can bin the light curve up to a minute timescale. This has been done for many flares of various sources previously (see Shukla et al. 2018). In our case we have focused on 6 hr binning because for this binning the data have good statistics (TS $\sim$ 25; $\sim 5\sigma$ significance) and also each and every peak can be clearly identified.

9. Conclusion

We have identified five flares in the 9 yr gamma-ray light curve of 3C 454.3. After scanning the light curve, the shortest variability timescale is found to be of hour scale, which is similar to other flaring FSRQs, e.g., PKS 1510−089. The gamma-ray SEDs of the flares are in most cases best fitted with the log-parabola function. A similar result was also found earlier for PKS 1510−089. The rise and decay times of flares do not follow any particular trend; in some cases they are equal, but in some other cases they are not. Flare-2D (MJD 55467 −55600) is found to be the most violent substructure in the 9 yr light-curve history of this source, with six different phases of activity: pre-flare, Plateau-I, Flare-I, Flare-II, Plateau-II, and post-flare. The most basic substructures have only three phases of activity: pre-flare, flare, and post-flare. We have done time-dependent leptonic modeling of Flare-2A and Flare-2D with multiwavelength data. The magnetic fields required to model these flares are 3.8 and 2.3 G, respectively, which are comparable to the magnetic fields found from SED modeling of other blazars., e.g., PKS 1510−089 and CTA 102. The jet powers required to model these flares are below the Eddington luminosity of 3C 454.3. In the future simultaneous multi-wavelength observations and constraint on neutrino flux from the IceCube detector would be useful to understand the composition of the jets and the location of flare.

We thank the referee for helpful comments to improve this paper. This work has made use of publicly available Fermi-LAT data obtained from FSSC's website data server and provided by NASA Goddard Space Flight Center. This work has also made use of data and software/tools obtained from NASA High Energy Astrophysics Science Archive Research Center (HEASARC) developed by Smithsonian Astrophysical Observatory (SAO) and the XRT Data Analysis Software (XRTDAS) developed by ASI Science Data Center, Italy. N.G. thanks C. S. Stalin and S. Sahaynathan for helpful discussions. A.K.D. thanks T. Ghosh for proofreading.

Software: Fermitools (https://fermi.gsfc.nasa.gov/ssc/data/analysis/) GAMERA (https://github.com/libgamera/GAMERA) HEASARC (https://heasarc.gsfc.nasa.gov/docs/software/heasoft/) XSPEC (https://heasarc.gsfc.nasa.gov/xanadu/xspec/) XSELECT (https://heasarc.gsfc.nasa.gov/ftools/xselect/).

ORCID iDs

Raj Prince https://orcid.org/0000-0002-1173-7310
Nayantara Gupta https://orcid.org/0000-0002-1188-7503

References

Abdo, A. A., Ackermann, M., Agudo, I., et al. 2010c, ApJ, 716, 30
Abdo, A. A., Ackermann, M., Ajello, M., et al. 2009, ApJ, 699, 817
Abdo, A. A., Ackermann, M., Ajello, M., et al. 2010a, ApJ, 722, 520
Abdo, A. A., Ackermann, M., Ajello, M., et al. 2010b, ApJ, 710, 1271
Acero, F., Ackermann, M., Ajello, M., et al. 2015, ApJS, 218, 23
Atwood, W. B., Abdo, A. A., Ackermann, M., et al. 2009, ApJ, 697, 1071
Blandford, R. D., & Königl, A. 1979, ApJ, 232, 34
Blumenthal, R., & Gould, G. 1970, RvMP, 42, 237
Bonninng, E. W., Bailyn, C., Urry, C. M., et al. 2009, ApJL, 697, L81
Bonnoli, G., Ghisellini, G., Foschini, L., Tavecchio, F., & Ghirlanda, G. 2011, MNRAS, 410, 368
Breeveld, A. A., Landsman, W., Holland, S. T., et al. 2011, arXiv:1102.4717
Britto, R. J., Bottacini, E., Lott, B., Razzaque, S., & Buson, S. 2016, ApJ, 830, 162
Burrows, D. N., Hill, J. E., Nousek, J. A., et al. 2005, SSRv, 120, 165
Cerruti, M., Dermer, C. D., Lott, B., Boisson, C., & Zech, A. 2013, ApJL, 771, L4
Dermer, C. D., & Menon, G. 2009, High Energy Radiation from Black Holes (Princeton, NJ: Princeton Univ. Press)
Diltz, C., & Böttcher, M. 2016, ApJ, 826, 54
Donnarumma, I., Pucella, G., Vittorini, V., et al. 2009, ApJ, 707, 1115
Finke, J. D., & Dermer, C. D. 2010, ApJL, 714, L303
Gaur, H., Gupta, A. C., & Wiita, P. J. 2011, AJ, 143, 23
Ghisellini, G., & Tavecchio, F. 2009, MNRAS, 397, 985
Giommi, P., Blustin, A. J., Capalbi, M., et al. 2006, A&A, 456, 911
Gorshkov, A. G., Ipatov, A. V., Ipatova, I. A., et al. 2018, ARep, 62, 183
Gu, M., Cao, X., & Jiang, D. R. 2001, MNRAS, 327, 1111
Gupta, A. C., Mangalam, A., Wiita, P. J., et al. 2017, MNRAS, 472, 788
Hahn, J. 2015, Proc. ICRC, 34, 917
Hartman, R. C., Bertsch, D. L., Dingus, B. L., et al. 1993, ApJL, 407, L41
Hartman, R. C., Bertsch, D. L., Fichtel, C. E., et al. 1992, IAUC, 5477, 2
Hunger, L., & Reimer, A. 2016, A&A, 589, A96
Jorstad, S. G., Marscher, A. P., Smith, P. S., et al. 2013, ApJ, 773, 147
Khangulyan, D. V., Barkov, M. V., Bosch-Ramon, V., Aharonian, F. A., & Dorodnitsyn, A. V. 2013, ApJ, 774, 113
Kohler, S., & Nalewajko, K. 2015, MNRAS, 449, 2901
Kushwaha, P., Gupta, A. C., Misra, R., & Singh, K. P. 2017, MNRAS, 464, 2046
Larionov, V. M., Villata, M., Raiteri, C. M., et al. 2016, MNRAS, 461, 3047
Longair, M. S. 1974, in Proc. IAU Symp. 63, Copernicus Symp. II, ed. M. S. Longair (Dordrecht: Reidel)
Massaro, E., Perri, M., Giommi, P., & Nesci, R. 2004, A&A, 413, 489
Nalewajko, K., Gupta, A. C., Liao, M., et al. 2019, A&A, 631, A4
Paliya, V. S. 2015, ApJL, 808, L48
Potter, W. J. 2018, MNRAS, 473, 4107
Prince, R., Majumdar, P., & Gupta, N. 2017, ApJ, 844, 62
Prince, R., Raman, G., Hahn, J., Gupta, N., & Majumdar, P. 2018, ApJ, 866, 16
Protheroe, R. J. 2002, PASA, 19, 486
Raiteri, C. M., Villata, M., Aller, M. F., et al. 2011, A&A, 534, A87
Raiteri, C. M., Villata, M., Chen, W. P., et al. 2008, A&A, 485, L17
Rajput, B., Stalin, C. S., Sahayanathan, S., Rakshit, S., & Mandal, A. K. 2019, MNRAS, 486, 1781
Roming, P. W. A., Kennedy, T. E., Mason, K. O., et al. 2005, SSRv, 120, 95
Saito, S., Stawarz, L., Tanaka, Y. T., et al. 2015, ApJ, 809, 171
Sarkar, A., Chitnis, V. R., Gupta, A. C., et al. 2019, ApJ, 887, 185
Sasada, M., Uemura, M., Fukazawa, Y., et al. 2014, ApJ, 784, 141
Schlafly, E. F., & Finkbeiner, D. P. 2011, ApJ, 737, 103

Shah, Z., Sahayanathan, S., Mankuzhiyil, N., et al. 2017, MNRAS, 470, 3283
Shukla, A., Mannheim, K., Patel, S. R., et al. 2018, ApJL, 854, L26
Sinha, A., Sahayanathan, S., Acharya, B. S., et al. 2017, ApJ, 836, 83
Vercellone, S., Chen, A. W., Vittorin, V., et al. 2009, ApJ, 690, 1018
Vercellone, S., Striani, E., Vittorini, V., et al. 2011, ApJL, 736, L38
Villata, M., Raiteri, C. M., Balonek, T. J., et al. 2006, A&A, 453, 817
Weaver, Z. R., Balonek, T. J., Jorstad,, S. G., et al. 2019, ApJ, 875, 15
Wehrle, A. E., Marscher, A. P., Jorstad, S. G., et al. 2012, ApJ, 758, 72
Zamaninasab, M., Savolainen, T., Clausen-Brown, E., et al. 2013, MNRAS, 436, 3341